

THE DIFFRACTIVE DISSOCIATION PROCESS

$\pi^- p \rightarrow \pi^- (\pi^- \pi^+ p)$  AT 14 GeV/c

Thesis by

Leo C. Rosenfeld

In Partial Fulfillment of the Requirements

for the Degree of

Doctor of Philosophy

California Institute of Technology

Pasadena, California

1977

(Submitted May 25, 1977)

## ACKNOWLEDGEMENTS

The experiment which I describe in this thesis depended on the efforts of many people at three institutions. The support personnel of the Caltech High Energy Physics Group built substantial portions of the apparatus. At the Stanford Linear Accelerator Center the major contributors were the members of the Experimental Facilities Department, under the leadership of E. Seppi, especially J. Murray; the members of the Accelerator Operations staff; and the members of the Bubble Chamber Operations Group, under the leadership of R. Watt, especially G. Bowden. The scanning and measurement of the bubble chamber film at Lawrence Berkeley Laboratory was in the hands both of the Data Handling Group under the leadership of H. White and the scanning and measuring staff of the Ely Physics Group.

The physicists who played major roles in the work reported here were R. Ely, D. Grether, and P. Oddone of LBL and W. Ford, V. Davidson, F. Nagy, and C. Peck of Caltech. Professor Ely was my host during a long residence in Berkeley, and he generously made available all the resources necessary to carry out the analysis. Professor Peck, the guiding hand and chief stimulus to the entire enterprise, was my thesis adviser. His labor, his leadership, and his friendly counsel were integral to the execution of this project.

I heartily thank all who contributed to this experiment.

## ABSTRACT

We describe an experiment in which a 14 GeV/c  $\pi^-$  beam was incident on a hydrogen bubble chamber. Fast forward scattered pions traversed a wire spark chamber spectrometer downstream of the bubble chamber. Events identified as inelastic by the spectrometer induced a trigger of the bubble chamber camera. The film produced contained a heavy enrichment of events of proton diffractive dissociation.

We have studied a sample from this exposure of 4400 events of the reaction  $\pi^- p \rightarrow \pi^- N^* \rightarrow \pi^- \pi^- \pi^+ p$ . In the two body mass spectra the only noteworthy feature is the  $\Delta^{++}(1230)$ . In the  $N^*$  mass spectrum we observe enhancements at 1.49 GeV, 1.72 GeV, and 2.0 GeV. For the prominent 1.72 GeV feature we give estimates of the width and cross section as well as evidence favoring a substantial branching fraction to  $\pi\Delta(1230)$ . We looked for production of  $N^*(1470)$  followed by decay to  $\pi\Delta(1230)$  with negative result. An examination of the  $\Delta^{++}(1230)$  decay distribution suggests that the Deck mechanism is the major contributor to the  $\pi\Delta$  subchannel.

We tested the s-channel and t-channel helicity conservation rules. We observed violent conflict with sCHC and mild conflict with tCHC. We also tested for simultaneous validity of tCHC and the Gribov-Morrison rule and found no significant contradiction with this dual hypothesis.

## CONTENTS

	<u>Page</u>
ACKNOWLEDGEMENTS .....	ii
ABSTRACT .....	iii
CHAPTER	
I. INTRODUCTION	
1. The Diffraction Picture of Good and Walker .....	1
2. Properties of Diffractive Dissociation .....	6
3. The t-channel Viewpoint .....	10
4. The Deck Mechanism .....	13
5. Some Published Data at Very High Energy .....	16
6. Intent of the Present Experiment .....	21
II. EXPERIMENTAL APPARATUS	
1. Overview .....	24
2. The Secondary Beam Line .....	25
3. The Bubble Chamber .....	27
4. The Spectrometer .....	29
5. Triggering and the Role of the Online Computer ..	34
III. PROCESSING	
1. Overview .....	43
2. Processing of the Spark Chamber Data .....	43
3. Scanning and Filtering .....	46
4. Measuring .....	47
5. Geometrical Reconstruction .....	48
6. Hybridization .....	49
7. Kinematic Fitting .....	58
8. Validation .....	61
IV. ANALYSES	
1. Preamble .....	69
2. Estimation and Display of Densities .....	70
3. Event Selection .....	71
4. Normalization .....	80
5. Acceptance and Weighting .....	82
6. Survey of the N* Mass Spectra .....	85
7. Production of $\Delta^{++}(1230)$ .....	100

	<u>Page</u>
8. Further Discussion of N* Resonance Production ....	111
9. Helicity Conservation .....	116
10. Test of the Białas-Dabkowski-Van Hove Hypothesis .	128
11. Summary .....	141
 APPENDICES	
A. Details of the Trigger Program .....	142
B. The Kuiper Statistic .....	145
C. The $\chi^2$ Dependence of Contamination from Lower Constraint Classes .....	149
D. Estimation of the Probability of Track Inversion .....	151
E. Derivation of the BDVH Relations .....	157
 LIST OF REFERENCES .....	 171

## I. INTRODUCTION

### 1. The Diffraction Picture of Good and Walker

In hadron scattering at high energy the preeminent diffractive process is forward elastic scattering. We call it diffractive because the dominant features of this process are understandable from the viewpoint of optical diffraction. The target acts as a nearly opaque disk, extinguishing most of the incident wave. The resulting shadow acts, in the Huygens construction, as the source of secondary waves at small angles from the incident direction. We refer to certain inelastic hadron processes as diffractive dissociation. They are similar in their major properties to elastic scattering, and they may also be a result of absorption of the incident wave.

The first thorough exposition of the concept of diffractive dissociation appears in Good and Walker [1960]. They present the following optical analogue. In the case that a linearly polarized wave impinges on an opaque disk, the diffracted light has the same polarization as the incident light. Suppose instead that the disk is a Polaroid and that its axis is at  $45^\circ$  to the direction of polarization of the incident wave. The polarization of the diffracted wave is then transverse to the axis of the Polaroid. If we project the diffracted wave on axes parallel and perpendicular to the incident polarization, we find components in both directions. Diffraction by a Polaroid can thus create a new state, one not present in the incident wave.

Good and Walker discuss reactions of the type

$$A B \rightarrow A^* B \quad (1.1)$$

in which  $B$  is a nucleus,  $A$  is a meson or nucleon, and  $A^*$  is a system of two or more hadrons which are the dissociation products of  $A$ . They adopted the viewpoint that a hadron is a composite of more elementary objects. One representation of a free particle state is a superposition of states containing different numbers and kinds of constituents.<sup>†</sup>

The choice of basis is at our disposal. For representing the incident hadron,  $A$ , and the final hadrons,  $A^*$ , the appropriate basis is the set of states  $|D_i\rangle$  of one or more free particles. For understanding the propagation of the constituents of  $A$  through  $B$ , the appropriate basis is the set of states  $|C_i\rangle$  which the nuclear matter attenuates exponentially. In general the rate of attenuation would be different for each  $|C_i\rangle$ , and in general no  $|C_i\rangle$  would be a free particle state.

We represent the incident hadron  $A$  as

$$|D_1\rangle = \sum_i c_i |C_i\rangle \quad (1.2)$$

The transmitted wave is

$$|T\rangle = \sum_i n_i c_i |C_i\rangle \quad (1.3)$$

---

<sup>†</sup>Good and Walker spoke of "bare nucleons" and "bare pions," whereas today we would most likely identify the constituents with quarks. The nature of the constituents has no impact on the rest of the discussion.

with  $|\eta_i| \leq 1$ . We reproject  $|T\rangle$  into the  $|D_i\rangle$  basis obtaining

$$|T\rangle = \beta_1 |D_1\rangle + \sum_{i>1} \beta_i |D_i\rangle \quad (1.4)$$

$$\beta_i = \langle D_i | T \rangle$$

$$= \sum_j \eta_j c_j \langle D_i | C_j \rangle \quad (1.5)$$

The first term on the right of equation (1.4) interferes with the incident wave to produce elastic scattering. The second term on the right is a source of secondary waves of one or more free particles distinct from the incident hadron. It corresponds to the new polarization state which we found in considering diffraction from a Polaroid.

An elegant example of differential absorption in hadronic reactions is the regeneration of  $K_S$  from  $K_L$  in nuclear targets. The incident  $K_L$  is a superposition of equal parts of the strangeness eigenstates  $K^0$  and  $\bar{K}^0$ . The nuclei of an absorber attenuate these states at different rates, so the emergent state is a superposition of  $K_L$  and  $K_S$ .

In the foregoing analysis we ignored the phase change of the hadron wave function as it propagates through a nucleus. This approximation would be valid if the nucleus were truly a disk with no spatial

extent in the beam direction or if all the states  $|C_i\rangle$  and  $|D_i\rangle$  were energy degenerate. In the general case, however, many of the states  $|D_i\rangle$  have appreciably greater mass than the incident hadron. In particular the mass of the final state of a dissociated nucleon is greater by at least the pion mass. We can follow the argument of Good and Walker to understand how nearly degenerate the  $|C_i\rangle$  and  $|D_i\rangle$  states must be when we treat the nucleus as a three dimensional object. We view each differential layer of the nucleus as an independent source for the transmitted wave. At the time of excitation, a layer emits a superposition of the states  $|D_i\rangle$  in phase with the incident wave. Each  $|D_i\rangle$  then propagates with a frequency dependent on its mass to the shadow side of the nucleus. For masses too far from that of the incident hadron the layers contribute incoherently to the final state and a significant cross section can not develop. Diffractive dissociation, in the sense of Good and Walker, is the relatively large cross section expected when the initial and final states are so nearly degenerate that the wavelets from each layer of the nucleus are in phase when they emerge.

We make the above considerations quantitative as follows. The frequency difference of the  $A$  and the  $A^*$  systems of reaction (1.1) is proportional to their energy difference.

$$\Delta\omega = (E^* - E)/\hbar \quad (1.6)$$

The time required for the collision is

$$\Delta t = (r_A/\gamma_A + r_B/\gamma_B)/c . \quad (1.7)$$

$r_A$  and  $r_B$  are the radii of A and B, and the factors  $1/\gamma$  account for the Lorentz contraction. The coherence condition is

$$\Delta\omega \Delta t \ll 1 . \quad (1.8)$$

We evaluate  $E^*-E$  from energy-momentum conservation, and we approximate both  $r_A$  and  $r_B$  by the Compton wavelength of the pion,  $\hbar c/m_\pi$ . The general result is

$$\left( \frac{M^{*2} - M_A^2}{m_\pi} \right) \left[ \frac{M_A}{s + (M_A^2 - M_B^2)} + \frac{M_B}{s - (M_A^2 - M_B^2)} \right] \ll 1 . \quad (1.9)$$

$s$  is the square of the center-of-mass energy, and  $M^*$  is the mass of  $A^*$ . We specialize relation (1.9) for three cases which cover most situations of practical interest.

Case 1.  $M_A \ll M_B$ , B is the target, A has momentum  $P \gg M_A$ .

$$\frac{M^{*2} - M_A^2}{2m_\pi (P + M_B)} \ll 1 \quad (1.10)$$

Case 2.  $M_A \approx M_B$ ,  $M_A^2 \ll s$ .

$$\frac{M^{*2} - M_A^2}{m_\pi} \cdot \frac{2M_A}{s} \ll 1 \quad (1.11)$$

or with  $P$  the beam momentum in the rest frame of either  $A$  or  $B$

$$\frac{M^{*2} - M_A^2}{m_\pi P} \ll 1. \quad (1.12)$$

Case 3.  $M_B \ll M_A$ ,  $M_A^2 \ll s$ ,  $P$  is the momentum of  $B$  in the  $A$  rest frame.

$$\frac{M^{*2} - M_A^2}{2m_\pi P} \ll 1 \quad (1.13)$$

Relations (1.10)-(1.13) make clear that the higher the beam momentum, the higher the  $M^*$  at which diffractive dissociation may be observable.

## 2. Properties of Diffractive Dissociation

The connection between quantum number exchange and energy dependence is the feature of hadronic processes which permits us to distinguish phenomenologically between diffractive dissociation and other dissociation processes. Over the domain of presently available energies two-body cross sections behave like a power of the beam momentum.

$$\sigma(AB \rightarrow A^*B) \propto p^{-r} \quad (2.1)$$

When  $A^*$  has the same internal quantum numbers as  $A$ ,

$$r \leq 0.5 \quad (2.2)$$

whereas when  $A^*$  has different internal quantum numbers,  $r \geq 1.5$  [Fox and Quigg 1973].

All proposed models of diffractive dissociation are unanimous in support of a selection rule requiring  $A^*$  to have the same quantum numbers as  $A$ . In the absorption model of the preceding section this rule is an immediate consequence for the additive quantum numbers.<sup>†</sup> In the case that  $A$  is a meson with definite charge conjugation  $C_A$ , the model does not by itself require that  $C_{A^*} = C_A$ . The Pomeranchuk theorem, however, which asserts the equality of particle and antiparticle cross sections at infinite energy, disfavors a gentle energy dependence like (2.2) if  $C_{A^*} \neq C_A$ . Although the model of Good and Walker is relevant to  $K_S$  regeneration as we mentioned, the charge conjugation changes from  $K_L$  to  $K_S$ , and the process does not satisfy relation (2.2). [Brody et al. 1971]. A corollary of the preservation of the  $C$  quantum number is that pions dissociate only into odd numbers of pions because the dissociation products must preserve the  $G$  parity. Corresponding rules for  $K$  meson diffractive dissociation are obtainable by invoking  $SU(3)$  symmetry.

---

<sup>†</sup>These include  $B$ ,  $Q$ ,  $I^2$ ,  $I_3$  and  $S$  (baryon number, charge, isotopic spin and its projection, and strangeness).

Diffraction scattering characteristically produces an angular distribution with a sharp forward peak. The Heisenberg uncertainty principle relates the width of the peak to the size of the diffracting object.

$$P_t \approx \hbar/r \quad (2.3)$$

with  $P_t$  the momentum component transverse to the incident direction and  $r$  the radius of a black disk. Elastic scattering of hadrons from nuclei exemplifies this behavior [Blieden et al. 1975 and Apokin et al. 1976]. Good and Walker [1960] reason that since absorption is responsible for both elastic diffraction and diffractive dissociation, the production angular distributions should be similar. Differences might exist, however, because the transparency of the absorbing disk may depend on impact parameter. Some other models in the same spirit as Good and Walker yield more detailed predictions for the angular distribution in dissociation reactions [Chou and Yang 1968, Cheng and Wu 1971].

A selection rule for the internal angular momentum and parity of  $A^*$  is a more difficult matter than the selection rule for the internal quantum numbers, in part because the quantum number accounting must include the orbital angular momentum of  $A$  and  $A^*$  with respect to  $B$ . Good and Walker suggested that the orbital angular momentum would not change with the consequence that  $J^P(A^*) = J^P(A)$ . In discussions of Regge exchanges Gribov [1967] and Morrison [1968] proposed the less stringent rule

$$P(A^*)/P(A) = (-1)^{J_{A^*} - J_A} \quad (2.4)$$

as a property of Pomeron exchange (see the following section).<sup>†</sup> Both authors spoke of  $A^*$  as a resonance, and neither specifically addressed the question of whether the rule should apply to a nonresonant component of  $A^*$ . Carlitz et al. [1969] proposed yet another rule stating that a resonant  $A^*$  could belong only to certain  $SU(6)$  multiplets. Experiments have not clearly established the validity of any of these rules.

A different kind of angular momentum rule concerns the helicity of  $A^*$ . For zero degree scattering (and assuming no  $B$  spin flip) the helicity of  $A^*$  must be the same as the helicity of  $A$  purely to conserve angular momentum. When the scattering angle is nonzero, statements about the  $A^*$  helicity must refer to a particular reference frame. Experimental evidence favors helicity "conservation" in the center-of-mass frame for  $\pi p$  elastic scattering ( $A \equiv p$ ,  $A^* \equiv p$ ) and for the quasi-elastic process  $\gamma p \rightarrow \rho^0 p$  ( $A \equiv \gamma$ ,  $A^* \equiv \rho^0$ ) (references in Section IV.9). This rule does not appear to be valid for meson and baryon dissociation reactions, at least not generally. An alternative rule, helicity conservation in the  $A^*$  rest frame (t-channel helicity conservation), has some experimental support. As with the Gribov-Morrison

---

<sup>†</sup>In the case that  $A$  and  $B$  are spinless and the scattering is directly forward, the rule (2.4) follows from parity and angular momentum conservation.

rule the helicity conservation properties of  $A^*$  may depend on whether or not  $A^*$  is resonant.

### 3. The t-channel Viewpoint

Our present understanding of nondiffractive two-body processes at lab momentum  $\geq 4$  GeV is in terms of particle exchange in the t-channel. The "t-channel" of the reaction  $A B \rightarrow C D$  is the reaction  $A \bar{C} \rightarrow \bar{B} D$ . We describe both reactions with a single amplitude analytically continued in the variables

$$s \equiv \begin{cases} (P_A + P_B)^2 \\ (P_A - P_B)^2 \end{cases}, \quad t \equiv \begin{cases} (P_C - P_A)^2 & \text{s-channel} \\ (P_C + P_A)^2 & \text{t-channel} \end{cases} \quad (3.1)$$

$s$  and  $t$  are the square of the center-of-mass energy, and therefore positive, in the physical region of their respective channels, and they are the square of the momentum transfer in the other channel. When the quantum numbers of both  $A\bar{C}$  and  $\bar{B}D$ , the t-channel quantum numbers, are appropriate to the formation of a particle or resonance, the scattering amplitude has a pole close to the small  $|t|$  edge of the physical region of the s-channel reaction. The pole produces a  $d\sigma/dt$  which peaks at small  $t$ . When  $A\bar{C}$  and  $\bar{B}D$  do not have the quantum numbers of a known particle state,  $\sigma(AB \rightarrow CD)$  is comparatively small,

and a forward peak in  $d\sigma/dt$  is generally not evident.

The extension of these ideas to account for the combined effect of all possible t-channel exchanges is the Regge pole phenomenology. In the Regge analysis the amplitude for the s-channel reaction has the following integral representation when A, B, C, and D are all spinless (the Sommerfeld-Watson transformation).

$$M(s,t) = \frac{1}{2\pi i} \int_C \frac{(2L+1) P_L(-z(s,t))}{\sin \pi L} A(L,t) dL \quad (3.2)$$

The function  $z(s,t)$  is the cosine of the scattering angle of the t-channel reaction. Kinematics alone determines its form. The function  $P_L$  is the Legendre function of complex order  $L$  and degree zero. The functions obtained by restricting  $A(L,t)$  to non-negative integer values of  $L$  are the partial wave amplitudes of the t-channel reaction. The contour  $C$  encloses at least these values of  $L$ . In the theory of scattering from a potential the singularities of the function  $A(L,t)$  in the complex  $L$  plane are isolated poles. They are the Regge poles, and their positions,  $\alpha_i(t)$ , are the Regge trajectories. The rightmost pole, the one with the largest  $\text{Re } \alpha$ , dominates the behavior of  $M(s,t)$  in the large  $s$  limit.

For relativistic particle scattering the singularities of  $A(L,t)$  may in principle be more complicated than isolated poles. The simple Regge formulation, however, not only yields a moderately successful, unified

description of much of two-body scattering data [Fox and Quigg 1973] but also connects it with particle spectroscopy. A value of  $\sqrt{t}$  ( $t > 0$ ) at which  $\alpha(t)$  is a non-negative integer (of proper signature) is the expected mass of a particle or resonance, and the usual identification of a trajectory is by the name of the lowest mass state which lies on it, for example the " $\rho$  trajectory." A special trajectory, however, is the "Pomeron." All of its  $t$ -channel quantum numbers are zero, and therefore the lowest mass state on it is the vacuum. From the  $t$ -channel viewpoint the Pomeron is the basis for understanding elastic scattering and inelastic diffractive processes. The Pomeron pole is always to the right of the other Regge poles, so when its exchange is possible, it dominates in the high  $s$  regime.

The two chief results of the Regge theory are the  $s$  dependence of  $d\sigma/dt$  and factorization. When only Pomeron exchange need be considered,

$$\frac{d\sigma}{dt} = R(t) s^{2\alpha_P(t)-2} \quad (3.3)$$

with  $\alpha_P(t)$  the trajectory of the Pomeron. This same  $s$  dependence obtains regardless of the identities of the initial and final state particles. The content of factorization is that  $R(t)$  is a product of two factors, one depending only on the  $t$ -channel initial state, the other depending only on the  $t$ -channel final state.

$$R_{AB \rightarrow CD} = R_{A \rightarrow C} R_{B \rightarrow D} \quad (3.4)$$

Experimentally testable corollaries take the form

$$\frac{d\sigma/dt (AB \rightarrow A^*B)}{d\sigma/dt (AB \rightarrow AB)} = \frac{d\sigma/dt (AC \rightarrow A^*C)}{d\sigma/dt (AC \rightarrow AC)} \quad (3.5)$$

Beyond factorization Regge theory leaves considerable freedom in the form of the functions  $R(t)$ .

For the understanding of reactions in which the quantum numbers forbid Pomeron exchange, the Regge phenomenology has no peer. The Pomeron, however, has been an object of substantial controversy. If the absorption mechanism described in Section I.1 is a correct view of diffractive reactions, then it is not clear why the Pomeron singularity should have the simplicity of a Regge pole. The predictive powers of the two viewpoints do not have much overlap, so experiment does not easily discriminate between them. A recent review of hadron diffraction theory emphasizing the t-channel viewpoint is available in Abarbanel [1976].

#### 4. The Deck Mechanism

Drell and Hiida [1961] and Deck [1964] proposed the following mechanism as a contributor, at least, to diffractive dissociation. One of the incident particles dissociates virtually into two pieces, for example  $\pi \rightarrow \rho\pi$  or  $p \rightarrow \pi p$ . One of the pieces then scatters elastically from the other incident particle resulting in a three particle state. The diagram of Figure 1 represents the amplitude for this process.

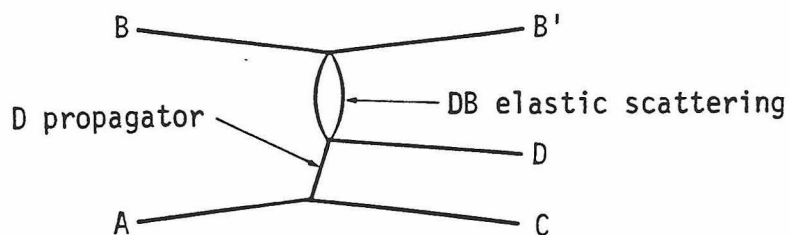


FIG. 1. Diagram representing the Deck mechanism.

Since the fraction of A's time which it spends as a virtual state of C and D is independent of beam energy, the energy dependence of the process is like the energy dependence of DB elastic scattering and is therefore diffractive.

A characteristic of the Deck mechanism is that it produces a broad enhancement near threshold in  $d\sigma/dM^2(CD)$  without the need for resonance formation in the CD system. We illustrate this in Figure 2 using  $d\sigma/dM^2$  for a particular Deck model fitted to data of the reaction  $pp \rightarrow p(n\pi^+)$  [Berger 1968].

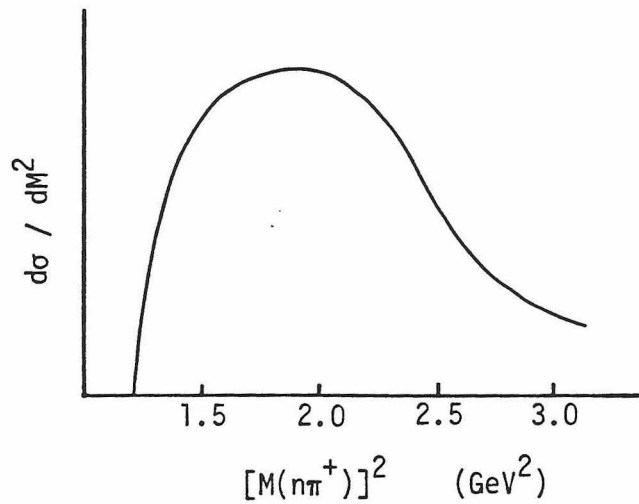


FIG. 2.  $d\sigma / dM^2$  for a Deck model.

Experimentally the  $d\sigma/dM$  for the diffractive dissociation of any incident hadron,  $\pi$ ,  $K$ , or nucleon, exhibits a threshold enhancement ( $A_1$ ,  $Q$ , or  $N^*$ ). Deck models tend, however, to overestimate its width. The Deck mechanism also predicts the distribution in the variable  $t(BB')$  [Oh and Walker 1969]. In a fit of the cross section to the form

$$\exp[-b(M)t(BB')]$$

the expected result is a  $b(M)$  which decreases dramatically with increasing  $M$  in the regime just above threshold.

From the  $t$ -channel viewpoint (preceding section) the Deck mechanism is just a special case in which the Pomeron exchange mediates the  $BD$  elastic scattering. By adding details of the dynamics at the  $A$  vertex, the model yields specific behavior in  $M(CD)$  and  $t(BB')$  which

is not an intrinsic part of Pomeron phenomenology.

### 5. Some Published Data at Very High Energy

We do not undertake in this section a general review of the experimental work on diffractive dissociation. Several such reviews are available [Derrick 1975, Miettinen 1975, Leith 1974, Gramenitskii and Novak 1974, and works they reference]. We merely want to point to four recent published experiments which demonstrate dissociation of the nucleon into exclusive channels at 20 GeV/c to 1000 GeV/c equivalent beam momentum. All four experiments used electronic detection methods.

The first group [O'Brien et al. 1974] studied the reactions

$$n C \rightarrow p \pi^- C \quad (5.1)$$

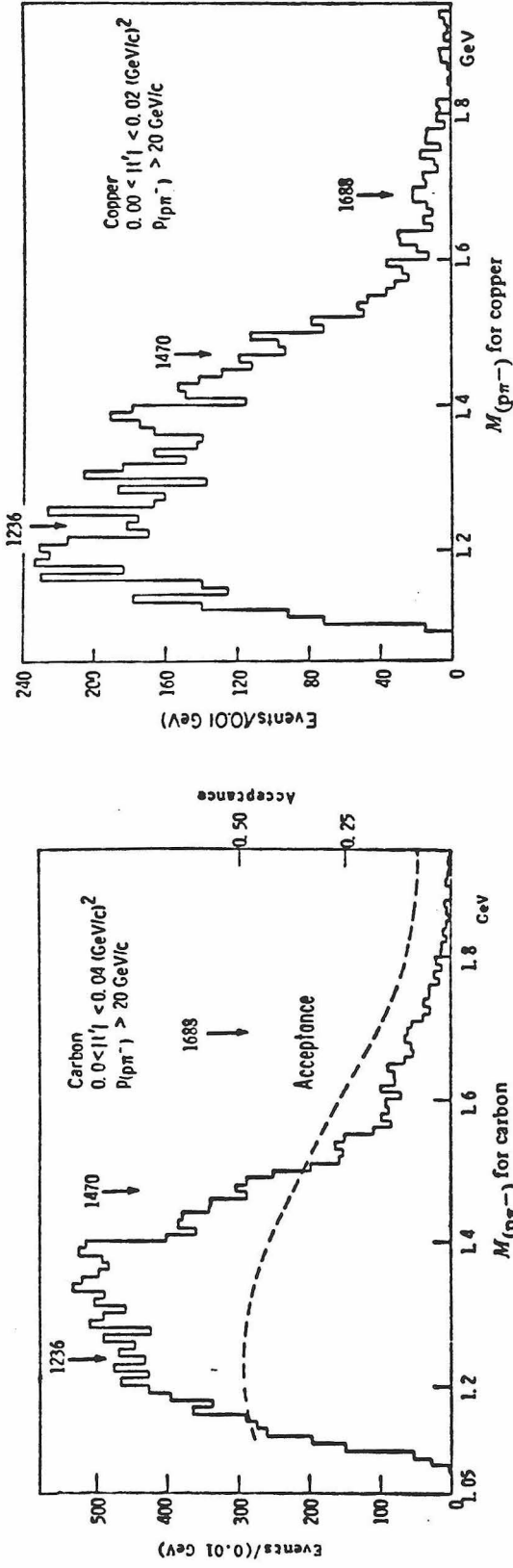
$$n Cu \rightarrow p \pi^- Cu . \quad (5.2)$$

The spectrum of their neutron beam peaked at 25 GeV/c and was 8 GeV/c wide (FWHM). We reproduce some of their results in Figure 3. The most noteworthy feature of this data is that none of the well established  $N^*$  resonances appear as obvious peaks.

The second experiment [Edelstein et al. 1977] obtained data for the reactions

$$p Z \rightarrow p \pi^+ \pi^- Z \quad (5.3)$$

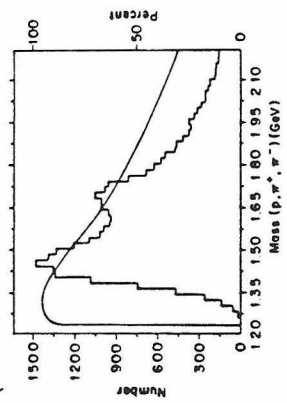
with  $Z$  representing Be, C, Al, Ti, Cu, Ag, Ta, Pb and U. The beam



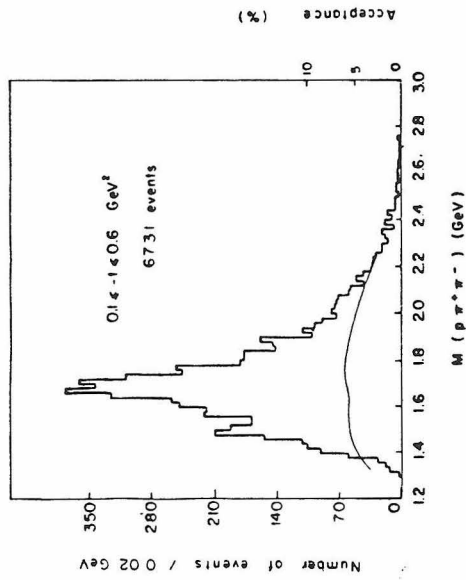
Coherent production cross section versus  $M_{(p\pi^-)}$

Target	$1.078 < M_{(p\pi^-)} < 1.5$ GeV	$1.4 < M_{(p\pi^-)} < 1.6$ GeV	$1.5 < M_{(p\pi^-)} < 1.8$ GeV
C	$1.00 \pm 0.27$ mb	$0.37 \pm 0.13$ mb	$0.23 \pm 0.07$ mb
Cu	$2.27 \pm 0.47$ mb	$0.73 \pm 0.19$ mb	$0.36 \pm 0.16$ mb

FIG. 3. Figures and table from O'Brien et al. [1974].



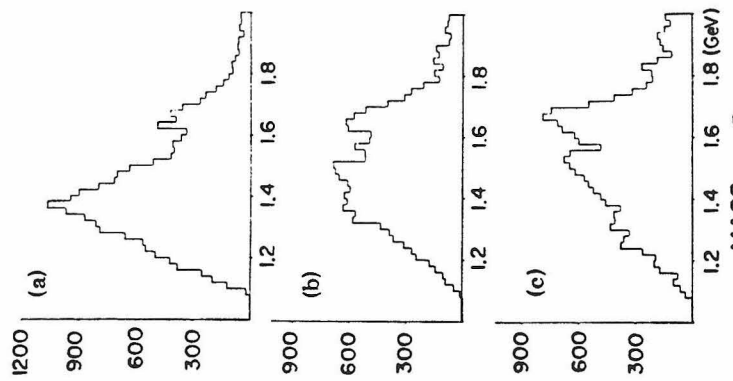
Uncorrected  $p\pi^+\pi^-$  mass spectrum for  $p + C \rightarrow p\pi^+\pi^- + C$  at 22.5 GeV with  $-t' < 0.04$  (GeV/c) $^2$ . Geometrical acceptance of the spectrometer vs mass is superimposed.



Experimental distribution in  $M(p\pi^+\pi^-)$  for  $0.1 \leq -t \leq 0.6$  GeV $^2$ . The smooth curve is the acceptance.

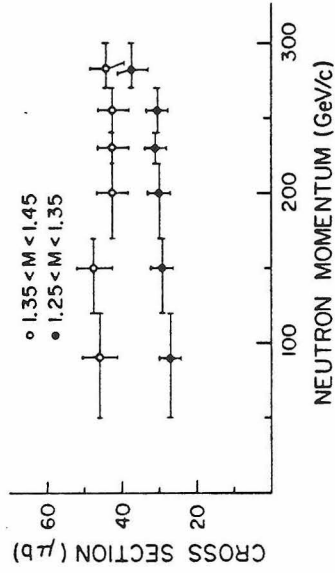
FIG. 4. Figure from Edelman et al. [1977].

FIG. 5. Figure from Webb et al. [1976].



Mass spectra of  $p\pi^-$  pairs in hydrogen, integrated over a 50–300 GeV/c neutron momentum band, displayed as a function of  $t$ . (a), (b), and (c) correspond to  $|t|$  bands of 0.02–0.08, 0.08–0.20, and 0.20–1.00 GeV<sup>2</sup>, respectively.

a



Energy dependence of the cross section for two low-mass intervals. Data are shown integrated over  $0.02 < |t| < 1.0$  GeV<sup>2</sup>. The absolute normalization is uncertain by about  $\pm 20\%$ .

b

FIG. 6. Figures from Biel et al. [1976].

momentum was 22.5 GeV/c. In Figure 4 we show their  $p \pi^+ \pi^-$  mass spectrum for the carbon data. Peaks are evident at about 1.4 GeV and 1.68 GeV. Whereas the lower peak could as well be a kinematic enhancement (see the preceding section), the upper peak is more suggestive of a resonance.

The reaction



was the subject of the third experiment [Biel et al. 1976]. The neutrons delivered by a neutral beam at Fermilab had momenta in the range 50-300 GeV/c. In Figure 6 we reproduce the  $p \pi^-$  mass spectrum and the cross section as a function of neutron momentum. The mass spectrum suggests some resonance production in the vicinity of 1.65 GeV. Figure 6b shows that the energy dependence of the cross section is indeed as expected for a diffractive process.

Our final example is an experiment conducted at the CERN-ISR [Webb et al. 1975] to study the reaction



The momenta of the colliding beams were both 22 GeV/c which is equivalent to a beam momentum of 1000 GeV/c for a fixed target experiment. The mass spectrum obtained appears in Figure 5. This spectrum suggests resonance production near 1.7 GeV even more strongly than the analogous

experiment on nuclei (see Figure 4 ). The relative dearth of events at the low mass end is most likely an artifact of the  $t$  selection. The Fermilab data (Figure 6 ) shows how sensitive the mass spectrum can be to the  $t$  cut. Much of the reaction (5.5) cross section corresponds to  $|t| < 0.1$  which is the lower limit of the ISR data. To estimate this cross section including the unobserved small  $|t|$  region, Webb et al. extrapolated their observed  $t$  distributions to  $t = 0$ . Their result is  $0.33 \pm 0.1$  mb at  $P_{\text{lab}} = 1000$  GeV/c and  $0.34 \pm 0.1$  mb at  $P_{\text{lab}} = 1500$  GeV/c. The absence of strong energy dependence characterizes the process as diffractive.

Taken together these four experiments show that, at high energy, nucleons dissociate into exclusive channels with cross sections of the order of  $200 \mu\text{b}$  and that the cross sections are roughly independent of energy. Three of them suggest that a small part of the cross section is attributable to resonance production.

## 6. Intent of the Present Experiment

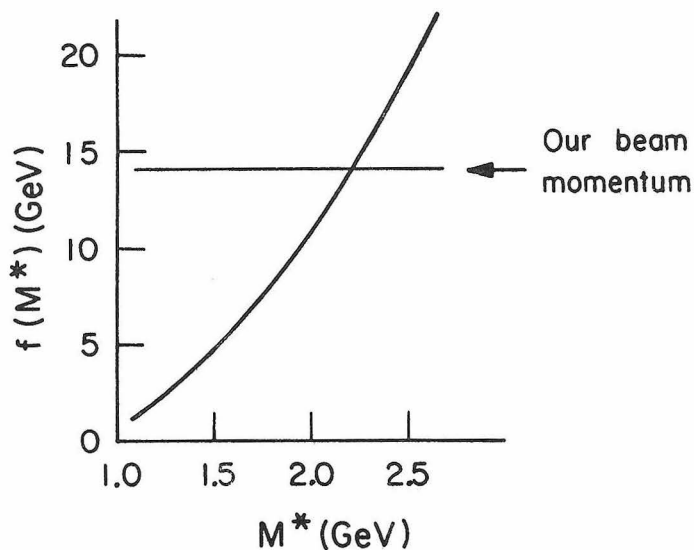
Prior to the proposal of this experiment, missing mass measurements [Belletini et al. 1965, Anderson et al. 1966, Foley et al. 1967] had provided large sample mass distributions and differential cross sections for nucleon diffractive dissociation. Peaks in the mass spectra suggested resonance production but could reveal nothing about their decay. More information was necessary to confront several questions. 1) How much of diffractive dissociation was ascribable to resonance production and how much to the Deck mechanism? 2) Which resonances could diffract

produce? 3) Did their production angular distributions have forward dips? 4) What was the status of the Gribov-Morrison and the helicity conservation rules? Attacks on these questions required studies of the angular distributions and correlations of the dissociation products. For this kind of work the superior  $4\pi$  detection efficiency of a bubble chamber is a considerable advantage, but the individual exposures then available were not large enough. The objective of the present experiment was a manyfold increase in the number of photographs of proton diffractive dissociation.

We pursued this objective by means of a synergistic combination of spark chamber and bubble chamber techniques. In the traditional mode of operation bubble chambers produced a picture of every beam pulse regardless of what sort of events occurred. This mode was not an economical way to obtain a large sample of a particular channel which was but a small fraction of the total cross section. The dissociation channels  $p \rightarrow p \pi^0$ ,  $p \rightarrow n \pi^+$ , and  $p \rightarrow p \pi^+ \pi^-$  represent about 5% of a total cross section of 26 mb for  $\pi^- p$  interactions at 14 GeV. We partially remedied the selectivity problem of the bubble chamber by augmenting it downstream with a wire spark chamber spectrometer. The spectrometer discriminated proton diffractive dissociation events both from elastic scatters and, by its limited acceptance, from much of the rest of the inelastic cross section. The bubble chamber camera produced a picture only on pulses for which the spectrometer indicated the occurrence of a desirable event.

By these means we collected film containing about 45 events/ $\mu\text{b}$  for the part of the cross section that we wished to investigate. What we achieved was about one half of our original goal. Chapters II and III document our methods, and in Chapter IV we present some analyses of the  $\pi^- \pi^- \pi^+ p$  final state.

Before proceeding we issue one caveat. From the point of view of the absorption mechanism (Section I.1) our beam momentum is uncomfortably low. The inequality (1.13) has the form  $f(M^*)/P \ll 1$ . Below we graph  $f(M^*)$  and compare it with 14 GeV/c, the highest beam momentum available to the experiment. That the graphs cross at a comparatively low value of  $M^*$  is certainly unfavorable. This situation is not directly relevant to our own analyses because in Chapter IV we do not explicitly treat our final state as a consequence of absorption.



## II. EXPERIMENTAL APPARATUS

## 1. Overview

The major components of the apparatus were the 40" hydrogen bubble chamber at the Stanford Linear Accelerator Center (SLAC), a large aperture magnetic spectrometer installed downstream of the bubble chamber, a beam line to deliver  $\pi^-$  mesons from the primary target, and a Xerox Sigma 2 computer. Briefly these components functioned together as follows. Prior to delivery of a beam pulse the bubble chamber began its expansion, and the cycle followed its normal course regardless of the scattering of any beam particles. The computer controlled only the bubble chamber camera. On most pulses the film remained unexposed. If an appropriate interaction did occur, some scintillation counters detected the forward scattered particle and triggered the wire spark chambers of the spectrometer. The spark chamber electronics digitized the spark positions and transferred this information to the computer. During the time required for bubbles to develop in the chamber, the computer analyzed the spark data to ascertain the momentum of the forward scattered track. If this momentum was within a preselected range, the computer signaled the bubble chamber camera to expose the film. Whenever the computer received spark digitizations it recorded them on magnetic tape.

In the rest of this chapter we describe the apparatus and the trigger operation in greater detail.

## 2. The Secondary Beam Line

The SLAC accelerator delivered an intense beam of 19 GeV electrons to a 30 cm beryllium wire target. The function of the beam line was to form from the secondary emission of the target a low intensity 14 GeV  $\pi^-$  beam and transport it to the bubble chamber. In Figure 7 we show a schematic of the secondary beam line. It collected particles emerging at 17 mrad from the primary beam direction and had an aperture of about 50  $\mu$ sr. The beam line had two points which were foci in both the horizontal and vertical planes. At the first focus the beam passed through 1.1 radiation lengths of lead to degrade the momentum of the electron component. Final momentum definition occurred at a one meter iron slit at the second focus. The last leg of the beam line gave the beam a ribbon like conformation at the bubble chamber. The quadrupoles made the beam parallel in the vertical plane and focussed at the bubble chamber in the horizontal plane. The optical axis of the bubble chamber camera was horizontal, so the camera viewed the broad dimension of the beam. The dipole magnets in the last leg steered the beam to the correct position and angle for passage through the bubble chamber and spectrometer. In Table II.A we give the characteristics of the beam at the bubble chamber. The information on contamination from  $K^-$ ,  $\bar{p}$ , and  $\mu^-$  comes from Boyarski et al. [1968]. The information on  $e^-$  contamination comes from our own measurement with a shower counter. The method ultimately used to normalize the data (see Section IV.4) is insensitive to  $\mu^-$  and  $e^-$  contamination.

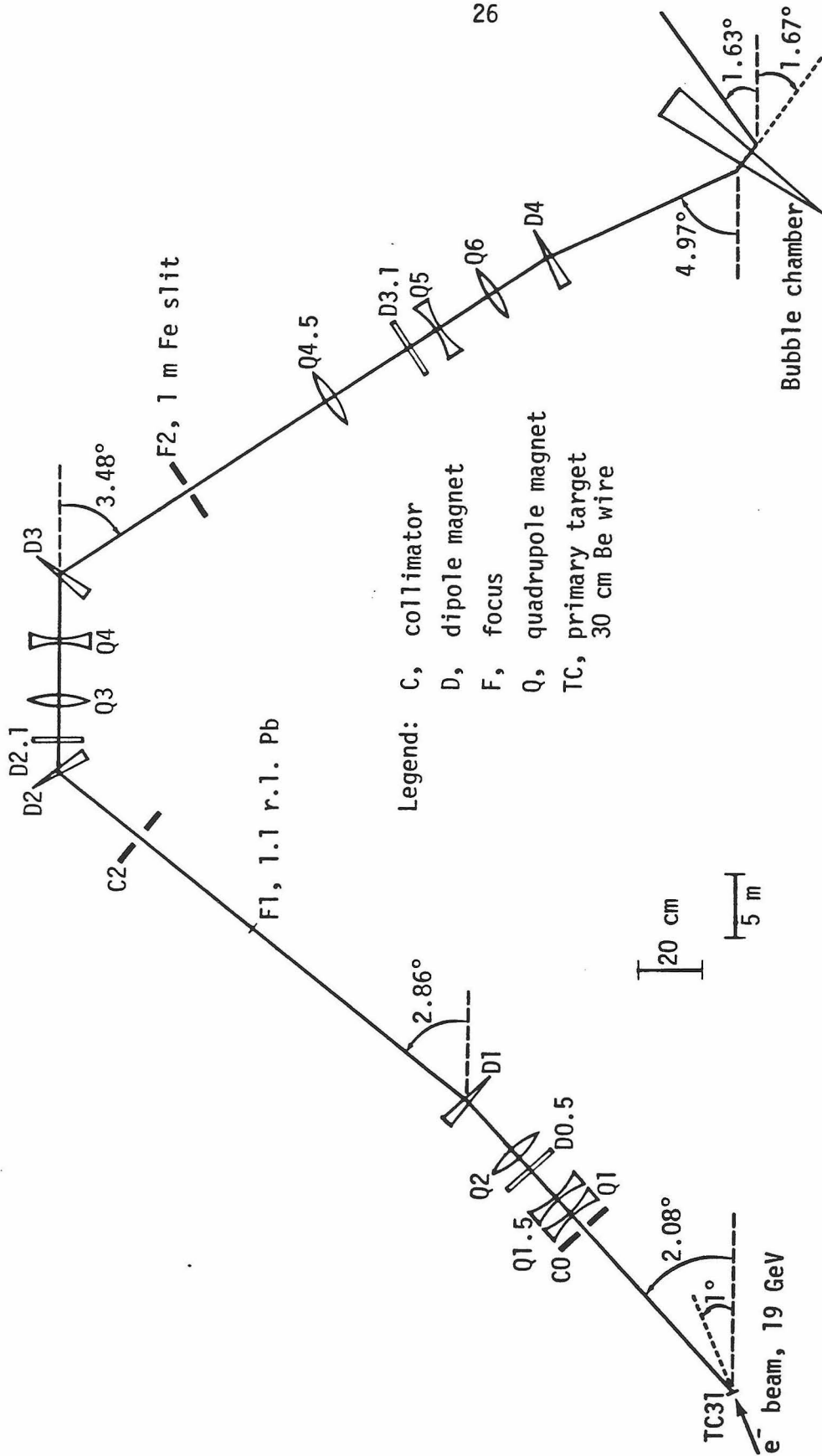


FIG. 7. Elevation view of the secondary beam line. The function of this beam line was to form

a 14 GeV/c  $\pi^-$  beam and transport it to the bubble chamber. All major bends were in the vertical plane. The field strengths in the horizontal trim magnets D0.5, D2.1, and D3.1 were nominally zero.

TABLE II.A.--Beam parameters at the bubble chamber.

---



---

Momentum	14 GeV
$\Delta P/P$	$\pm 0.5\%$
Intensity	$\approx 8\pi^-/\text{pulse}$
Pulse duration	$\approx 1.2 \mu\text{s}$
Horizontal dimension (5% points)	1.0 cm
Vertical dimension (5% points)	15 cm
Horizontal divergence ( $\sigma$ )	$\approx 2.0 \text{ mrad}$
Vertical divergence ( $\sigma$ )	$< 1.0 \text{ mrad}$
Contamination: $K^-$	$\approx 2\%$
$\bar{p}$	$< 0.2\%$
$\mu^-$	$< 5\%$
$e^-$	$< 3\%$

---



---

### 3. The Bubble Chamber

The chamber was a cylinder of diameter 110 cm and depth 45 cm in a magnetic field of 27 kG. Its axis was horizontal and transverse to the beam direction. The camera provided three views of the chamber from a position 200 cm along the chamber axis from the beam. The lens centers were at the vertices of a 70 cm equilateral triangle, and the optical axis of each view was parallel with the chamber axis.

The chamber had two features, not common to most other bubble chambers, which particularly suited it to this experiment. One was its beam exit windows, and the other was its capability for rapid cycling. In addition to the usual thin windows on the entrance side, this chamber had 20 cm diameter thin windows on the exit side.<sup>†</sup> Material intervening between the hydrogen and the spectrometer has two adverse effects. It scatters beam particles into the sensitive region of the spectrometer causing unwanted triggers, and it degrades the spectrometer angle measurement of tracks scattered in the hydrogen. The interaction rate in the windows was equivalent to the rate in 18 cm of liquid hydrogen, and multiple scattering in the exit windows corresponded to multiple scattering in 94 cm of hydrogen. The thin windows were a prerequisite to the successful operation of the spectrometer.

The SLAC accelerator normally generates 360 pulses of electrons each second, so it can supply beam to a bubble chamber as rapidly as the chamber can pulse. The repetition rate of the chamber is therefore the limiting factor in the data rate. At the outset of data taking the 40" chamber operated at two expansions/sec, and at the conclusion a rate of five expansions/sec was achievable. The overall result was that the experiment logged  $7 \times 10^6$  expansions in ten weeks of data accumulation (including down time), an average of one expansion/sec.

---

<sup>†</sup>A separate enclosure maintained a vacuum around the chamber. The vacuum tank as well as the chamber had thin windows.

The bubble chamber, while well suited to the accelerator and to this experiment, also imposed the chief constraint on the trigger apparatus. The chamber begins its expansion about 10 msec prior to arrival of the beam particles. By beam time the liquid hydrogen is close to the minimum in the pressure curve. Growth of bubbles then requires about 3 msec. At the end of this interval high intensity lamps flash to expose the film. The chamber returns to its equilibrium state in 20 msec and then idles pending the arrival of the next beam pulse. The triggerable part of this process is the flash of the high intensity lamps. The time available to the trigger mechanism to reach a decision is the 3 msec bubble growth time.

#### 4. The Spectrometer

A novel aspect of this experiment was the operation of a spectrometer in conjunction with the bubble chamber. By measuring the momentum of fast forward secondaries, the spectrometer together with the Sigma 2 computer contributed in two ways, both of them indispensable to the overall success of the experiment. First, it triggered the bubble chamber flash tubes when it detected a forward track with momentum in the desired range. Second, the spectrometer measurement of momentum was far more precise than the corresponding bubble chamber measurement. The increased precision is most important for reactions containing a single neutral particle in the final state. It reduces ambiguity in the identification of these events to a tolerable level.

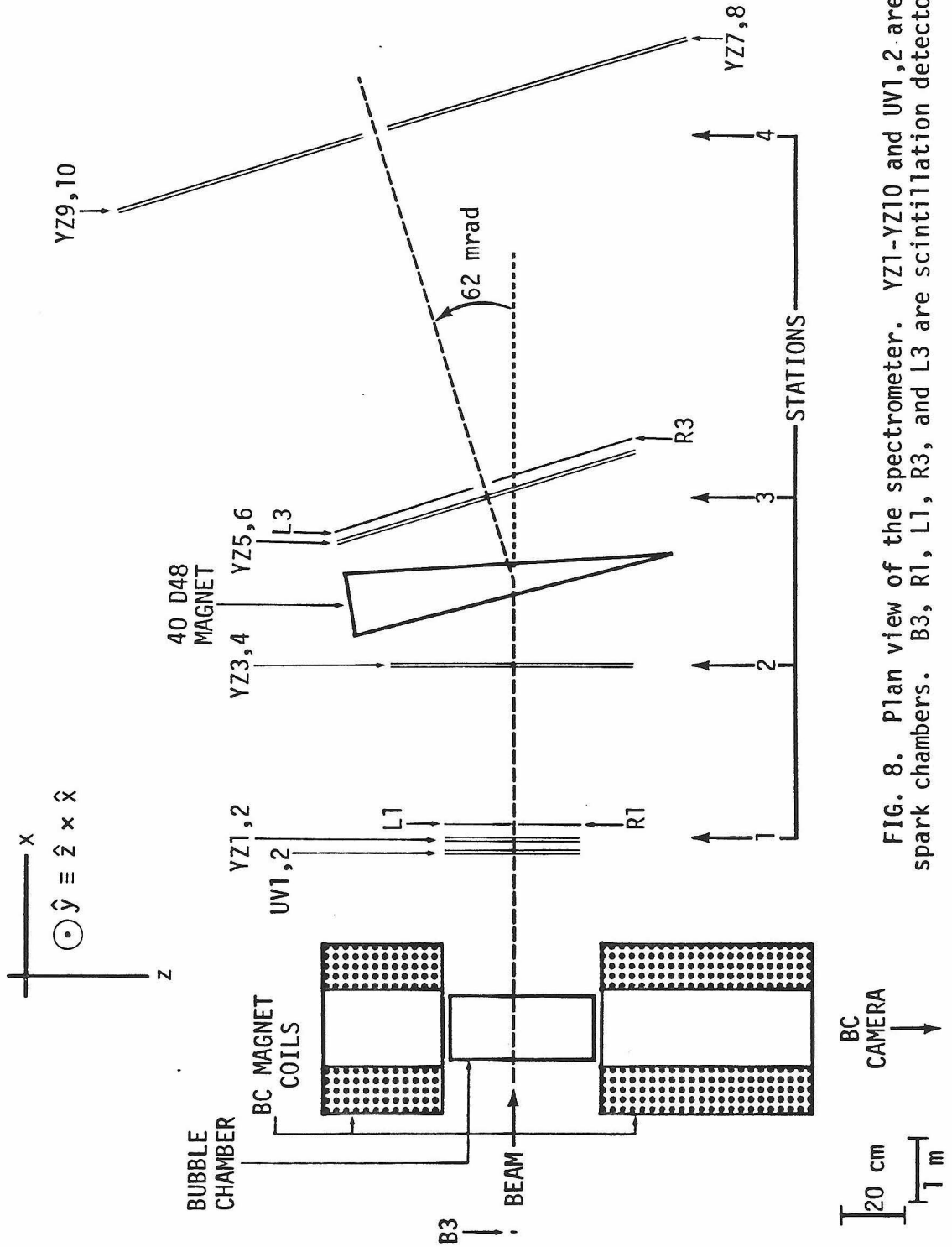


FIG. 8. Plan view of the spectrometer. YZ1-YZ10 and UV1,2 are wire spark chambers. B3, R1, L1, R3, and L3 are scintillation detectors.

We describe the spectrometer with the assistance of Figure 8. It consisted of a dipole magnet, wire spark chambers to measure particle trajectories upstream and downstream of the magnet, and scintillation counters for triggering. We give the relevant parameters of the magnet in Table II.B.

TABLE II.B.--Parameters of the spectrometer magnet.

Horizontal aperture (z)	102 cm
Vertical aperture (y)	38 cm
Field strength	28 kG-m
Sextupole coefficient	$1.1 \times 10^{-5} \text{ cm}^{-2}$
Bend angle of 14 GeV particles	62 mrad

R1, L1, R3, and L3 are labels of plastic scintillation counters. The scintillator dimensions, horizontal (z) first, were 20 cm  $\times$  24 cm at station 1 and 46 cm  $\times$  43 cm at station 3. Unscattered beam particles passed through a 2.5 cm horizontal separation between R1 and L1 and a 5.6 cm separation between R3 and L3. A coincidence of one of R1 and L1 with one of R3 and L3 indicated that a scattered particle had passed through the spectrometer magnet.

This coincidence produced a trigger for the twelve wire spark chambers, YZ1 - YZ10, UV1, and UV2. We placed the chambers in pairs

at four locations designated station 1 through station 4. At station 1 adjacent to the yoke of the bubble chamber magnet were both a YZ pair and the UV pair. Station 4 required two YZ pairs, one on each side of the beam. Pairing the chambers ensured a high efficiency for the detection of at least one spark at each station. The efficiency of individual chambers ranged from 90% to 99%. All chambers were of the same physical size and the same basic design. We give their common characteristics in Table II.C.

TABLE II.C.--Common characteristics of the spark chambers.

Type	Wire plane
Maximum sensitive area	1 m × 1 m
Plane separation	1.0 cm
Relative orientation of wires	90 deg
Wire spacing	0.05 cm
Gas fill	80%/20% Ne-He at atmospheric pressure
High voltage pulse generator	Thyratron
Readout mechanism	Magnostriuctive ribbon
Resolution ( $\sigma$ )	≈0.03 cm

To minimize the occurrence of extraneous sparks in the chambers we reduced their sensitive areas to match the apertures set by the bubble

chamber and the spectrometer magnet. We simply severed the connection of chamber wires with their bus bar. By the same technique we deadened vertical bands through which the beam traversed the YZ chambers at stations 1, 2, and 3. At station 4 the beam traversed a gap between chamber pairs YZ7,8 and YZ9,10. To deaden the beam-illuminated area of the UV chambers we inserted slabs of polyurethane foam between the wire planes.

The physically relevant parameters of a forward scattered track are its momentum and the scattering angle. For fixed values of only these parameters some trajectories successfully negotiate the spectrometer while others miss an aperture or traverse the dead region at one of the stations. The resulting detection probability depends heavily both on the momentum and the scattering angle, and we must account for it in the analysis of the data. We discuss this issue in detail in Section IV.5.

The most important measurement which the spectrometer supplied was the bend angle in the magnet. The resolution ( $\sigma$ ) for this measurement was 0.25 mrad. The contributions from position error of the spark chambers and from multiple scattering in the chambers and intervening material were nearly equal. The relation of momentum to bend angle is

$$\frac{P}{14 \text{ GeV}} = \frac{62 \text{ mrad}}{\theta} . \quad (4.1)$$

From this follows the relation for the error of the momentum.

$$\begin{aligned}\Delta P &= \frac{p^2}{14 \text{ GeV}} \cdot \frac{\Delta\theta}{62 \text{ mrad}} \\ &= p^2 \times 2.9 \times 10^{-4} \text{ GeV}^{-1}\end{aligned}\tag{4.2}$$

$\Delta P$  is  $\approx 60$  MeV at 14 GeV and  $\approx 30$  MeV at 10 GeV.

## 5. Triggering and the Role of the Online Computer

The logic equation for the spark chamber trigger signal was

$$\text{SCTRIG} = \text{GATE} \cdot (\text{R1} + \text{L1}) \cdot (\text{R3} + \text{L3})\tag{5.1}$$

The factor GATE was true for the duration of every beam pulse. The SCTRIG signal was fanned out to the high voltage pulse circuits at each chamber. Because of cable delays and the rise time of the HV pulsers, sparks developed roughly 0.4  $\mu\text{sec}$  after the triggering particle traversed the spectrometer. The memory time of the chambers easily accommodated this delay. Because of the delay, however, and because the beam "spill" was so short, a second track was sometimes observable in the spark chambers.

Figure 9 shows schematically the electronics used to digitize spark coordinates. We use the term "wand" to refer to a magnetostrictive ribbon, its mechanical support, the pickup coil, and integral preamp. Near the ends of each wand at precisely known locations on the chambers were fiducial wires. Synchronously with the application of the high voltage, current pulses in the fiducial wires

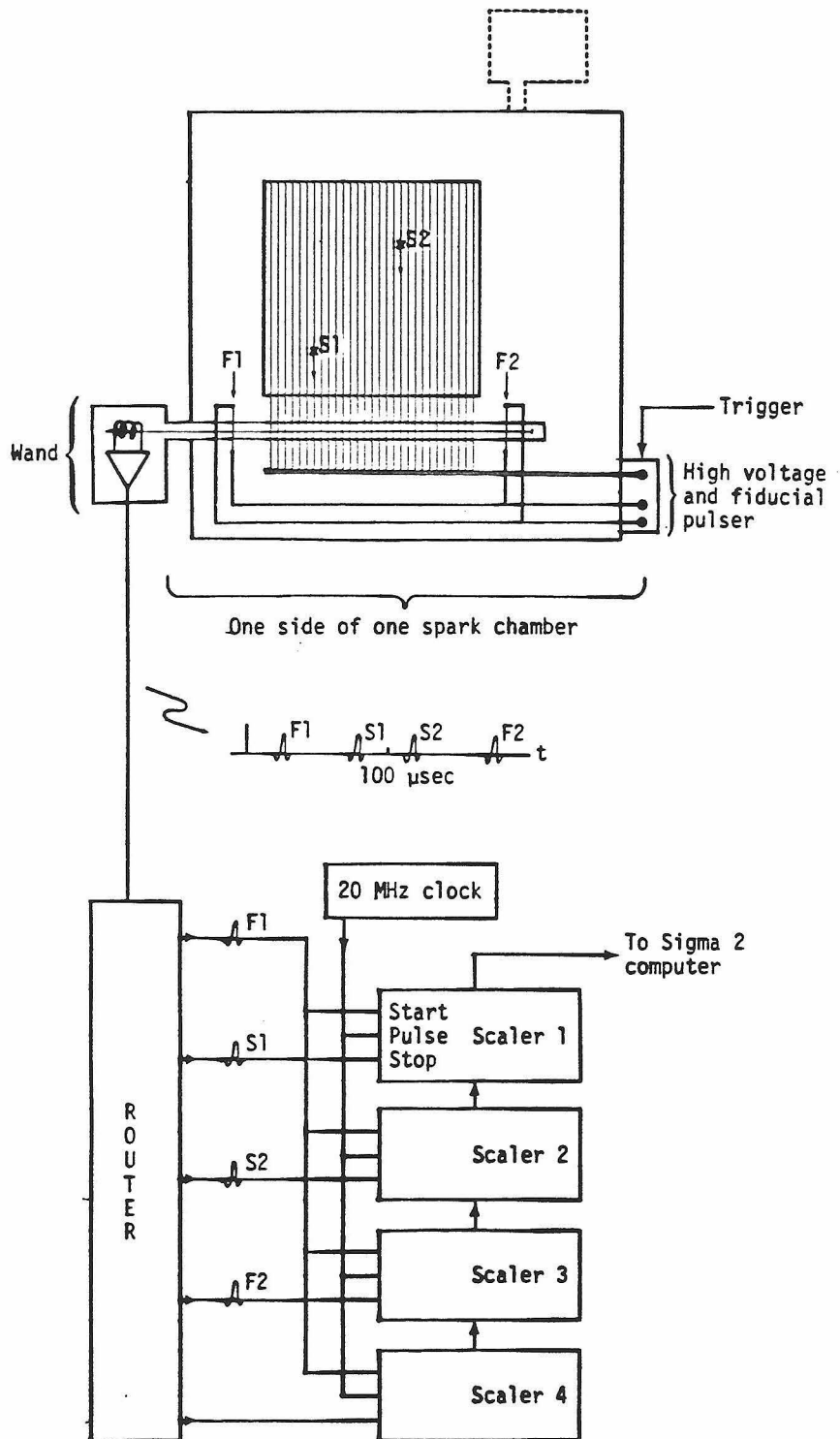


FIG. 9. Schematic of the spark digitizing electronics. F1 and F2 are pulses from the fiducial wires, and S1 and S2 are pulses from sparks.

initiated acoustic pulses in the magnetostrictive ribbon. Because the acoustic pulse propagates along the ribbon with uniform velocity, the position of the source of a pulse corresponds to a time of arrival at the pickup coil. The first fiducial pulse from a wand started four 20 MHz 12 bit scalars associated with that wand. Succeeding pulses stopped the scalars one by one. The last one to stop digitized the time of arrival of the second fiducial except on occasion when a chamber produced more than three sparks. The computer maintained a running average of the digitizations obtained for the fiducial, and this average established the effective propagation velocity in the magnetostrictive ribbon.

We developed computer codes for the online Sigma 2 computer to perform three primary tasks. One was to fetch the spark coordinates from the spark chamber electronics and to record these on magnetic tape. A second was to do some minimal analysis of the data to ensure that the spectrometer was functioning satisfactorily. The third task, and the most noteworthy, was to select pulses on which to trigger the bubble chamber flash tubes. The design of this algorithm required great care so as to satisfy the 3 msec time constraint.<sup>†</sup>

The trigger algorithm deals with the reaction



---

<sup>†</sup>W. Ford was chiefly responsible for its development.

The system  $X$  includes one nucleon and an arbitrary number of mesons. The primary objective is to generate a trigger when  $X$  includes at least one pion. The cross section for elastic scattering is about a factor of three larger than the cross section for the dissociation reactions which we seek to study. An algorithm must identify elastics with efficiency greater than 93% in order that contamination of the triggers be less than 20%.

We use the notation  $M_p$ ,  $M_X$  for the masses of the proton and  $X$ , and we use  $P_b$  and  $P_f$  for the magnitude in the lab frame of the momenta of the beam particle,  $\pi^b$ , and the secondary particle measured in the spectrometer,  $\pi^f$ . Neither of these momenta is ever less than 6.5 GeV. For this discussion we can safely approximate the energies of the pions by their momenta. Conservation of 4-momentum in the reaction yields an expression for  $M_X^2$ .

$$M_X^2 = M_p^2 + 2 M_p (P_b - P_f) + t \quad (5.3)$$

with  $t$  the square of the 4-momentum transfer from  $\pi^b$  to  $\pi^f$ . An adequate approximation for  $t$  is

$$t \approx - P_b P_f (\phi_y^2 + \phi_z^2) \quad (5.4)$$

$\phi_y$  and  $\phi_z$  are the vertical and horizontal projections of the scattering angle.<sup>†</sup>

---

<sup>†</sup>Projecting an angle in this way is also an approximation which is satisfactory for our scattering angles of  $\lesssim 60$  mrad.

We determine  $P_f$  from its bend angle in the spectrometer according to the relation

$$P_f \theta_f = \int B_y d\ell . \quad (5.5)$$

The right hand side is the integral of the  $y$  component of the magnetic field over the trajectory through the spectrometer magnet. We can approximate this integral by the sum of the dipole term and a sextupole term.

$$\begin{aligned} P_f \theta_f &\approx P_0 \theta_0 [1 + b(d_z^2 - d_y^2)] \\ &\approx P_0 \theta_0 + P_f \theta_f b(d_z^2 - d_y^2) \end{aligned} \quad (5.6)$$

$P_0$  is the design momentum of the beam, and  $\theta_0$  is the bend angle of an on-axis pion with this momentum. The quantities  $d_z$  and  $d_y$  are the horizontal and vertical displacements of the trajectory from the  $x$  axis of the magnet. The coefficient  $b$  is positive with magnitude about  $1.1 \times 10^{-5} \text{ cm}^{-2}$  for the magnet. In analogy with the angle  $\theta_f$  we may define the angle  $\theta_b$  which is the bend angle that the spectrometer would measure for a beam track.

$$P_b \theta_b = \int B_y d\ell = P_0 \theta_0 \quad (5.7)$$

$\theta_b$  is of course not measurable for individual events. We have measured

the average,  $\bar{\theta}_b$ , by using a small dipole magnet upstream of the bubble chamber to steer the beam, at reduced intensity, into the active area of the spark chambers.

We now combine relations (5.3)-(5.7) to obtain

$$\begin{aligned} M_x^2 - M_p^2 &= 2 M_p P_0 \theta_0 \left( \frac{1}{\bar{\theta}_b} - \frac{1}{\theta_f} \right) - 2 M_p P_f b (d_z^2 - d_y^2) - P_b P_f (\phi_y^2 + \phi_z^2) . \end{aligned} \quad (5.8)$$

In a loose approximation which ignores the dimensions of the beam and the bubble chamber we can write

$$d_y \approx x_M \phi_y \quad , \quad d_z \approx x_M \phi_z \quad . \quad (5.9)$$

$x_M$  is the distance from the bubble chamber to the spectrometer magnet.

Using relations (5.9) in a rearrangement of equation (5.8) we have

$$M_x^2 - M_p^2 = 2 M_p P_0 \theta_0 \left( \frac{1}{\bar{\theta}_b} - \frac{1}{\theta_f} \right) - P_f C_z \phi_z^2 + P_f C_y \phi_y^2 \quad (5.10)$$

wherein

$$C_y = 2 M_p b x_M^2 - P_b = -4 \text{ GeV} \quad (5.11)$$

$$C_z = 2 M_p b x_M^2 + P_b = 24 \text{ GeV} . \quad (5.12)$$

For the sake of speed the trigger program operated with only

the  $z$  coordinates of the sparks. This information is sufficient to compute only the first and second terms on the right hand side of equation (5.10). The second term may be as large as  $1.0 \text{ GeV}^2$ , and neglecting it in the trigger program would have resulted in too much contamination from elastic scatters. Because of the dimensions of the magnet aperture, the maximum value of  $\phi_y$  is about one half the maximum of  $\phi_z$ . On this account and because  $|C_y| \ll |C_z|$ , the third term in equation (5.10) is  $\leq 0.08 \text{ GeV}^2$ . Since the threshold in  $M_x^2 - M_p^2$  for single pion production is  $0.28 \text{ GeV}^2$ , neglect of the third term in the trigger creates no difficulties.

In Appendix A we describe in detail the steps taken by the trigger program to identify tracks corresponding to inelastic events. In Figure 10 we show a histogram of the time required for the trigger program to reach a decision. For a small fraction of the spark chamber triggers, the trigger program required more than 3 msec to conclude. In these cases if the program called for a picture, the picture was lost. In Table II.D we give statistics of the data acquisition and the operation of the trigger.

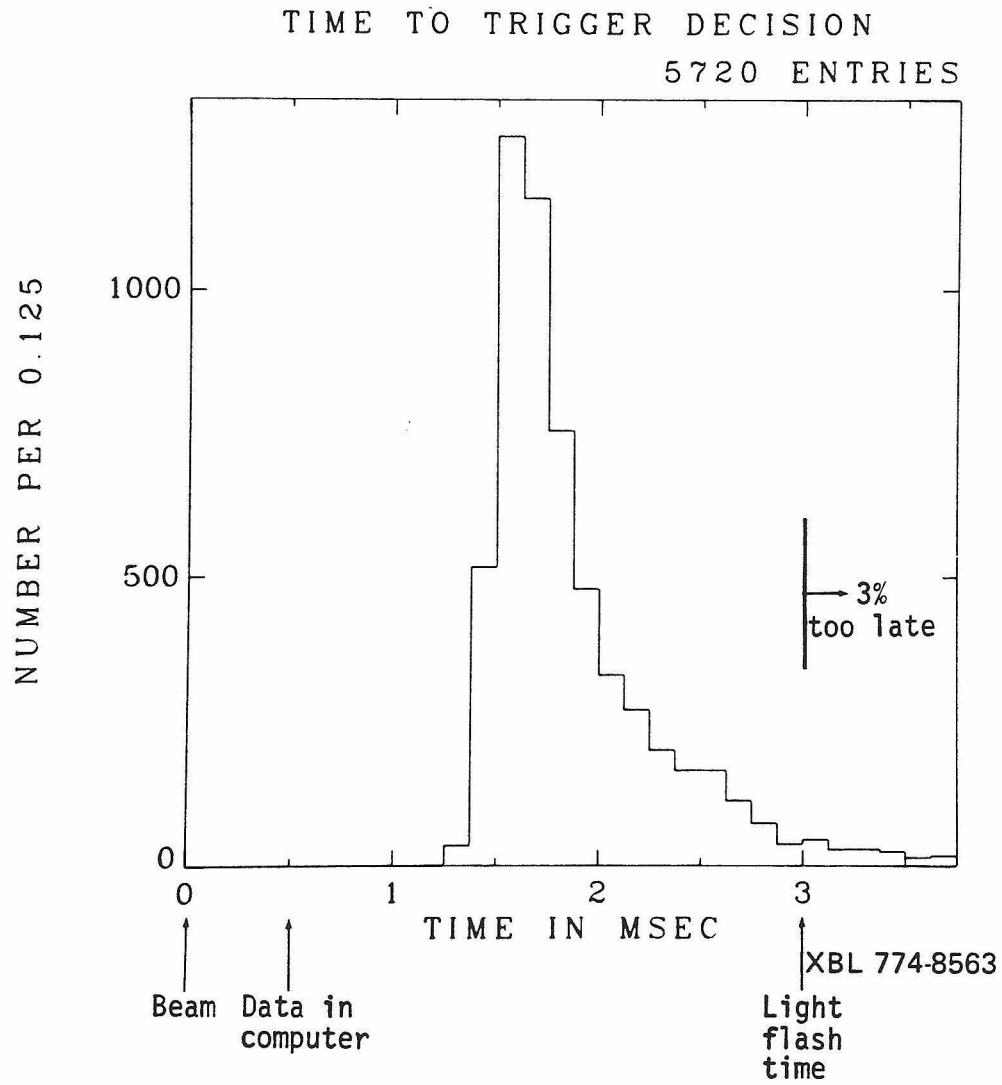


FIG. 10. Distribution of the time required for the trigger program to reach its decision.

TABLE II.D.--Statistics of data collection.

	Number acquired	Beam pulses	As a fraction of SC triggers	BC pictures	BC events
Beam pulses	$5.5 \times 10^6$	---	---	---	---
Spark chamber triggers	$2.5 \times 10^6$	0.45	---	---	---
BC picture triggers	$3.2 \times 10^5$	0.058	0.13	---	---
Pictures lost because of late trigger	$1.0 \times 10^4$	0.002	0.004	0.03	---
BC triggers on events in fiducial volume	$1.1 \times 10^5$	0.020	0.044	0.34	---
BC triggers on elastic scatters	$2.8 \times 10^4$	0.0051	0.011	0.088	0.25
BC triggers on inelastic two prongs	$4.9 \times 10^4$	0.0089	0.020	0.15	0.45
BC triggers on four prongs	$3.5 \times 10^4$	0.0064	0.014	0.11	0.32
BC triggers on $\pi^- p \rightarrow \pi^- \pi^+ \pi^- p$	$1.7 \times 10^4$	0.0031	0.0068	0.053	0.15

### III. PROCESSING

#### 1. Overview

We describe in this chapter the metamorphosis of the data from its original state to a form convenient for study of its physics. For 75% of the film all processing took place at Lawrence Berkeley Laboratory. For the remaining 25% Caltech carried out the scanning and measuring on systems quite different from the LBL apparatus. In this report we will describe only the LBL processing, and we will use only LBL processed data in the analysis of the next chapter.

In Figure 11 we show schematically the major processes and trace the flow of information from one to another. The figure is only illustrative since large segments of the film received treatment which varied in some respect from what is shown. For example some rolls did not undergo filtering, and the measurement of other rolls was exclusively via COBWEB. In the last section of the chapter we discuss one of the tests that we made to verify correct operation of the processes from measurement through fitting.

#### 2. Processing of the Spark Chamber Data

Our raw spark chamber data for an event consisted of groups of spark digitizations associated with each coordinate of each chamber. A computer code which we built and named TORTIS reorganized the digitizations into "track banks." The collection of sparks forming a track bank defined a trajectory which a charged particle could have followed through the spectrometer. TORTIS permitted an arbitrary number of

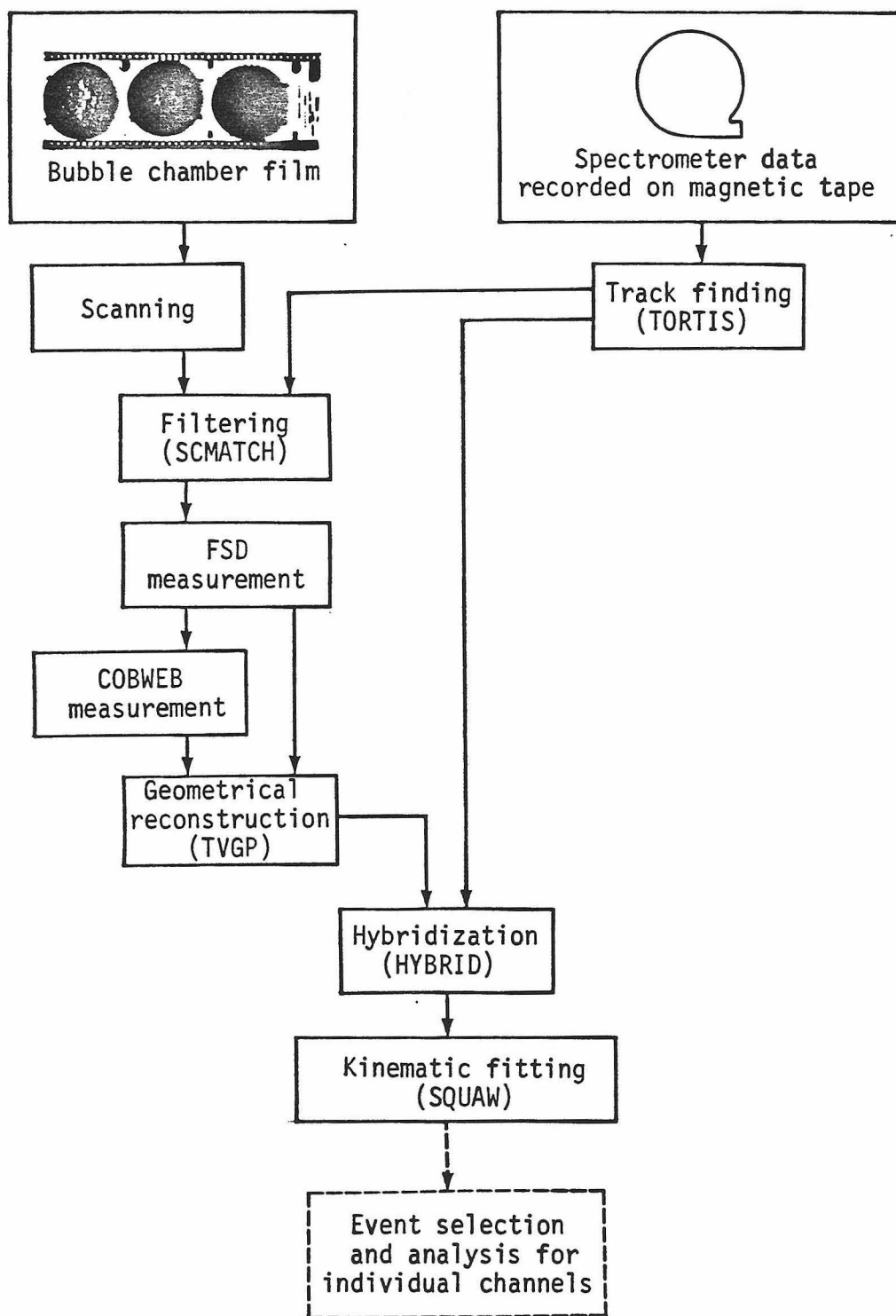


FIG. 11. Preparation of the data for analysis: major processes and the flow of information. FSD and COBWEB designate measuring engines. TORTIS, SCMATCH, TVGP, HYBRID, and SQUAW are computer codes.

track banks for each event, and it permitted each digitization to appear in an arbitrary number of banks. The TORTIS algorithm went roughly as follows. ( $y$  and  $z$  are defined in Figure 8.)

1) Merge the sparks of adjacent chambers into station banks and remove redundant sparks.

2) Find all sets of four  $z$  coordinates, one from each station, for which the lines defined by the station 1,2 pair and the station 3,4 pair intersect at the midplane of the spectrometer magnet. A separation of the lines at the midplane of less than 0.3 cm satisfies this condition.

3) Analogously find sets of four  $y$  coordinates, one from each station, but additionally require that the angle between the lines be less than 2.5 mrad. The tolerance on this angle accommodates the bend in the vertical plane caused by the fringe field of the spectrometer magnet.

4) Pair each set of  $y$  coordinates with each set of  $z$  coordinates. When the UV chambers at station 1 contain digitizations consistent with the  $y,z$  position, form a track bank. In the case that steps 2 and 3 result in just one  $z$  coordinate set and one  $y$  set, form the track bank regardless of the UV chamber output.

The tolerances used in TORTIS were liberal enough that the algorithms did not add significantly to the inefficiency of the spark chambers themselves. Considering only those beam pulses which generated a BC camera trigger, the TORTIS efficiency was at least 95%. The precise value is unimportant because it does not enter in the method used to obtain absolute normalization in Chapter IV. The track banks

created by TORTIS were available to the filter and hybridization processes which we describe in succeeding sections.

### 3. Scanning and Filtering

Bona fide events occurring within the fiducial volume of the bubble chamber (70 cm in length) account for only 35% of the BC camera triggers. The balance are ascribable to events occurring in hydrogen outside the fiducial volume (58 cm, much of which was invisible), to events occurring in the beam entrance and exit windows (equivalent to 18 cm of  $H_2$ ), and to decays of beam particles in the last several meters of beam preceding the station 1 spark chambers. A typical roll of film of 1000 frames, containing  $\approx 350$  bona fide events, contains in addition  $\approx 350$  events within the fiducial volume which are not trigger associated and do not match a track in the spectrometer. Measurement of these interlopers is unproductive, so we devised a scanning process which substantially reduced this burden.

Our scanners worked at scan tables equipped with an image plane digitizing arm electronically interfaced to a magnetic tape drive. When they located an event, they digitized one fiducial and the vertex of the event in one view only. By the touch of a button the scanner recorded the roll and frame numbers, the event type, and the digitizations. We used this procedure to locate all events except those with kinks or V's resulting from the production and decay of strange particles.

The scan output and the TORTIS output were the input to a computer code, SCMATCH. For each event discovered in the scan this

code projected each of the spectrometer tracks back to the  $x$  coordinate of the event's vertex. When the  $y$  coordinate of the vertex was within 1.8 cm of one of the projections, the code flagged the event for measurement. We adopted the generous 1.8 cm tolerance rather than take pains to optimize this process. The output per 1000 frames contained all trigger associated events and  $\approx 90$  interlopers. The 25% extra measurement burden was acceptable.

#### 4. Measuring

We utilized two independent systems for measuring the events. One was a flying spot digitizer, FSD (known in some quarters as a Hough-Powell device, HPD) under the control of an IBM 7094 computer [White et al. 1968]. Its mode of operation was fully and exclusively automatic; it had no provision for operator assistance in the measurement process. We will give no further details of this system.

The second system, called COBWEB [Albrecht et al. 1968], consisted of several film plane digitizing engines, known as Frankensteins, interfaced to an IBM 7044 computer. The control electronics of the Frankensteins made them "semiautomatic." The reticle of the device is an orientable slit. So long as the operator maintains the axis of the slit within  $6^\circ$  of the tangent to a track, the electronics will drive the stage so that the track passes precisely through the center of the reticle. The machine can automatically digitize at intervals along the track while the stage is in motion. Completely manual control of the stage is also available to the operator, and he uses it to bypass

regions of confusion or obstruction of a track. The computer as well as the operator can control stage position and frame advance, and the computer intervenes where possible to speed the measurement process.

The FSD system was the first to process each roll. It produced measurements for about 45% of the events on the measurement list. We then directed the COBWEB system to measure those events (55%) on which the FSD system failed. The output of either system was a magnetic tape record containing up to twenty pairs of film plane digitizations for each view of each track.

#### 5. Geometrical Reconstruction

The input to the process which we call reconstruction is the output of the measuring systems just described. Its function is to produce a five parameter description of each track and the  $5 \times 5$  error matrix for the parameters. Specifically, in the coordinate system of Figure 8, the parameters are the polar and azimuthal angles and the curvature at the beginning of the track, and the polar and azimuthal angles at the end of the track. The computer code which we utilized for reconstruction was TVGP (Three View Geometry Program) [Solmitz et al. 1966]. This code has seen prior use in many experiments and with several different bubble chambers and measurement systems. Its architecture facilitates adaptation to a particular bubble chamber, and we had only to develop the necessary modifications for the SLAC 40" chamber.

Particle trajectories in liquid hydrogen depend on the particle

mass as well as momentum because of energy loss by ionization,  $dE/dx$ . TVGP obligingly allows for a number of different mass interpretations of each track. For negative tracks we obtained only a  $\pi^-$  interpretation, and for positive tracks we obtained the  $\pi^+$  and proton interpretations. We omitted  $K^-$  and  $K^+$  interpretations and other more esoteric possibilities in favor of savings in computer charges.

## 6. Hybridization

We built a computer code, HYBRID, which amalgamated the output of TVGP with the output of TORTIS. It carried out two distinct operations which we will call "matching" and "averaging." The matching process selected from the TORTIS track banks the track which was most compatible with the bubble chamber measurement of the fast forward  $\pi^-$ .<sup>†</sup> The averaging process created a unified description of the forward  $\pi^-$  using the best information from both the spark chambers and the bubble chamber.

In the matching we utilized a nine component  $\chi^2$  statistic, and we give below a brief description of each component.

1) Horizontal distance (along  $z$ , in the bending plane) between the projections at the magnet midplane of the station 1,2 sparks and the station 3,4 sparks.  $FWHM \approx 0.13$  cm.

---

<sup>†</sup>In the case of four prongs we compared the TORTIS track banks only with the negative bubble chamber track of higher momentum. The number of four prong events lost by this selection was negligible.

2) Vertical distance (along  $y$ , transverse to bending plane) between the projections as in 1) above. FWHM  $\approx 0.17$  cm.

3 & 4) Displacement of the spark in the UV chambers from the position consistent with the  $y, z$  measurements at stations 1 and 2. FWHM  $\approx 0.16$  cm.

5) Difference in momentum as measured in the bubble chamber and spectrometer. FWHM  $\approx 1.5$  GeV.

6) Difference in the polar angle (the "dip" angle) at the end of the bubble chamber track. FWHM  $\approx 7.5$  mrad.

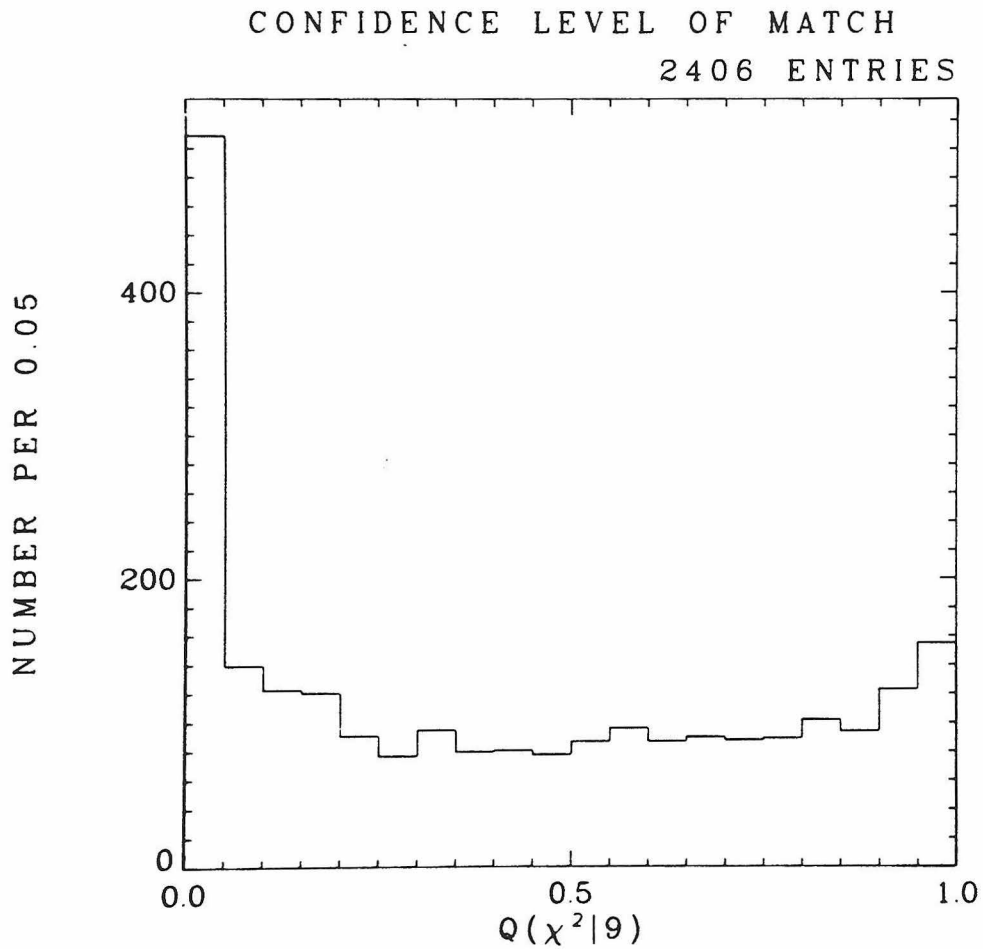
7) Difference in the azimuth angle at the end of the track. FWHM  $\approx 3.5$  mrad.

8) Difference in the  $y$  coordinate at the end of the track. FWHM  $\approx 0.25$  cm.

9) Difference in the  $z$  coordinate at the end of the track. FWHM  $\approx 0.30$  cm.

The first four measure only the quality of the spectrometer portion of the track. The last five measure the differences between the bubble chamber and spectrometer measurements. The TVGP output did not include correlations for the position variables ( $y, z$ ), but all of the correlations that were available were included in the construction of the  $\chi^2$ .

We show in Figure 12 the confidence level distribution for a typical subset of the film. Flaws in our algorithm resulted in a distinctly nonflat distribution, but we considered it flat enough for the purpose at hand. By applying the algorithm to bubble chamber measurements for one frame and spark chamber data for a different frame,



XBL 774-8564

FIG. 12. Distribution, based on ten rolls of film, of the confidence level for the best match of a spark chamber track to the high momentum bubble chamber track. Included are only events with  $\chi^2 < 60$  which corresponds to  $Q(\chi^2|9) > 10^{-9}$ .

we determined the rate of accidental matches. It was only a few tenths percent, and it was not the major contributor to the spike at small confidence level. We presume that the spike results from non-Gaussian errors in various parts of the measurement process. We made our  $\chi^2$  cutoff quite liberal, putting off a more critical selection to a later stage. The upper limit for accepted events was 60, which corresponds to a nominal confidence level of  $10^{-9}$ . We do not know the proportion of good events which failed to match, but we chose to normalize our results by a technique which is insensitive to this loss (see Section IV.4).

For the purpose of kinematic fitting, which we discuss in the next section, we require a unified description of the fast forward  $\pi^-$  which makes best use of the measurements from both bubble chamber and spectrometer. Our algorithm, which we call averaging, actually combines averaging with selective suppression of some information. First we discuss abstractly the mathematics of the algorithm. Suppose that we have available two measurements of a quantity  $x$ ,  $x_a$  and  $x_b$ , and the respective variances  $\sigma_a^2$  and  $\sigma_b^2$ . We define

$$\begin{aligned} w_a &= (\sigma_a^2)^{-1} \\ w_b &= (\sigma_b^2)^{-1} \\ w &= w_a + w_b \end{aligned} \tag{6.1}$$

Then the maximum likelihood best estimate of  $x$  is

$$\bar{x} = w^{-1} (w_a x_a + w_b x_b) \quad (6.2)$$

and its variance is

$$\sigma^2 = w^{-1} . \quad (6.3)$$

We can readily interpret equations (6.1)-(6.3) for a vector valued  $x$ .  $\sigma_a^2$  and  $\sigma_b^2$  are then covariance matrices and the reciprocal operation,  $( )^{-1}$ , becomes matrix inversion. Now suppose that we have some reason to distrust the  $i^{\text{th}}$  component of  $x_a$  and that we therefore wish to impose the condition

$$\partial \bar{x} / \partial (x_a)_i = 0 . \quad (6.4)$$

We do so by replacing  $w_a$  with  $w'_a$  defined as follows.

$$(w'_a)_{jk} = \begin{cases} (w_a)_{jk} & j \neq i, k \neq i \\ 0 & \text{otherwise} \end{cases} \quad (6.5)$$

This definition ensures that  $w = w'_a + w_b$  will be symmetric and positive definite as required for a weight matrix (proof omitted).

Application of the above method requires covariance matrices which refer to a common set of track parameters. Therefore the first step of the averaging procedure was to generate from the TORTIS output a TVGP style parametrization of the forward  $\pi^-$  and the corresponding

covariance matrix. The parameters which we chose to suppress from the average were the spectrometer measurement of azimuth and the bubble chamber measurement of polar angle (dip). We did not use the spectrometer azimuth because our technique for propagating the trajectory through the bubble chamber fringe field was crude and could have introduced bias. The benefit from improving the technique would have been meagre because the bubble chamber measurement of azimuth is quite accurate relative to the spectrometer even for short tracks.

In the case of the polar angle the spectrometer offers the higher precision. What led us to cast out the bubble chamber measurement of polar angle was a failure of the camera which produced variable deformation of the film at the time of exposure. The only symptom was severe skewing in the distribution of the difference of the two measurements of polar angle (not shown). The malady no doubt affected measurements of all tracks, but for low momentum tracks the effect was inconsequential. Only for the beam and the fast forward track did the small perturbation of the polar angle correspond to a sizeable mis-measurement of transverse momentum.

We handled the beam track with the same averaging algorithm that we used with the fast forward. The dispersion of the beam tracks in both momentum and angle was considerably less than the dispersion of the respective measurements. We could therefore obtain a better representation of each beam track by averaging the individual measurement with an "archetype," a pseudotrack with parameters and covariance matrix corresponding to the beam track population. We constructed such an

archetype by combining information from various sources. For example the beam design established the momentum spread, and from samples of 4C events (no neutrals) we could determine the mean polar angle. In the averaging algorithm the parameters which we suppressed were the archetype azimuth angle and the measured polar angle. The azimuth is the parameter for which the archetype is least beneficial. We suppressed it just to spare ourselves the inconvenience of constructing and maintaining an accurate central value. We suppressed the measured polar angle because it was biased on account of the film deformation.

In a formal sense the hybrid momentum (technically, the curvature) of the beam and fast forward tracks was an average. Practically, however, the archetype and spectrometer momenta alone determined the hybrid values because their errors were several times smaller than those of the respective bubble chamber measurements. Accuracy in the difference of the beam and fast forward momenta is critical for obtaining proper fits to the events. On the other hand a discrepancy of a few tenths of a GeV between the archetype momentum and the true central beam momentum could have existed without significant adverse effect. We describe next the steps we took to promote good values for the momentum and other parameters of the beam archetype.

The kinematics of 4C events (no neutral secondaries) makes them especially suitable for monitoring parameters of the hybridization process. We write the constraints of energy-momentum conservation as follows.

$$\begin{aligned}
\Delta E &\equiv E_b + M_p - E_f - E_s = 0 \\
\Delta P_x &\equiv P_{xb} - P_{xf} - P_{xs} = 0 \\
\Delta P_y &\equiv P_{yb} - P_{yf} - P_{ys} = 0 \\
\Delta P_z &\equiv P_{zb} - P_{zf} - P_{zs} = 0
\end{aligned} \tag{6.6}$$

The subscripts  $b$  and  $f$  denote the beam and fast forward tracks, and the subscript  $s$  denotes a summation over the low momentum secondaries. The beam direction is close to the  $x$  axis deviating by up to 50 mrad. The fast forward track also follows the  $x$  axis and usually deviates by less than 50 mrad. We obtain a particularly powerful constraint equation by taking the difference  $\Delta E - \Delta P_x$ ,

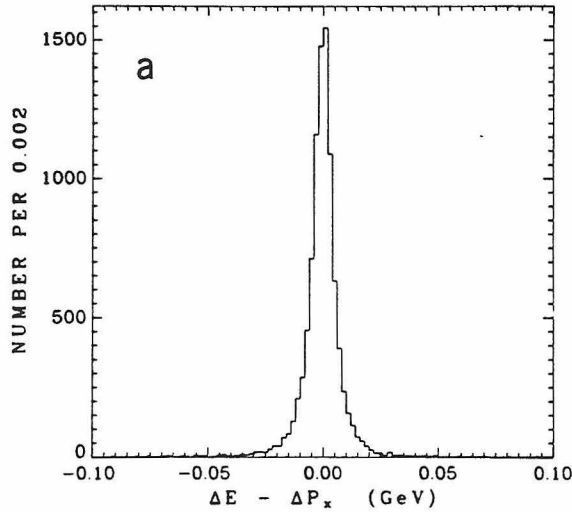
$$(\Delta E - \Delta P_x) \equiv (E_b - P_{xb}) - (E_f - P_{xf}) - (E_s - P_{xs}) + M_p = 0 . \tag{6.7}$$

The terms  $(E_b - P_{xb})$  and  $(E_f - P_{xf})$  are of the order of 10 MeV, and errors as large as 10% in the magnitude of  $P_b$  (or  $P_f$ ) or  $\approx 10$  mrad in its direction perturb  $(\Delta E - \Delta P_x)$  by only a fraction of 10 MeV. We have, therefore, a robust way to identify 4C events. If we combine a cut on  $(\Delta E - \Delta P_x)$  with very loose cuts on  $\Delta P_y$  and  $\Delta P_z$  we can obtain an admirably pure sample without the formality of kinematic fitting.

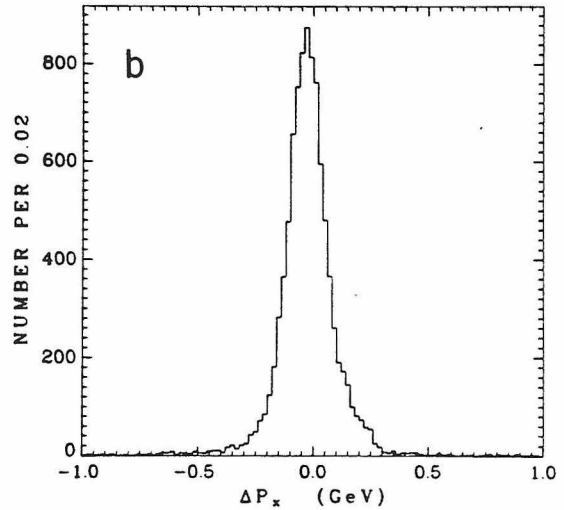
For 4C four prong events  $(\pi^- p \rightarrow \pi^- \pi^- \pi^+ p)$  selected by this technique we may examine the distributions of  $\Delta P_x$ ,  $\Delta P_y$ , and  $\Delta P_z$ . Symmetric distributions with means close to zero indicate well chosen values for the momentum and polar angle of the beam archetype. In

$\pi^b p^t \rightarrow \pi^r \pi^s \pi^+ p$ , 14 GeV/c

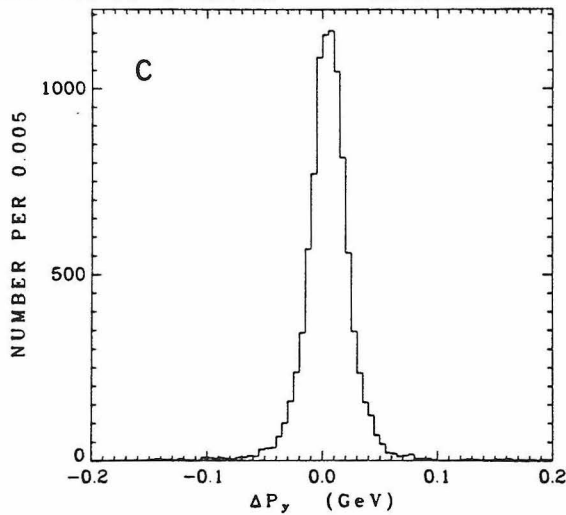
$\langle X \rangle = -.63 \cdot 10^{-3} \sigma = .98 \cdot 10^{-2}$  9320 ENTRIES



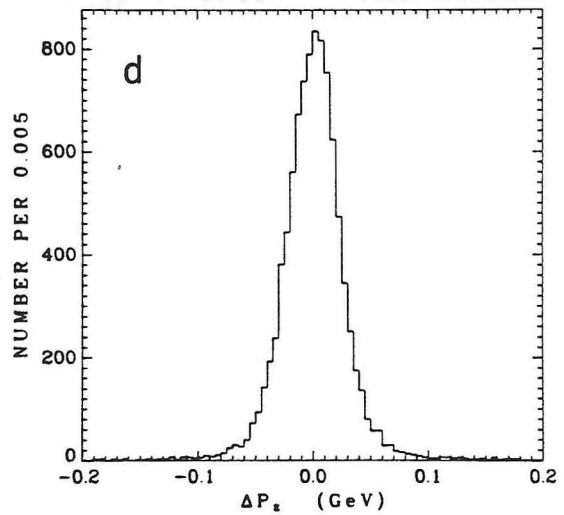
$\langle X \rangle = -.26 \cdot 10^{-1} \sigma = .14$  9301 ENTRIES



$\langle X \rangle = .49 \cdot 10^{-2} \sigma = .22 \cdot 10^{-1}$  9342 ENTRIES



$\langle X \rangle = .34 \cdot 10^{-3} \sigma = .28 \cdot 10^{-1}$  9325 ENTRIES



XBL 772-7591

FIG. 13. Components of the missing energy-momentum vector for 4C four-prong events. a) Difference of the energy and beamlike component of momentum. b) The beamlike component. c,d) The transverse components.  $\hat{z}$  is parallel to the camera axis.

Figure 13 a-d we show these distributions. All are reasonably symmetric and well centered. The analogous distributions for events from each ten rolls of film are similar to the large sample distributions of the figure.

## 7. Kinematic Fitting

A two prong event may ab initio be an example of one of several reactions of which the following are the most probable.

$$\pi^- p \rightarrow \pi^- p \quad (7.1)$$

$$\rightarrow \pi^- \pi^0 p \quad (7.2)$$

$$\rightarrow \pi^- \pi^+ n \quad (7.3)$$

$$\rightarrow \pi^- p (\pi^0)^k \quad k > 1 \quad (7.4)$$

$$\rightarrow \pi^- \pi^+ n (\pi^0)^k \quad k > 0 \quad (7.5)$$

We consider for a moment just reaction (7.2). A complete kinematic description entails twelve parameters which we could choose to be the cartesian components of momentum of the beam and each of the three secondaries. These parameters must satisfy the four constraint equations of energy-momentum conservation. Therefore in the nine dimensional space of the measured parameters reaction (7.2) maps onto an eight dimensional hypersurface. Because of measurement error the point representing an event which is truly an example of reaction (7.2) would lie at a small distance from this hypersurface. The

kinematic fitting process locates that point on the hypersurface which is closest to the measurement point. The covariance matrix serves as metric, and the square of the minimum distance is a  $\chi^2$  statistic for one degree of freedom.

Kinematic fitting is likewise applicable to reactions (7.1) and (7.3), the latter being completely analogous to (7.2). The hypersurface of reaction (7.1) is five dimensional, so fitting yields a  $\chi^2$  with four degrees of freedom. The reactions with multiple neutral secondaries, (7.4) and (7.5), are underconstrained, and only the mass of the neutral system is determinable. The major four-prong channels are in one-to-one correspondence with reactions (7.1)-(7.5) by the addition of a  $\pi^+$  and  $\pi^-$  to each final state. The dimensionalities of the measurement space and the reaction hypersurfaces are greater by six, but the efficacy of the fitting procedure is the same.

The benefit of kinematic fitting is threefold. 1) The postfit parameters exactly conserve energy-momentum. 2) The postfit errors are smaller, sometimes much smaller, than the original measurement errors. 3) The  $\chi^2$  statistics are invaluable for selecting a sample of a particular reaction. We have at our disposal requirements for low  $\chi^2$  in a desired channel and for high  $\chi^2$  in competing channels, and we may combine these as appropriate to obtain a sample of suitable purity.

The computer code which we used for fitting was SQUAW [Dahl et al. 1968] which is a companion code to TVGP. The reactions to which we fitted two-prong events were

$$\pi^- p \rightarrow \pi^- p \quad (7.6)$$

$$\pi^- p \rightarrow \pi^- \pi^0 p \quad (7.7)$$

$$\pi^- p \rightarrow \pi^- \pi^+ n . \quad (7.8)$$

For four-prongs the reactions were

$$\pi^- p \rightarrow \pi^f \pi^s \pi^+ p \quad (7.9)$$

$$\pi^- p \rightarrow \pi^f \pi^s \pi^+ \pi^0 p \quad (7.10)$$

$$\pi^- p \rightarrow \pi^f \pi^s \pi^+ \pi^+ n . \quad (7.11)$$

The superscripts  $f$  and  $s$  identify the fast forward  $\pi^-$  and the low momentum  $\pi^-$ . For the reactions (7.9) and (7.10) SQUAW generates two fits, one for each assignment of masses to the positive tracks.

Kinematic fitting is the last process which we describe in this chapter. In the output of SQUAW we have a description of the data which is suitable for study of the physics of the various reactions. We do best to regard the problem of sample selection as reaction dependent. A global algorithm which assigns each event to exactly one reaction can not achieve the proper balance of event loss and contamination for all reactions simultaneously. For example the  $\chi^2$  criteria used to accept events when selecting a 4C sample should in general be quite different from the criteria used to reject 4C events when selecting a 1C sample. In Chapter IV we discuss sample selection in detail for reaction (7.9).

## 8. Validation

We have just described the complex system of measuring engines and computer programs with which we extracted fitted track parameters from protographs. In this section we give results from one kind of test that this system performed as expected, that its output is trustworthy. In the ideal method for testing a large "black box" we would introduce input for which the correct output is fully predictable on a trial-by-trial basis. The strength of our technique is that its approach to this ideal is the closest feasible. Its weakness is that, falling short, it remains a statistical test, and a necessarily small sample size limits its sensitivity.

Our test utilizes events which produced a neutral strange particle, and, as we noted in Section III.3, we did not scan for such events in the present experiment. The source of our events therefore had to be a companion experiment in the same bubble chamber for which the beam was  $\pi^+$  at 14 GeV/c rather than  $\pi^-$ . For the companion experiment the scan did include strange particle topologies. The reactions of interest are the following.

$$\pi^+ p \rightarrow \pi^+ K^+ \Lambda \quad (8.1)$$

$$\pi^+ p \rightarrow K^+ p \bar{K}^0 \quad (8.2a)$$

$$K^+ p \rightarrow \pi^+ p K^0 \quad (8.2b)$$

$$\pi^+ p \rightarrow \pi^+ \pi^+ \pi^- K^+ \Lambda \quad (8.3)$$

$$\pi^+ p \rightarrow \pi^+ \pi^+ K^- p K^0 \quad (8.4a)$$

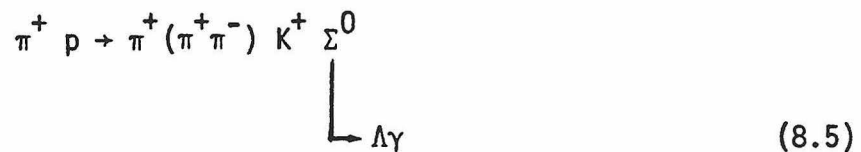
$$\pi^+ p \rightarrow \pi^+ \pi^- K^+ p \bar{K}^0 \quad (8.4b)$$

The events to be treated are those with a  $\pi^+$  or  $K^+$  measured in the spectrometer and a single strange particle decay (a "V") in the bubble chamber. So far as possible the treatment of these events from measurement through kinematic fitting was identical with the treatment of ordinary data.

The strategy is first to identify the events which are examples of reactions (8.1)-(8.4), then to refit these events treating the tracks from the  $\Lambda$  or  $K^0$  decay as emanating from the primary vertex with arbitrary invariant mass. By discarding in addition the information for one of the charged tracks (but not the fast forward) we can simulate a 1C fit. The test of the processing system is to verify that these "hobbled" fits reproduce the mass of the  $\Lambda$  or  $K^0$  within assigned errors.

We deemed an event to be an example of one of the  $\Lambda$  or  $K^0$  reactions if the confidence level for the fit was greater than 0.05 and if the confidence level for alternative 7C fits was less than  $10^{-3}$ . The result of increasing the cutoff for alternative fits from  $10^{-3}$  to  $10^{-2}$  is an insignificant increase in the sample size.

Most events assigned to the  $\Lambda$  reactions by this procedure also have a good fit to the reactions



The reason is that the kinematics permits the lab momentum of a  $\Lambda$  to be parallel to the lab momentum of a parent  $\Sigma^0$ . The lab momentum of the sibling  $\gamma$ , in this case, is usually so low that the measurement errors can easily accommodate it. This inherent ambiguity together with the selection criteria results in contamination of the 7C  $\Lambda$  sample by  $\Sigma^0$  events. The extent of this contamination depends on nature's cross section for the  $\Sigma^0$  reactions, on the momentum distributions of the produced  $\Sigma^0$ 's and on their decay distribution. The available sample size is insufficient to measure these distributions and thus estimate the contamination. We observe, however, that 1) the number of unambiguous  $\Sigma^0$  events is about 20% of the number assigned to  $\Lambda$  channels, and that 2)  $\Sigma^0$  events are usually unambiguous. Regardless of the  $\Sigma^0$  momentum, only in a small proportion of the decay phase space is the  $\gamma$  momentum in the lab so small that an ambiguity is likely to occur. In particular a  $\Sigma^0$  nearly at rest yields a  $\gamma$  of 75 MeV which is rarely concealable by measurement errors. We are therefore confident that  $\Sigma^0$  contamination in the 7C  $\Lambda$  sample is insignificant.

To illustrate our method of analysis we consider the set of hobbled fits for reaction (8.1), in which the  $\pi^-$  daughter of the  $\Lambda$  was treated as unmeasured. For each event we construct the quantity

$$\delta = \frac{M_{\pi^- p} - 1115.6 \text{ MeV}}{\sigma_M} . \quad (8.6)$$

In this expression  $\sigma_M$  is the standard deviation of  $M_{\pi-p}$  as computed by SQUAW using its complete error matrix. If the processing system works correctly, the observed  $\delta$ 's are a sample from a standard normal population. To assess the normalcy of the  $\delta$ 's, we selected the Kuiper statistic [Kuiper 1960]. In Appendix B we give an introductory discussion of this statistic and mention those characteristics which commend its use in the present situation.

We state our results in Tables III.A and III.B which have entries for each of the hobbled fits. In Table III.A we give the sample size and the confidence level for the Kuiper statistic. For the benefit of those who distrust an unfamiliar statistic we give in Table III.B the mean and the  $\sigma$  of the  $\delta$ 's. All of these statistics are dimensionless. The errors quoted in Table III.B are the sampling errors for a standard normal population. An excess of very small Kuiper confidence levels would signal some misbehavior of the processing system. This signal does not occur. The imperfections in the processing are small enough that they are not detectable by this method with 142 events.

We have shown that the actual errors of the measured  $\Lambda$  and  $K^0$  masses are consistent with the assigned errors for several kinds of fits. To complement this result we indicate the size of the assigned errors in Table III.C. We give the root-mean-square  $\sigma_M$  both in MeV and as a fraction of the kinetic energy released in the decay. The upper entry is

$$\eta = \left| \frac{1}{N} \sum_{\text{events}} \sigma_M^2 \right|^{1/2} \quad (8.7)$$

and the lower entry is  $\eta/Q_{\Lambda,K}$  with  $Q_{\Lambda} = 37.8$  MeV and  $Q_K = 218.6$  MeV. We also calculate the error of  $\eta$  from the sample variance of  $\sigma_M^2$ . (Some of the samples are so small, however, that a Gaussian interpretation of the error is unjustified.) The table shows as expected that the resolution is quite good for 4C fits and that it deteriorates appreciably as we discard additional information. The mass resolution for these fits of strange particle events does not bear directly on the mass resolution for other channels. Having established the veracity of SQUAW's errors, however, we can compute resolution ( $\eta$ ) in other channels in this same straightforward way.

TABLE III.A.--Validation statistics.

Upper entry is the sample size. Lower entry is the confidence level for the Kuiper statistic. Statistics in the two-prong column are for reaction (8.1) or (8.2), and those in the four-prong column are for reaction (8.3) or (8.4). The row labels distinguish the  $\Lambda$  reactions from the  $K^0$  reactions and indicate which track measurements, if any, were discarded.

	Two-prongs		Four-prongs		Combined 2 & 4-prongs	
$\Lambda$ 4C	90	0.81	26	0.33	116	0.43
$\Lambda$ p missing	90	0.40	26	0.79	116	0.20
$\Lambda$ $\pi^-$ missing	90	0.47	26	0.68	116	0.31
$\Lambda$ $\pi^+$ or $K^+$ missing	90	0.69	---	---	---	---
$K^0$ 4C	11	0.61	15	0.24	26	0.47
$K^0$ p missing	11	0.56	15	0.22	26	0.17
$K^0$ $\pi^-$ missing	11	0.70	15	0.10	26	0.12
$K^0$ $\pi^+$ missing	11	0.92	15	0.54	26	0.73

TABLE III.B.--More validation statistics.

Upper entry is the mean, and lower entry is the standard deviation of the  $\delta$  distributions. The errors are the sampling errors for a standard normal population.

	Two-prongs	Four-prongs	Combined 2 & 4-prongs
$\Lambda$	0.14±0.11	0.14±0.20	0.14±0.09
4C	0.95±0.07	1.03±0.14	0.97±0.07
$\Lambda$	0.05±0.11	-0.01±0.20	0.04±0.09
p missing	0.97±0.07	0.85±0.14	0.94±0.07
$\Lambda$	-0.09±0.11	0.09±0.20	-0.05±0.09
$\pi^-$ missing	1.00±0.07	0.88±0.14	0.98±0.07
$\Lambda$	0.04±0.11	---	---
$\pi^+$ or $K^+$ missing	0.93±0.07	---	---
$K^0$	0.15±0.30	0.20±0.26	0.18±0.20
4C	0.96±0.22	0.89±0.19	0.92±0.14
$K^0$	0.06±0.30	0.29±0.26	0.20±0.20
p missing	0.90±0.22	0.84±0.19	0.87±0.14
$K^0$	0.42±0.30	0.32±0.26	0.36±0.20
$\pi^-$ missing	0.94±0.22	0.71±0.19	0.82±0.14
$K^0$	-0.28±0.30	-0.09±0.26	-0.17±0.20
$\pi^+$ missing	1.08±0.22	0.82±0.19	0.95±0.14

TABLE III.C.--Mass resolution for the hobbled fits.

Upper entry is the root-mean-square of the strange particle mass error assigned by SQUAW. Units are MeV. The lower entry is the r.m.s. error as a fraction of the kinetic energy released in the decay.

	Two-prongs	Four-prongs	Combined 2 & 4-prongs
$\Lambda$	$1.7 \pm 0.1$	$1.6 \pm 0.2$	$1.7 \pm 0.1$
4C	0.045	0.042	0.045
$\Lambda$	$4.2 \pm 0.7$	$2.7 \pm 0.4$	$3.9 \pm 0.6$
p missing	0.11	0.071	0.10
$\Lambda$	$15 \pm 1$	$13 \pm 1$	$14 \pm 1$
$\pi^-$ missing	0.40	0.34	0.37
$\Lambda$	$2.9 \pm 0.5$	---	---
$\pi^+$ or $K^+$ missing	0.076	---	---
$K^0$	$4.8 \pm 0.6$	$7.1 \pm 1.3$	$6.2 \pm 0.9$
4C	0.022	0.032	0.028
$K^0$	$5.4 \pm 0.7$	$22 \pm 9$	$17 \pm 7$
p missing	0.023	0.10	0.077
$K^0$	$15 \pm 1$	$35 \pm 6$	$28 \pm 5$
$\pi^-$ missing	0.069	0.16	0.13
$K^0$	$14 \pm 1$	$15 \pm 1$	$15 \pm 1$
$\pi^+$ missing	0.064	0.069	0.069

## IV. ANALYSES

## 1. Preamble

In this chapter we undertake to present and interpret the data on the final state  $\pi^-\pi^-\pi^+p$ . We will make no attempt at a comprehensive analysis. On the one hand we note that model dependent approaches to our reaction are fraught with serious theoretical uncertainties. On the other, truly model independent approaches would require between fifty and one thousand times more data than we have at hand and some polarization measurements in addition. For example one of the original intents of this experiment was to determine selection rules for nucleon resonances producible in a diffractive collision. The partial wave analysis required to address this issue in the four-body final state would suffer excessively if not from theoretical biases then from insufficient data.

Instead we will extract from the diverse theoretical schemes a few properties which, with available data, are susceptible to quantitative statistical test. Specifically we will examine the hypothesis of helicity conservation for the s-channel and for the t-channel reference frames. On finding t-channel helicity conservation to be the better approximation we will test for simultaneous validity of the Gribov-Morrison rule on permissible spin-parities.

Some of the ideas included in our program have lost currency if not respectability since they were proposed several years ago. Some other ideas, though potentially of great interest, we have abandoned to our successors. Nonetheless, we believe that the application of simple

and rigorous methods to our selected topics contributes to understanding of the physics underlying this data.

## 2. Estimation and Display of Densities

The most common of the modes which we will use to summarize data will be a graphical estimate of a univariate density. We will sometimes use just a histogram, but often we will use a  $k$ -th nearest neighbor estimator [Friedman 1974]. As the latter is not in common use for data of high energy physics, we offer in this section a brief explanation.

As an example we refer ahead to Figure 14b. The somewhat jagged curve is the  $k$ -NN estimate. If  $d(x)$  is the estimate at  $x$  and if  $k-1$  data points are closer to  $x$  than  $x_j$ , then

$$d(x) \propto |x - x_j|^{-1} \quad (2.1)$$

The magnitude of  $k$  controls the tradeoff between bias (underestimation at peaks, overestimation at dips) and smoothing (suppression of statistical fluctuations) in analogy with the bin width of a histogram. Unlike the histogram, however, the  $k$ -NN estimator is a continuous function of the independent variable. In most cases, to choose  $k$  we generated the display using several widely spaced values. We easily judged most structures which appeared either to be statistical fluctuations or to reflect variations of the parent population. A few structures we judged ambiguous in this regard. For presentation we selected the largest  $k$  which still preserved ambiguous structures. The

subjectivity of this procedure is evident, but we point out that all common density estimation techniques involve analogous subjective decisions.

The relative statistical error of the  $k$ -NN estimate is a constant,  $1/\sqrt{k}$ , and therefore if error bars are omitted from a display, they are easy to visualize. Traditionally error bars serve as a yardstick by which to judge informally whether some alternative to the estimate is actually consistent with the data. For this purpose independent errors are most convenient, whereas for a  $k$ -NN estimate the errors of nearby points are heavily correlated. Therefore we have chosen to indicate the statistical precision of the data with a coarsely binned histogram superposed on the  $k$ -NN estimate. The two estimates, of course, will not be identical even at the center of the histogram bins. They will differ both because they incur different amounts of bias and because of statistical fluctuations.

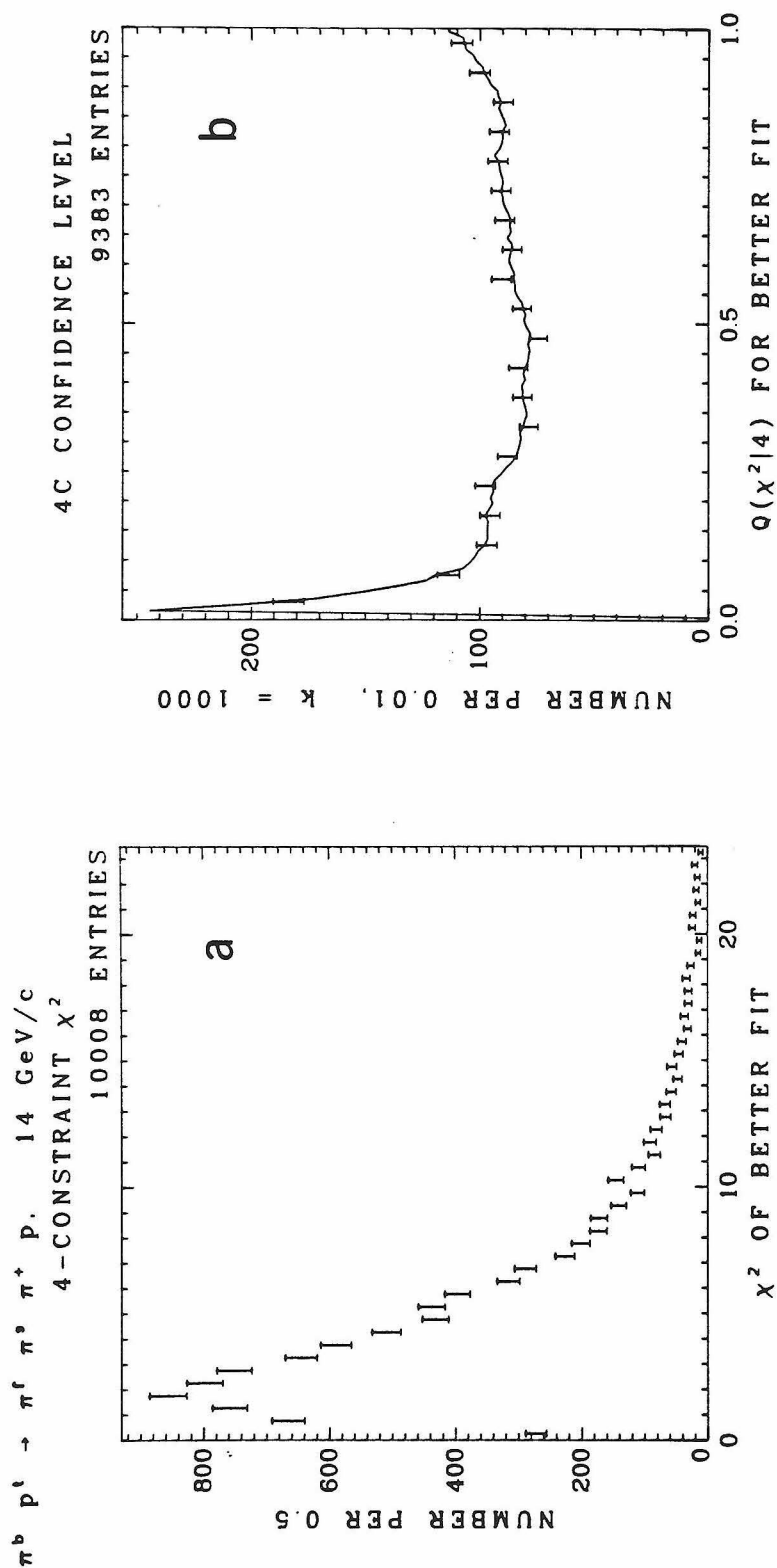
### 3. Event Selection

The overall reaction which we will study is



$\pi^b$ ,  $\pi^f$ , and  $\pi^s$  are all negative pions. The symbol  $\pi^f$  denotes the one which was detected in the forward spectrometer.

We fit each event twice with this hypothesis, once for each assignment of masses to the positive tracks. When the  $\chi^2$  of the better fit was less than 13.3 (corresponding to a confidence level of 0.01), we



XBL 774-8349

FIG. 14. a) Distribution of  $\chi^2$  for the fit to the reaction  $\pi^b p^i \rightarrow \pi^f \pi^s \pi^+ p$ . b) The corresponding confidence level distribution for events with confidence level greater than 0.01 ( $\chi^2 < 13.3$ ).

accepted for further analysis the corresponding interpretation of the event. Track density information (ionization) from this exposure was of poor quality. Its use could have reduced the contamination but to an indeterminable extent. Since the contamination level is in any case quite low as we will demonstrate, we elected not to consider track density in the event selection. In Figure 14a we histogram the  $\chi^2$  of the better fit to reaction (3.1) out to  $\chi^2$  of 23.5, and in Figure 14b we show a  $k^{\text{th}}$  nearest neighbor density estimate of the confidence level distribution down to the cutoff of 0.01.

Above 0.1 Figure 14b comes gratifyingly close to the ideal of a uniform distribution demonstrating that the fitting and event selection procedures are at least sensible. We attribute the substantial rise below 0.1 to a combination of misidentified events and non-Gaussian sources of error. The misidentified events concern us most, so we proceed to a discussion of the nature and extent of our contamination.

The reactions which merit discussion as plausible contaminants in the data sample are the following.

$$\pi^b p \rightarrow \pi^f \pi^s \pi^+ p (\pi^0)^j \quad j \geq 1 \quad (3.2)$$

$$\pi^b p \rightarrow \pi^f \pi^s \pi^+ \pi^+ n (\pi^0)^j \quad j > 0 \quad (3.3)$$

$$\pi^b p \rightarrow \pi^f K^- K^+ p \quad (3.4a)$$

$$\pi^b p \rightarrow K^f \pi^- K^+ p \quad (3.4b)$$

$$K^- p \rightarrow \pi^f K^- \pi^+ p \quad (3.5a)$$

$$K^- p \rightarrow K^f \pi^- \pi^+ p \quad (3.5b)$$

$$\pi^b p \rightarrow \pi^f \pi^s (\pi^+ \text{ identified as } p) (p \text{ identified as } \pi^+) \quad (3.6)$$

In reactions (3.4a) and (3.5a) the particle detected in the forward spectrometer is a  $\pi^-$  whereas in reactions (3.4b) and (3.5b) it is a  $K^-$ . We will consider each of these possibilities in turn, and we will conclude that the sum of all contributions is between 2% and 8% and is probably closer to 2%. For reaction (3.6) we are able to estimate the fraction of the data sample which it generates. For the others an upper limit is the best information we can develop, and these upper limits may grossly exceed the actual contamination. In Table IV.A we summarize what we know about each reaction.

In reaction (3.2) only if the system of  $\pi^0$ 's is at rest in the lab frame can this type of event exactly satisfy the momentum constraints of reaction (3.1). It can exactly satisfy the energy constraint as well, but only if with inverted mass assignment the energy computed for the positive tracks equals the true energy of the positives and neutrals combined. Especially with the spectrometer determination for the forward  $\pi^-$ , our measuring precision makes these conditions exceedingly stringent. For the reaction (3.3) final state no configuration can exactly satisfy the energy constraint. Consequently this reaction has even less potential to contaminate than reaction (3.2).

We have computed an upper limit for the contamination from (3.2) and (3.3) based on conservative assumptions about the distribution in  $\chi^2$  of events from each source. First we assumed that these two channels generate all of the events with  $20.0 < \chi^2 < 23.5$ . Second for the probability that a contamination event has a  $\chi^2 < \xi$  (i.e.  $\chi^2$  of the reaction (3.1) fit) we assumed

$$P(\chi^2 < \xi) \propto \xi^{3/2} \quad (3.7)$$

TABLE IV.A.--The level of contamination of reaction (3.1) from reactions (3.2) - (3.6).

Reaction	Estimate	Upper Limit <sup>†</sup>
3.2	---	3%
3.3		
3.4a	<< 2%	2%
3.4b		
3.5a	<< 2%	2%
3.5b	(benign)	
3.6	1.5%	--

<sup>†</sup>The upper limit may grossly exceed the actual value.

The exponent is one half the difference of the number of degrees of freedom of the 4C reaction (3.1) and the 1C reaction  $\pi^- p \rightarrow \pi^- \pi^- \pi^+ p \pi^0$ . The lower the exponent the higher would be the upper limit, and in Appendix C we state why our choice is conservatively low. Our upper limit comes from evaluating the form (3.7) at  $\xi = 13.3$  using the normalization based on the interval 20.0 to 23.5. The result is 3%.

In our opinion most events with  $20.0 < \chi^2 < 23.5$  actually represent bad measurements of reaction (3.1). If so, the true level of 1C and 0C contamination is considerably less than 3%.

The momentum constraints are ineffective in the case of reactions (3.4) and (3.5). Except for reaction (3.5b) other factors combine to suppress these events to a negligible level. Prior to kinematic fitting, the ratio of reaction (3.4) to reaction (3.1) is of the order of 2%. This estimate matches the proportion of all events which exhibit  $K^0$  or  $\Lambda$  decays. The prefit proportion of reaction (3.5) is also about 2% corresponding to the ratio of incident  $K^-$  to  $\pi^-$  as measured in a beam survey at SLAC [Boyarski et al, 1968].

In the analyses which we pursue in later sections we will restrict attention to events with  $\pi^- \pi^+ p$  mass less than 2.6 GeV, about 75% of the 4C fits. We next argue that most events of reactions (3.4) and (3.5a) do not survive both this mass cut and the kinematic fitting. The dominant processes which contribute to reaction (3.4a) are diffractive dissociation of the incident  $\pi^-$  to  $\pi^- K^+ K^-$  and diffractive dissociation of the target  $p$  to  $pK^+ K^-$ . In the former case the mass of the  $pK^+ K^-$  system will usually be greater than 2.6 GeV even when the  $K$ 's are treated as  $\pi$ 's. In the latter case the lab momentum of at least one of the  $K$ 's will usually be low enough that the fitting procedure rejects the event. Reaction (3.4b) is like (3.4a) except that target dissociation is not a possibility. For reaction (3.5a) the dominant process is diffractive dissociation of the incident  $K^-$  which, as with  $\pi^-$  incident, usually produces a high mass  $K^- \pi^+ p$

system. These arguments convince us that the contamination from reactions (3.4) and (3.5a) is well below the upper limit of 4%, though we have not studied the matter enough to say quantitatively how much below.

Kinematic fitting has no power at all against reaction (3.5b). The major contributory processes are diffractive dissociation of the target proton, dissociation of the incident  $K^-$ , and  $\pi$  exchange which we illustrate in Figure 15.

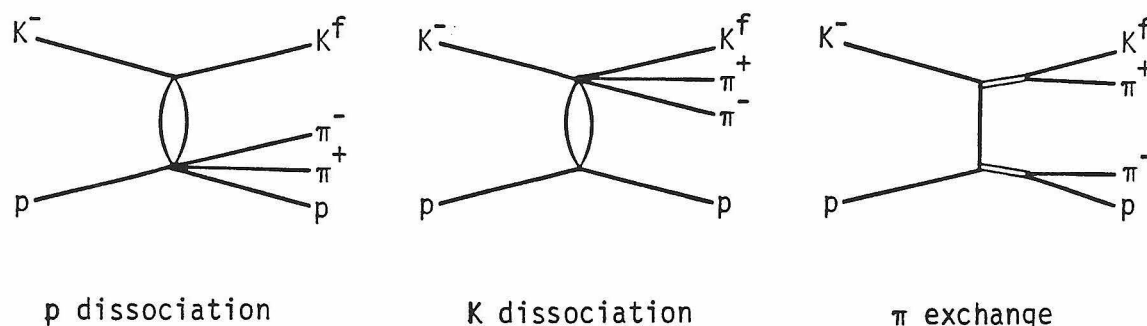


FIG. 15. Diagrams contributing to reaction (3.5b).

All three processes are similar in their grosser characteristics to the analogous  $\pi$  induced processes. The mass cuts we make in later sections to isolate the target dissociation component will work as well for either identity of the projectile. Comparison of our mass spectra with spectra acquired in predominantly  $K^-$  beams [Boesebeck et al. 1971] suggests that target dissociation is similar even in fine detail whether

$\pi$  induced or  $K$  induced. This sort of contamination would be benign even at levels higher than 2%.

Reaction (3.6) is our last and quite likely our most serious source of misidentified events. When the momenta of the positive tracks have nearly the same magnitude in the laboratory frame, the energy constraint loses its power to discriminate between the correct assignment of masses and the inverse assignment. To estimate the proportion of misassignments we have devised a purely statistical technique which we describe in Appendix D. When applied to our uncut sample this technique indicates a 1% rate of misassignment, and for the subsample with  $\pi^+$  mass near the  $\Delta^{++}$  the estimate is 1.5%.

From the foregoing discussion we conclude with some confidence that statistical fluctuations will overshadow contamination effects in any analysis of this data ( $\approx 10^4$  events).

The cut on  $\chi^2$  at 13.3 excludes some number of bona fide events of reaction (3.1). If all measurement errors were Gaussian, the proportion would be 1.0%. The multiple Coulomb scattering distribution, however, is heavy tailed, and we suspect that other processes affecting the measurements are also heavy tailed. In order to place an upper limit on the event loss engendered by the  $\chi^2$  cut we have approximated the confidence level distribution, Figure 14b, by the form

$$N(x) = 9000 [1 + (1/18)\exp(-66x)] \quad (3.8)$$

This expression reasonably matches the shape of the data on the interval

$0.01 < x < 1.0$  . The integral of  $N(x)$  from zero to  $x = 0.01$  amounts to 4% of the accepted sample. This figure may overestimate the loss because some of the rise at small  $x$  may result from contamination rather than non-Gaussian errors. The chief reason for discussing the event loss is its potential effect on the absolute normalization. We will see in the next section, however, that the uncertainty in normalization greatly exceeds 4%. Thus the event loss turns out to have little significance.

In addition to  $\chi^2$  selection we imposed cuts on the measured parameters of the beam track. The objective was to suppress events in which the beam had suffered an unseen small angle elastic scatter. Specifically we discarded an event unless a) the  $z$  of the vertex was within 1.4 cm of the mean, b) the beam track direction was within 4 mrad of its nominal azimuth, and c) within 30 mrad of its nominal polar angle. These cuts reduced the sample by 1%.

Only events with successful first measurements were candidates for inclusion in the present sample. These represent about 75% of the completed Berkeley processing and about 60% of the entire exposure (that is including the Caltech processed film). The grand total of events which met our  $\chi^2$  and other criteria was 9378. Our considered opinion is that biases in this sample are not large enough to affect seriously the analyses which we will pursue. Since we have not proved this point, however, we designate our presentation as preliminary and so acknowledge that results from the complete sample might differ some from results in this report.

#### 4. Normalization

The natural technique for determination of incident flux in a traditional bubble chamber experiment is to count beam tracks at the upstream end of the fiducial volume. In this experiment we introduced dead time on those 40% of the pulses when we triggered the spark chambers, and we photographed a selected 6%. A count of beam tracks is biased and does not fairly measure the average flux. Convincing methods of accounting for the dead time and the bias in combination have eluded us. The traditional flux measurement technique of a counter experiment was also available to us. For each beam pulse we tallied counts from scintillation detectors located upstream of the bubble chamber. Unfortunately our study of the output of these detectors turned up some inconsistencies in their behavior which cast doubt on their reliability.

Ultimately we used the cross section for elastic scattering as previously measured at Brookhaven to establish our normalization. On a 2.5% subsample of our beam pulses we photographed elastic as well as inelastic events. For elastics in the momentum transfer interval  $0.05 < -t < 0.30 \text{ GeV}^2$  we summed the reciprocal geometrical detection efficiency to obtain an apparatus independent estimate of the number of events,  $\left( \sum_{\text{elas}} 1/e_i \right)$ . For the four prongs in this subsample we counted the number,  $N_{4\text{pr}}$ , with recoil mass less than 2.6 GeV. To obtain the cross section corresponding to the elastics,  $\sigma_{e1}$ , we computed the best fit of a simple exponential form to the data of Foley et al. [1969], and we integrated this fit over the pertinent range of  $t$ . Our result from this calibration is the cross section to produce and detect a four prong

(recoil mass <2.6 GeV),

$$\sigma_{4pr} \equiv \frac{\epsilon_{e1} N_{4pr}}{\epsilon_{4pr} \left( \sum_{e1as} \frac{1}{e_i} \right)} \sigma_{e1} . \quad (4.1)$$

$\epsilon_{e1}$  and  $\epsilon_{4pr}$  are the probabilities that elastic scatters and four prongs respectively are discovered in the calibration scan and survive all further processing. The small  $|t|$  cut on elastic scatters at  $0.05 \text{ GeV}^2$  ensures that the range of the proton is at least 4 cm, and protons of this length are quite easy to see at a scan table. This precaution removes the grossest disparity between  $\epsilon_{e1}$  and  $\epsilon_{4pr}$ . Supposing them equal we obtain

$$\sigma_{4pr} = 292 \text{ } \mu\text{b} . \quad (4.2)$$

The statistical error of  $\epsilon_{4pr}$  is about 5% and is attributable dominantly to fluctuation of  $N_{4pr}$ . More serious systematic uncertainties arise from the normalization of the Brookhaven experiment and from uncontrolled scanning/processing efficiencies of the calibration film. Because we scanned this film only once and have not remeasured first pass failures, our supposition that  $\epsilon_{e1} = \epsilon_{4pr}$  is unsubstantiated. Our best understanding of these efficiencies comes from general experience with the scanning and processing systems. On this basis only we regard as unlikely that  $\epsilon_{e1}/\epsilon_{4pr}$  is less than 0.9 or exceeds 1.1. Allowing for all the uncertainties, our opinion is that the true value of  $\sigma_{4pr}$  is within 15% of the value given in equation (4.2) but no

quantitative defense of this assertion is available.

The number of four prongs corresponding to our reaction (3.1) event sample was  $1.40 \times 10^4$ . We have calculated the physical cross section for a subsample,  $Z$ , according to the relation

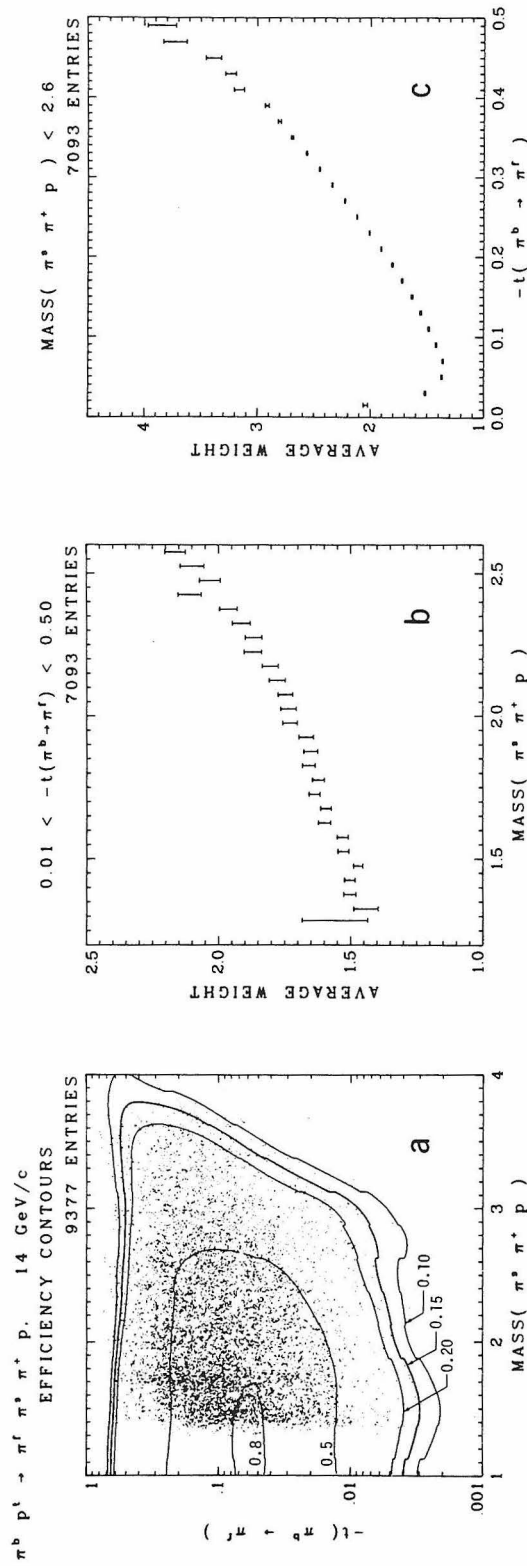
$$\begin{aligned} \sigma_Z &= \frac{1.04}{1.40 \times 10^4} \sigma_{4pr} \cdot \sum_Z \frac{1}{e_i} \\ &= 0.0217 \text{ } \mu\text{b} \sum_Z \frac{1}{e_i} \end{aligned} \quad (4.3)$$

where  $e_i$  is the geometrical detection efficiency for event  $i$ . The factor 1.04 corrects for the  $\chi^2$  truncation loss.

## 5. Acceptance and Weighting

Many events of reaction (3.1) went unobserved because the  $\pi^f$  trajectory missed one of the apertures of the forward spectrometer. We explain here how in our analyses we account for the unobserved events.

A set of parameters sufficient for the description of the  $\pi^f$  trajectory are the beam direction, the vertex coordinates, the azimuth of the  $\pi^f$  about the beam direction, and the kinematic variables  $M(\pi^s \pi^+ p)$  and  $t(\pi^b \rightarrow \pi^f)$ . We consider a function of these eight parameters which equals one when the trajectory passes through all apertures and otherwise equals zero. When we average this function over all parameters except  $M$  and  $t$ , we obtain the detection probability as a function of  $M$  and  $t$  only which we call the acceptance function. The  $M, t$  dependence of this function is indeed severe. It



XBL 774-8359

FIG. 16. a) Contours of the acceptance function in the  $M, t$  plane superposed on a scattergram of the data. b) Average over the data of the reciprocal acceptance in bins of  $M(\pi^s \pi^+ p)$ . c) Like b) but in bins of  $t(\pi^b \rightarrow \pi^r)$ . The vertical bar associated with each average weight indicates the one sigma points of the distribution of the mean.

falls to zero for  $|t| \ll 0.01$  because of the regions of the spark chambers made insensitive to unscattered beam tracks. It becomes small when  $|t| \approx 0.6$  in large measure because of the spectrometer magnet aperture. At higher values of  $M$ , the  $\pi^+$  momentum is lower, and the bend angles in the bubble chamber and spectrometer magnetic fields are larger. Multiple apertures then act in concert to depress acceptance.

To obtain an estimate of the acceptance function we randomly sampled the beam, vertex, and azimuth parameters at each node of a mesh in the  $M, t$  plane. The computer determined whether each trajectory passed through all apertures and tallied successes and failures at each node. We extended the function thus calculated on the mesh to the  $M, t$  plane by Lagrangian interpolation. In Figure 16a we indicate by a few contours the general behavior of the acceptance function. At its maximum the value is about 0.82.

We have removed the effects of the apparatus from density estimates by weighting each event by the reciprocal of the acceptance. We display the average weight as a function of  $M$  in Figure 16b and as a function of  $t$  in Figure 16c. The impact of weighting on distributions of other variables is different, probably milder, than for  $M$  and  $t$  themselves. In some cases we have determined or assumed that a distribution is sufficiently independent of both  $M$  and  $t$  that weighting is unnecessary, and we dispense with it to gain statistical precision and simplicity. Where we have used weights we specify the unit of the ordinate as microbarns per GeV or  $\text{GeV}^2$ . Where we have not used them the units are simply events per indicated division of the abscissa. In the case of  $k$ -th nearest neighbor density estimates,  $k$  refers always to a number of

events without regard to their weights. We compute a weighted k-NN density as the product of the unweighted density and the local average weight.

## 6. Survey of the $N^*$ Mass Spectra

Although the design objective of our experiment was to focus on the subclass of events having the character of nucleon diffraction, about half of reaction (3.1) events correspond to production of  $A$  enhancements in the  $\pi^f \pi^S \pi^+$  system and to  $\rho^0$  and  $f$  enhancements in the  $\pi^f \pi^+$  combination. In Figure 17a we show a scattergram of  $M(\pi^S \pi^+ p)$  vs  $M(\pi^f \pi^S \pi^+)$  and in Figure 17b a weighted histogram of  $M(\pi^f \pi^S \pi^+)$  for events with  $M(N^*) \equiv M(\pi^S \pi^+ p) < 2.6$  GeV. The  $A$  enhancements, prominent in the scattergram, are associated dominantly with high  $N^*$  masses. (We will often refer to the  $\pi^S \pi^+ p$  system as the  $N^*$  without regard to its resonance characteristics.) After the 2.6 GeV mass cut the  $A$ 's contribute about 6% to the cross section. In Figures 18a and 18b we show the analogous scattergram and histogram with  $M(\pi^f \pi^+)$  on the abscissa. These figures show that, unlike the  $3\pi$  enhancements, the  $\rho^0$  and  $f$  heavily overlap the low mass  $N^*$  system.

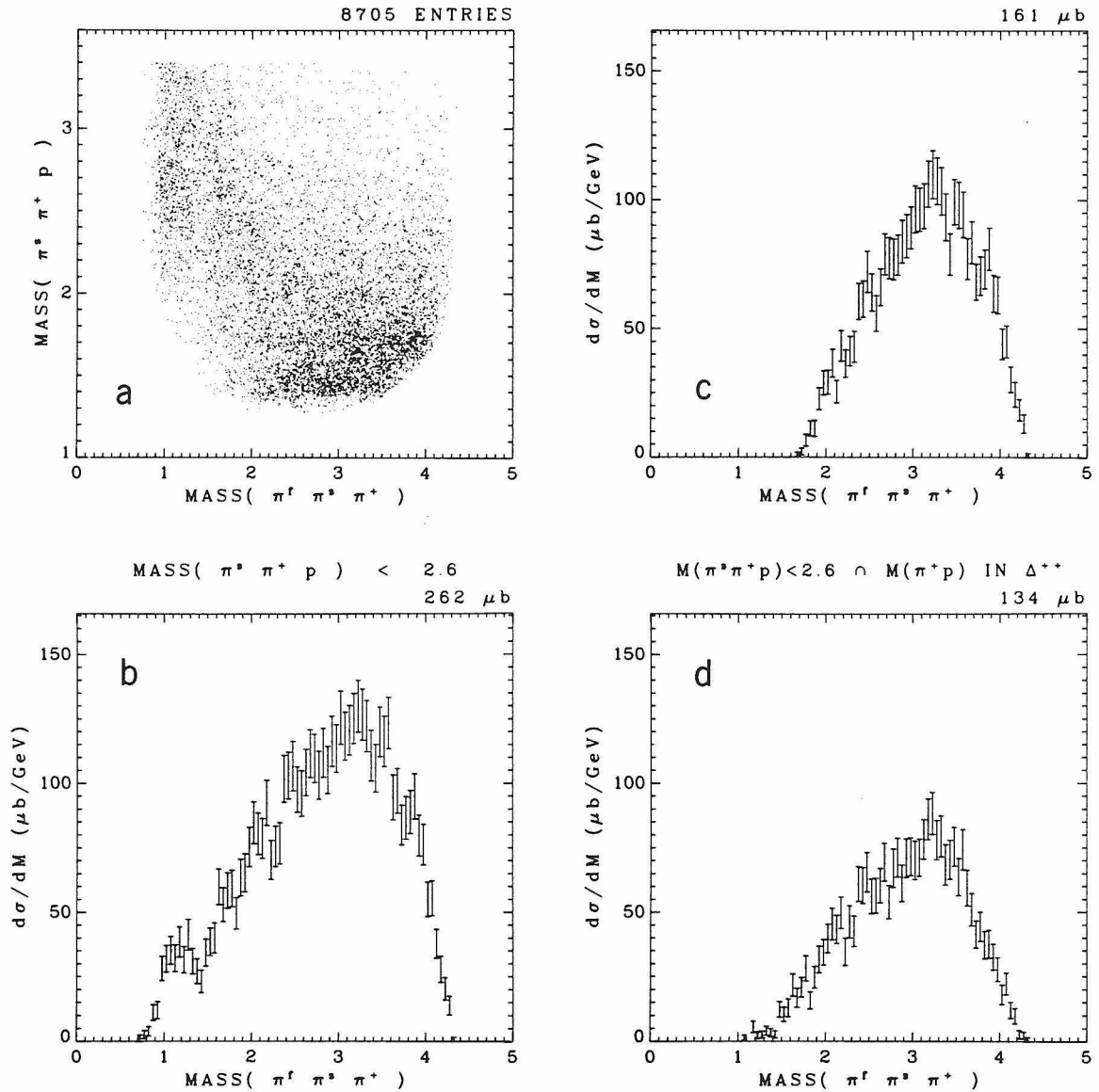
For surveying the  $N^*$  mass spectra we simply excise the  $\rho^0$  and  $f$  signals. Our three cuts will be

$$0.01 < -t(\pi^b \rightarrow \pi^f) < 0.5 \text{ GeV}^2 \quad (6.1)$$

$$M(\pi^S \pi^+ p) < 2.6 \text{ GeV} \quad (6.2)$$

$$M(\pi^f \pi^+) > 1.45 \text{ GeV} \quad (6.3)$$

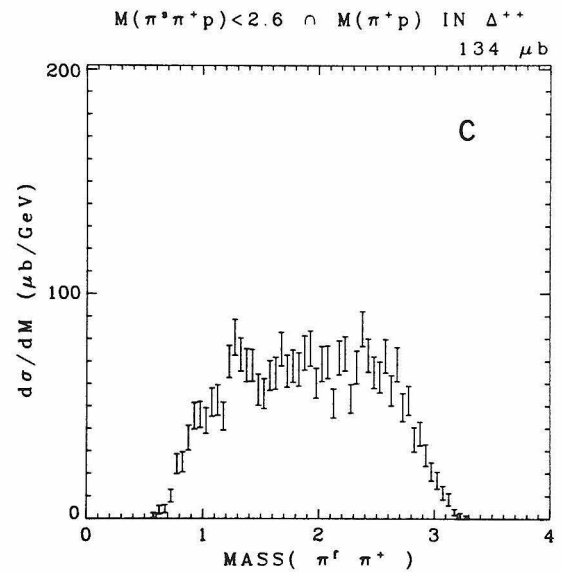
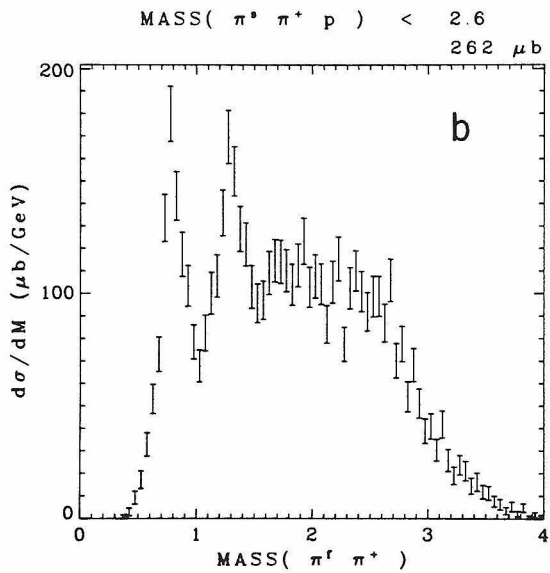
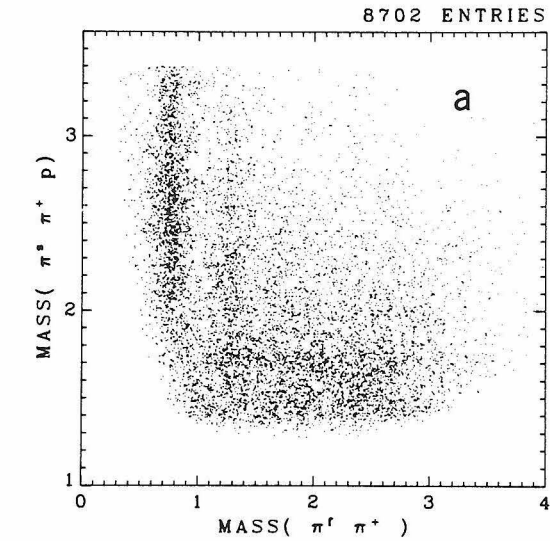
$\pi^b p^l \rightarrow \pi^f \pi^s \pi^+ p$ . 14 GeV/c  
UNCUT



XBL 774-8361

FIG. 17.  $A_1$  and  $A_3$  enhancements are visible in the scattergram of events with  $M(N^*) < 3.4$  GeV. We illustrate suppression of the A's by b) the cut  $M(N^*) < 2.6$  GeV, c) this cut combined with  $M(\pi^f \pi^+) > 1.45$  GeV, and d) this cut combined with selection of  $\Delta^{++}$  by the cut  $1.15 < M(\pi^+ p) < 1.32$  GeV.

$\pi^b p^t \rightarrow \pi^f \pi^s \pi^+ p$ , 14 GeV/c  
UNCUT



XBL 774-8362

FIG. 18. The  $\rho^0$  and the  $f(1270)$  are strong signals in the  $\pi^f \pi^+$  system, even when  $M(N^*) < 2.6$  GeV. We remove them from the sample either explicitly or for some purposes by selecting  $\Delta^{++}$  with the cut  $1.15 < M(\pi^+ p) < 1.32$  GeV as in c).

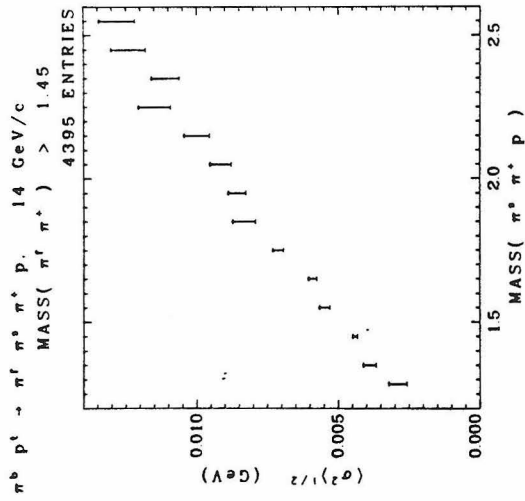


FIG. 19. Mass resolution for the  $\pi^S \pi^+ p$  system (r.m.s. of the errors calculated by SQUAW). The resolution for the two-body masses is similar.

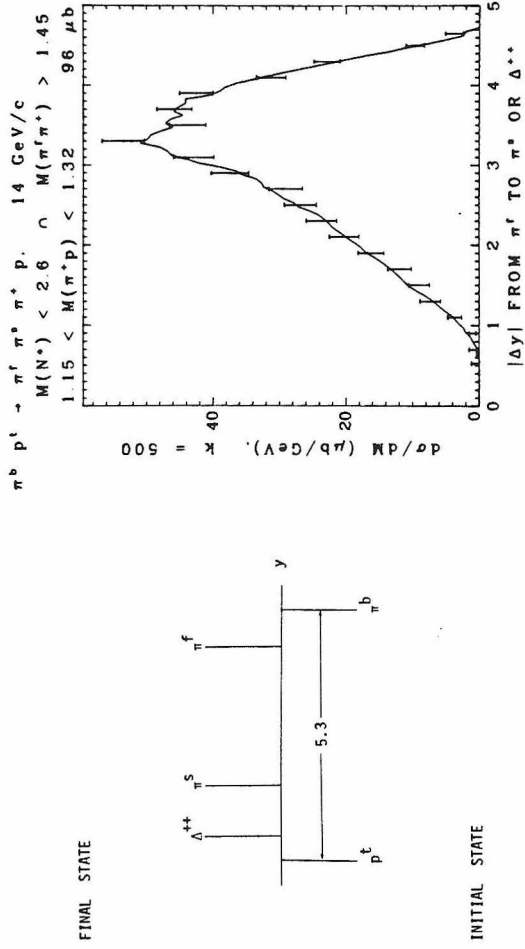
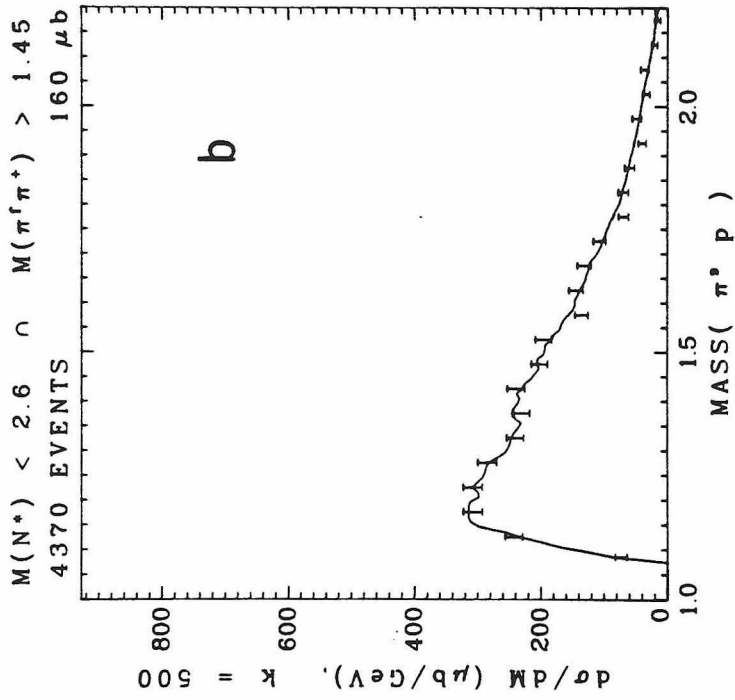
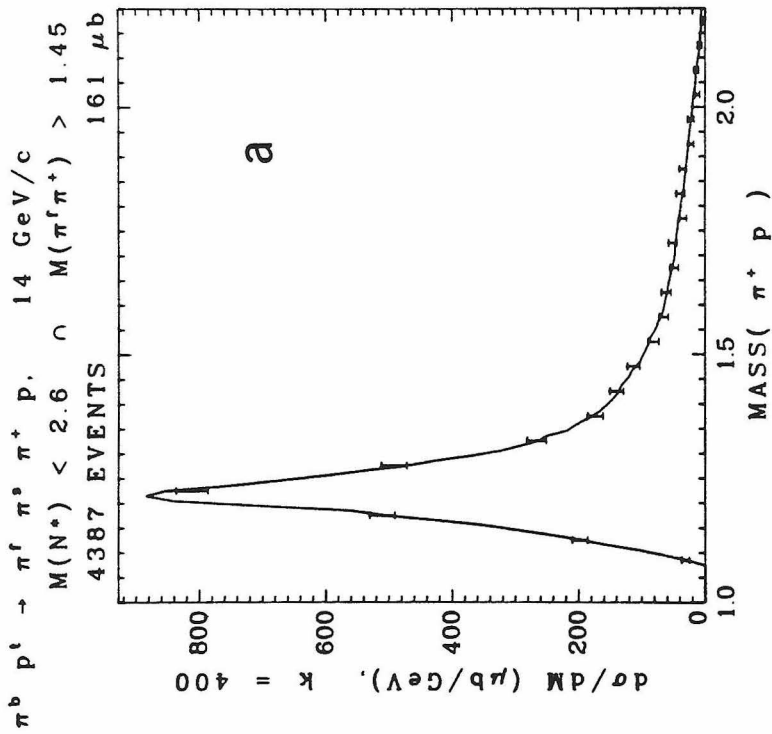
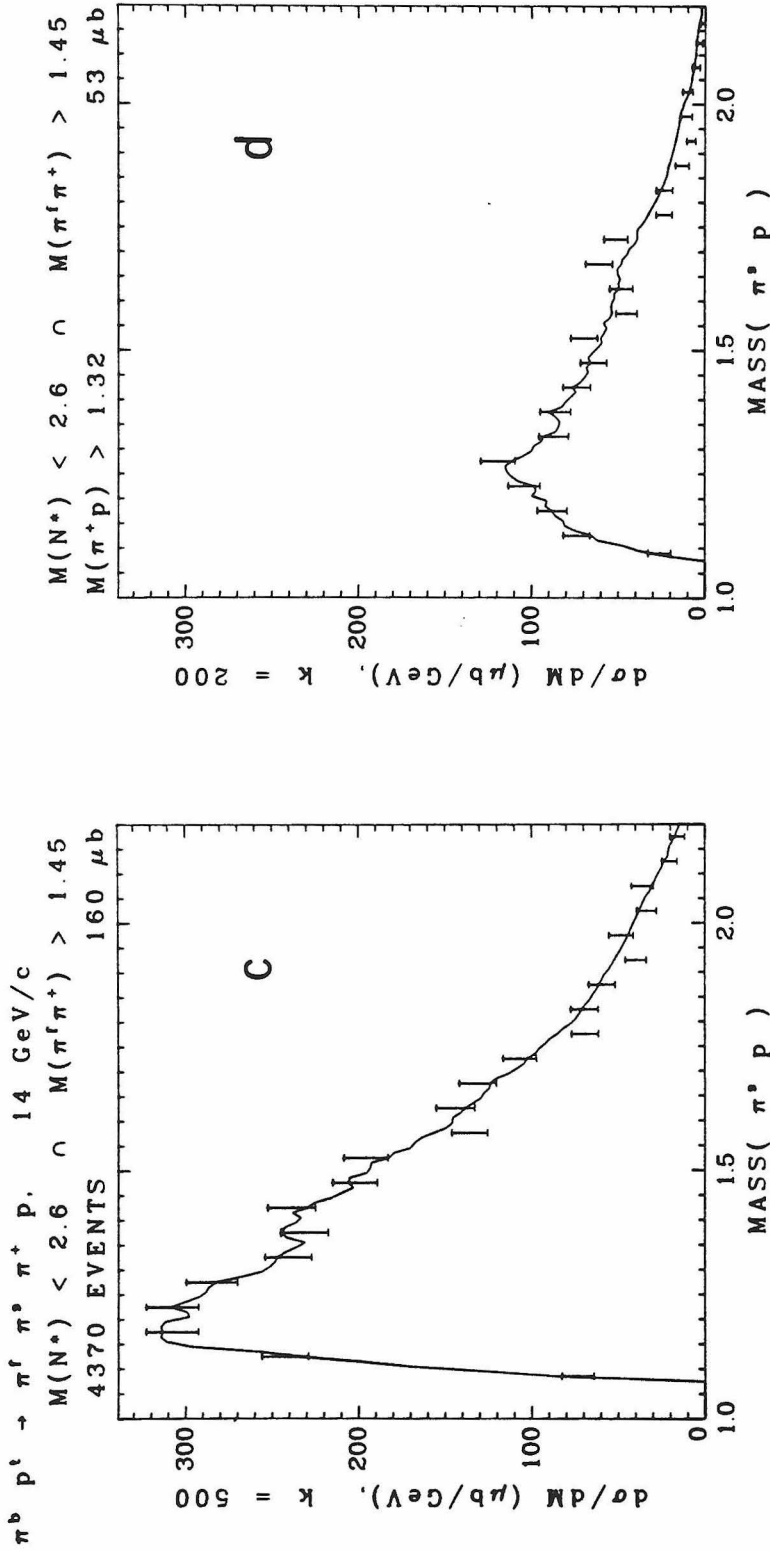


FIG. 20a. Schematic of the rapidity gaps for the reaction  $\pi^b p \rightarrow \pi^f \pi^S \Delta^{++}$ .



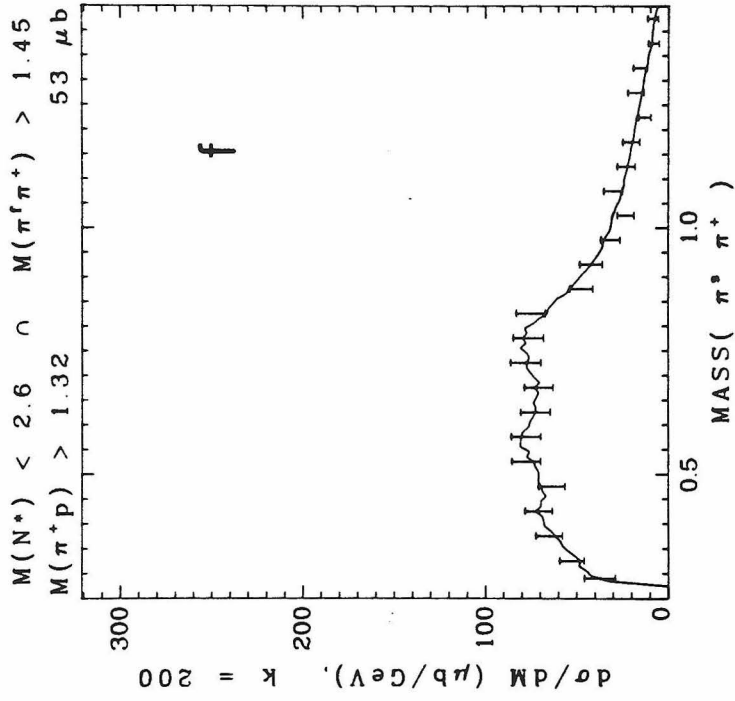
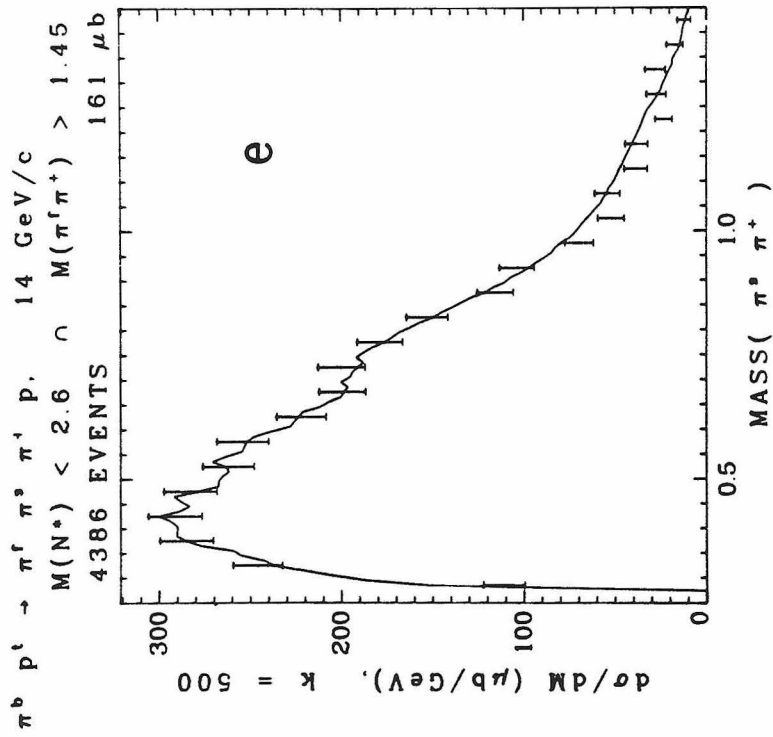
XBL 774-8350

FIG. 21. Two-body mass distributions. b) and c) differ only in vertical scale. In d) and f) we suppress the  $\Delta^{++}$  by the cut  $M(\pi^+ p) > 1.32 \text{ GeV}$ .



XBL 774-8351

FIG. 21 (continued).



XBL 774-8352

FIG. 21 (continued).

The minimum detection efficiency is just under 20% in the region of the  $M, t$  plane defined by cuts (6.1) and (6.2). As indicated in Figure 17c cut (6.3) eliminates the last vestiges of the  $A$  enhancements as well as the  $\rho^0$  and the  $f$ . (We refer to Figures 17d and 18c in a later section.)

The observable mass spectra are a convolution of the natural distributions with a resolution function arising from the errors of measurement. The width of the resolution function is less than 15 MeV for all of the particle combinations. To show how the resolution depends on mass we display in Figure 19 the root-mean-square of the errors of the  $\pi^S \pi^+ p$  masses. These errors are a part of the output of the SQUAW kinematic fitting program. We discuss their validity in Section III.8. The resolution as a function of mass for the two-body masses is so similar to Figure 19 that we omit the displays. The resolution has no material impact on the shape of the mass spectra we are about to present since the width of the narrowest structures which appear is several times 15 MeV.

In Figures 21a-f we present the mass spectra of the  $\pi^+ p$ ,  $\pi^S p$ , and  $\pi^S \pi^+$  systems. The  $\pi^+ p$  system, Figure 21a, exhibits a dominant  $\Delta^{++}(1230)$  enhancement but no other identifiable structures. By contrast the  $\pi^S p$  system, Figure 21b or 21c, exhibits neither a clear  $\Delta^0(1230)$  signal nor any other resonance peaks.

The dominance of the doubly charged state of the  $\Delta(1230)$  is a consequence of a well established property of strong interactions and of the values of certain Clebsch-Gordan coefficients. The property we refer

to is that amplitudes which incorporate the exchange of an internal quantum number, such as (nonzero) isotopic spin, across a rapidity gap larger than  $\approx 2.0$  are small compared with otherwise similar amplitudes which do not incorporate such an exchange. Evidence for this general rule comes first from the  $s$  dependence of two body exchange reactions, e.g.,  $\pi^- p \rightarrow \pi^0 n$ , relative to their elastic counterparts [Fox and Quigg 1973]. Studies of dissociation reactions have also supported this idea [Beaupré et al. 1971b, Boesebeck et al. 1972, Colley et al. 1973, Beaupré et al. 1973]. In the initial state of the present experiment the rapidity gap is 5.3. In the final state the gap which separates the  $\pi^f$  from its nearest neighbor in the  $\pi^S \Delta^{++}$  system may be smaller as we show schematically in Figure 20a. In Figure 20b we demonstrate that gap sizes greater than 2.0 are preponderant even in the final state. The rule about quantum number exchange therefore implies that  $I = 1/2$  dominates the isotopic spin content of the  $\pi^S \Delta^{++}$  system. Colley et al. [1973] demonstrate explicitly in the reactions  $K^+ p \rightarrow K \pi \pi p$  at 10 GeV/c that the  $I = 3/2$  intensity in the  $\pi \pi p$  system is about 6%.

Here enter the Clebsch-Gordan coefficients. When  $I_{N^*} = 1/2$ , the relative intensity of  $\pi^+ \Delta^0$  to  $\pi^- \Delta^{++}$  is 1/3. The branching fraction of the  $\Delta^0$  to  $\pi^- p$  is also 1/3. The ratio of observable  $\Delta^0$  to  $\Delta^{++}$  in reaction (3.1) is the product 1/9. This analysis applies only to the  $I = 3/2$  portions of the  $\pi p$  subsystems. The mass distribution of  $M(\pi^- p)$ , Figure b, results from a coherent sum of  $I = 1/2$  and  $I = 3/2$  contributions so that at  $M(\pi p) = 1.23$  GeV the cross

section ratio is close to 0.3 instead of 1/9. The  $I = 1/2$  background thus obscures the  $\Delta^0(1230)$  production which might otherwise be visible as a small peak.

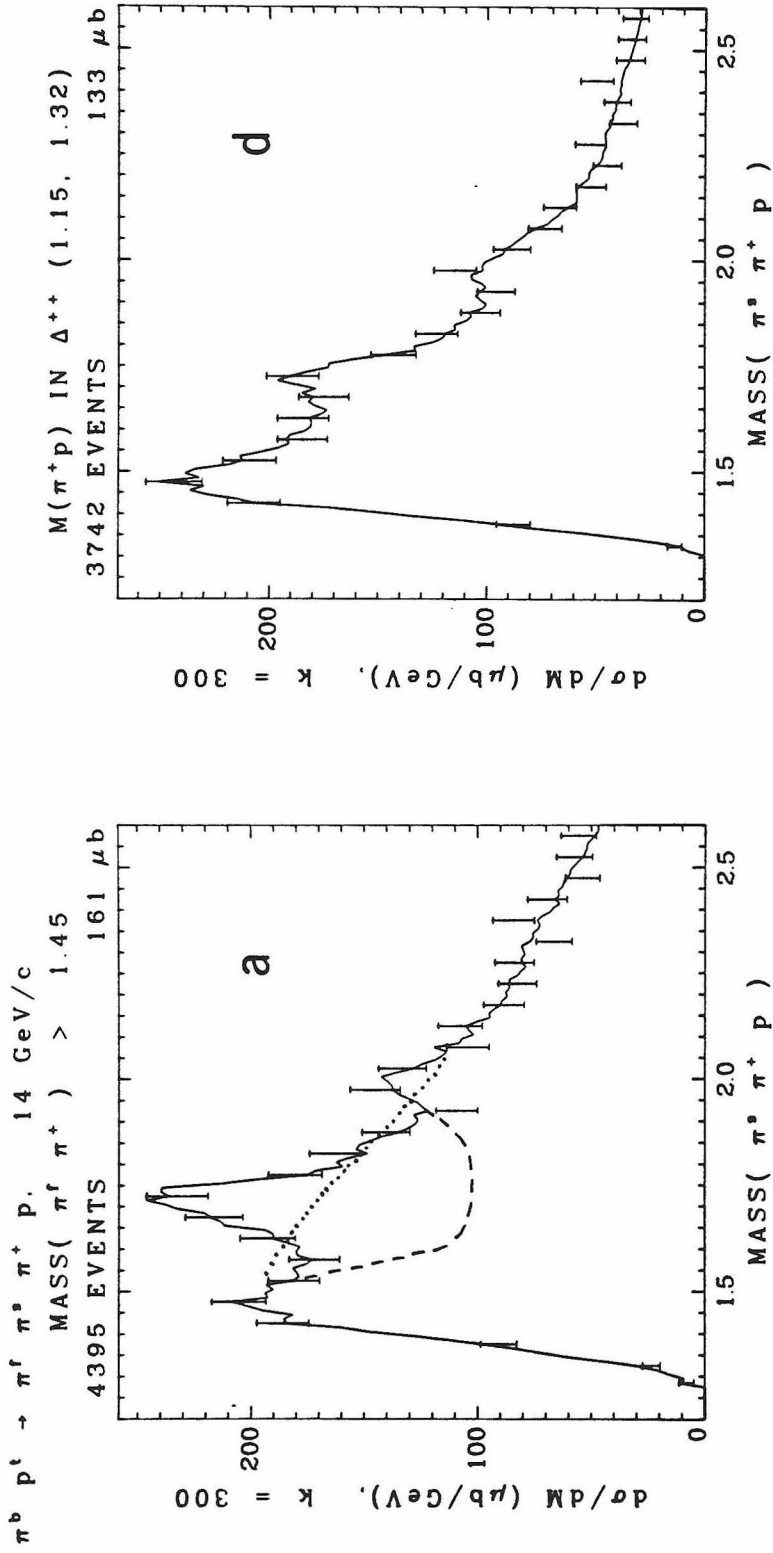
The  $\pi^S\pi^+$  mass spectrum, Figure 21e, is also featureless unless one regards as a feature the absence of a significant  $\rho^0(770)$  enhancement. In Figures 21d and 21f we show the  $\pi^S p$  and  $\pi^S\pi^+$  mass distributions after removing most of the  $\Delta^{++}(1230)$  by requiring

$$M(\pi^+ p) > 1.32 . \quad (6.4)$$

Still no resonance peaks stand out. A shoulder in the distribution of Figure 21f at 0.80 GeV suggests that production of  $\rho^0$  is not altogether missing.

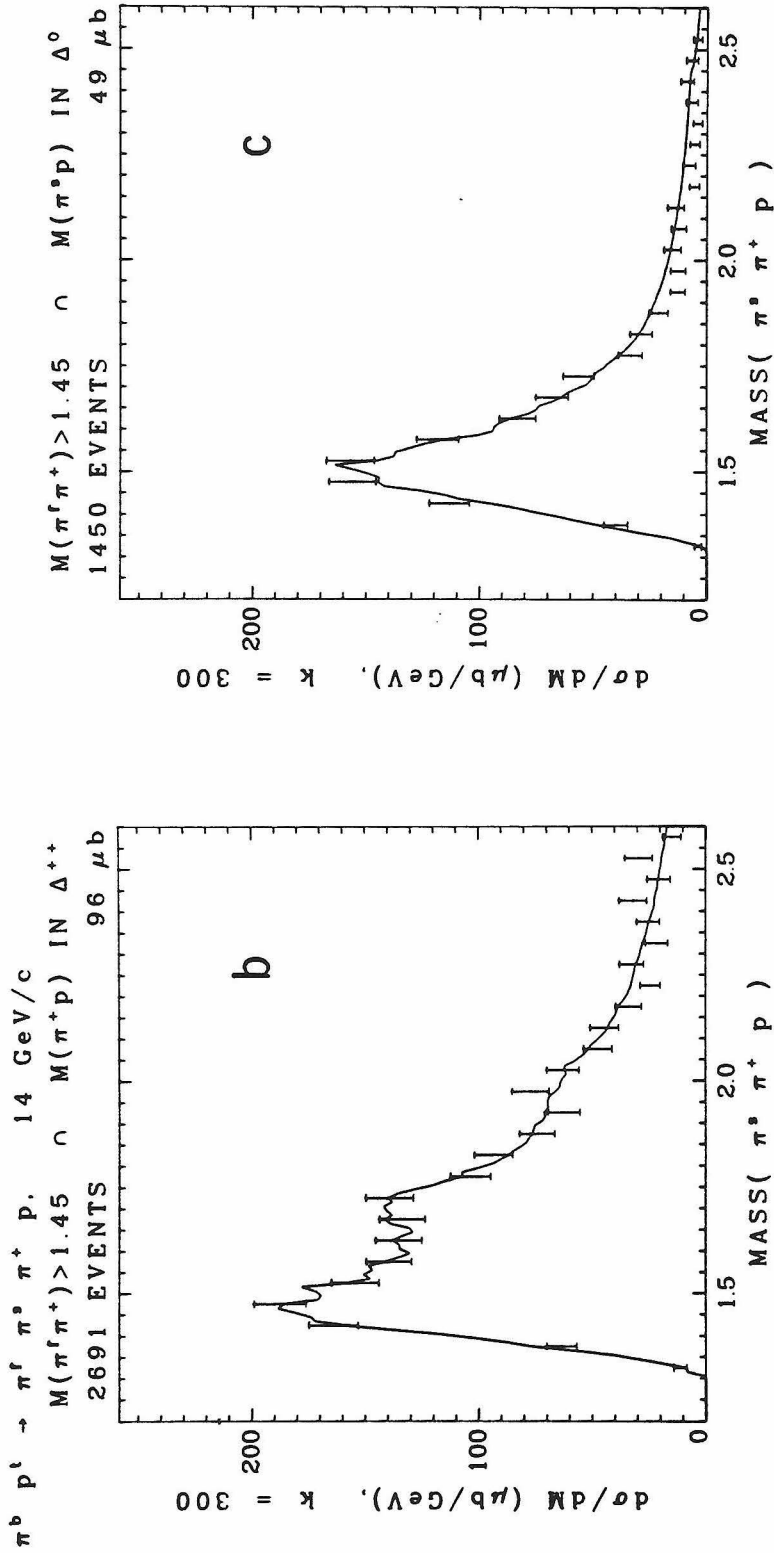
In Figure 22a we present the mass distribution of the  $\pi^S\pi^+p$  system. We determined the position of the lowest peak to be 1.49 GeV by "eyeball" from Figure 22a. To determine the error we generated twenty additional versions of the distribution of Figure 22a by a Monte-Carlo method. For each of these we estimated the peak position in the same informal way as we did for the data. The dispersion ( $\sigma$ ) of this sample of twenty estimates was 20 MeV.

Often a distribution has the character of a resonance superposed on a "smooth" background. In such cases the data alone are sufficiently informative on the shape of the background to permit estimation of the width and cross section of the resonance. In the present case we cannot presume the background to be smooth because of proximity to threshold. We also cannot presume that the background near 1.5 GeV is very small



XBL 774-8353

FIG. 22. a) Distribution of the  $N^*$  mass after a cut which removes the  $A$ ,  $\rho^0$ , and  $f$  in the  $f_2^+ \pi^+ \pi^0$  and  $\pi^+ \pi^0$  systems. We discuss the dotted and dashed curves in Section IV.8. b,c) The distribution after additional cuts to select  $\Delta^{++}$  and  $\Delta^0$ . d) With only the  $\Delta^{++}$  cut. This sample is also free of  $A$ ,  $\rho^0$ , and  $f$ .



XBL 774-8354

FIG. 22 (continued).

because we will later present certain angular distributions which are evidence to the contrary (see Section IV.7). Under these circumstances estimation of resonance width and cross section is a heavily model dependent project which we have elected not to undertake.

In Table IV.B we list some statistics of the 1.72 GeV feature of Figure 22a. These estimates also came directly from the figure without benefit of a fitting procedure. For the peak position and its error

TABLE IV.B.--Parameters of the enhancement at 1.72 GeV.

Peak position	$1.720 \pm 0.015$ GeV
Width (FWHM)	$0.100 < \Gamma < 0.160$ GeV
Cross section in excess of background	$8 < \delta < 25$ $\mu$ b
Cross section for the interval 1.6-1.8 GeV	$41 \pm 6$ $\mu$ b
$\frac{N^*(1720) \rightarrow \pi \Delta \rightarrow \pi \pi p}{N^*(1720) \rightarrow \pi^S \pi^+ p}$	$\gg 0.1$ , consistent with 1.0

our method was the same as described above for the 1.49 GeV peak. The background may bias the peak in the data away from the center of the responsible resonance by an amount which depends on the background slope and the resonance width. In the present case if the background falls precipitously at 1.7 GeV, the peak of the distribution could occur as much as 20 MeV below the resonance mass, an amount comparable to the

statistical error. The unknown shape of the background creates the major uncertainty in the width of the enhancement and in the cross section above background. The dotted and the dashed curves which we have superposed on the data in Figure 22a are two widely separated possibilities for the background shape. The limits for the width and cross section quoted in Table IV.B correspond to these curves. The dominant source of error of the cross section for the 1.6-1.8 GeV interval is the overall normalization uncertainty.

In Figure 22b we display the  $\pi^S \pi^+ p$  mass spectrum subject to the constraint that the  $\pi^+ p$  mass lie between 1.15 and 1.32 GeV. For comparison we show in Figure 22c the  $\pi^S \pi^+ p$  mass spectrum with the analogous cut on the  $\pi^S p$  mass. Bin for bin the available phase space is the same in the two figures because of the symmetry in the kinematics.<sup>†</sup> If the 1.72 GeV enhancement were to have no  $\pi\Delta(1230)$  decay mode, we would expect to observe it with roughly the same strength in each figure. On the other hand if the decay were exclusively via  $\pi\Delta(1230)$ , the Clebsch-Gordan coefficients for the isospin decomposition place 90% of the intensity in the  $\pi^S \Delta^{++}$  mode, 10% in the  $\pi^+ \Delta^0$  mode. The observation favors a substantial branching fraction to  $\pi\Delta(1230)$ . Figures 22b and 22c are not obviously inconsistent with 100%. If the

<sup>†</sup>The requirement  $M(\pi^f \pi^+) > 1.45$  GeV, potentially disturbs the kinematic symmetry. To check the importance of this effect we generated distributions like Figures 22b and 22c but with symmetry restored by the additional cut  $M(\pi^f \pi^S) > 1.45$  GeV. The shapes of the new distributions were substantially the same as those shown.

ratio

$$\frac{\Gamma (N^*(1720) \rightarrow \pi\Delta(1230))}{\Gamma (N^*(1720) \rightarrow \text{all } \pi^+\pi^-p)}$$

were as small as 0.1 (and if we ignore interference effects), we would expect the strength of the enhancement in Figure 22c to be about 80% of its strength in Figure 22b. Clearly the figures require a branching fraction greater than 10%. This reasoning is the basis for the last line of Table IV.B. A more quantitative treatment is a formidable statistical problem which would necessitate adoption of a dynamical model to account for the background. We have not pursued this sophisticated kind of analysis.

Our peak at 2.0 GeV (see Figure 22a) stands about two standard deviations above a smooth background. Colton et al. [1971], studying  $pp \rightarrow pp\pi^+\pi^-$ , also noticed an enhancement in the  $p\pi^+\pi^-$  system at this mass. The Review of Particle Properties [Particle Data Group 1976] lists two  $N^*$  states near 2.0 GeV, both determined from  $\pi N$  elastic phase shift analyses. The spin-parities are  $5/2^+$  and  $7/2^+$ . The statistical significance of our effect is so low that it will not tolerate further discussion or analysis.

In the next section we will present certain angular distributions and their moments which bear strongly on nonresonant production mechanisms. We will then return to discuss further the enhancements at 1.49 and 1.72 GeV.

## 7. Production of $\Delta^{++}(1230)$

In this section and in those to follow we consider the " $\Delta$  subset" of the data which we define by the constraints

$$M(\pi^S \pi^+ p) < 2.6 \text{ GeV} \quad (7.1a)$$

$$-t(\pi^b \rightarrow \pi^f) < 0.5 \text{ GeV}^2 \quad (7.1b)$$

$$1.15 < M(\pi^+ p) < 1.32 \text{ GeV} \quad (7.1c)$$

A number of characteristics of this subset merit discussion both because of their intrinsic interest and because they facilitate further analysis. First, the subset is large. Integration in Figure 21a over the interval 1.15-1.32 GeV shows that the cut (7.1c) includes about 60% of the target dissociation cross section.

A second helpful feature is that the selection criteria are not only sufficient to reduce the background but also compatible with certain methods of analysis which we can usefully pursue. Since we will examine the distributions of several angles which are kinematically coupled to the  $\pi^f \pi^+$  mass, a cut on this variable, though appropriate for the previous section, becomes unsuitable. These angles are not coupled to the variables appearing in inequalities (7.1). In Figure 17d and 18c we demonstrate that condition (7.1c) adequately suppresses the enhancements in the  $\pi^f \pi^S \pi^+$  and  $\pi^f \pi^+$  systems. A residual  $f$  peak is still evident in Figure 18c, but indications of the  $A$ 's and the  $\rho^0$  have disappeared.

In Figure 22d we display the  $\pi^S \pi^+ p$  mass spectrum for the  $\Delta$

subset. Its shape is similar to the distribution of Figure b where the  $\pi^+p$  and  $\pi^f\pi^+$  mass cuts were both operative.

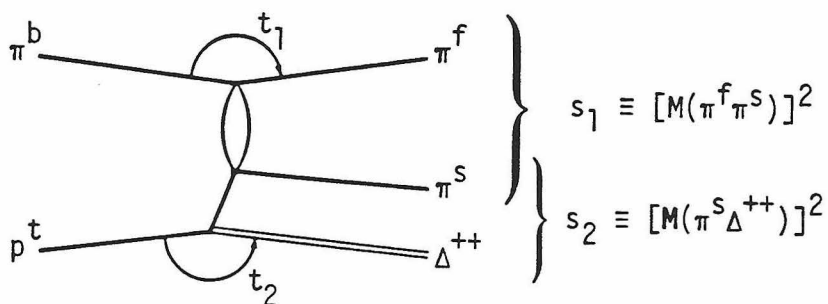
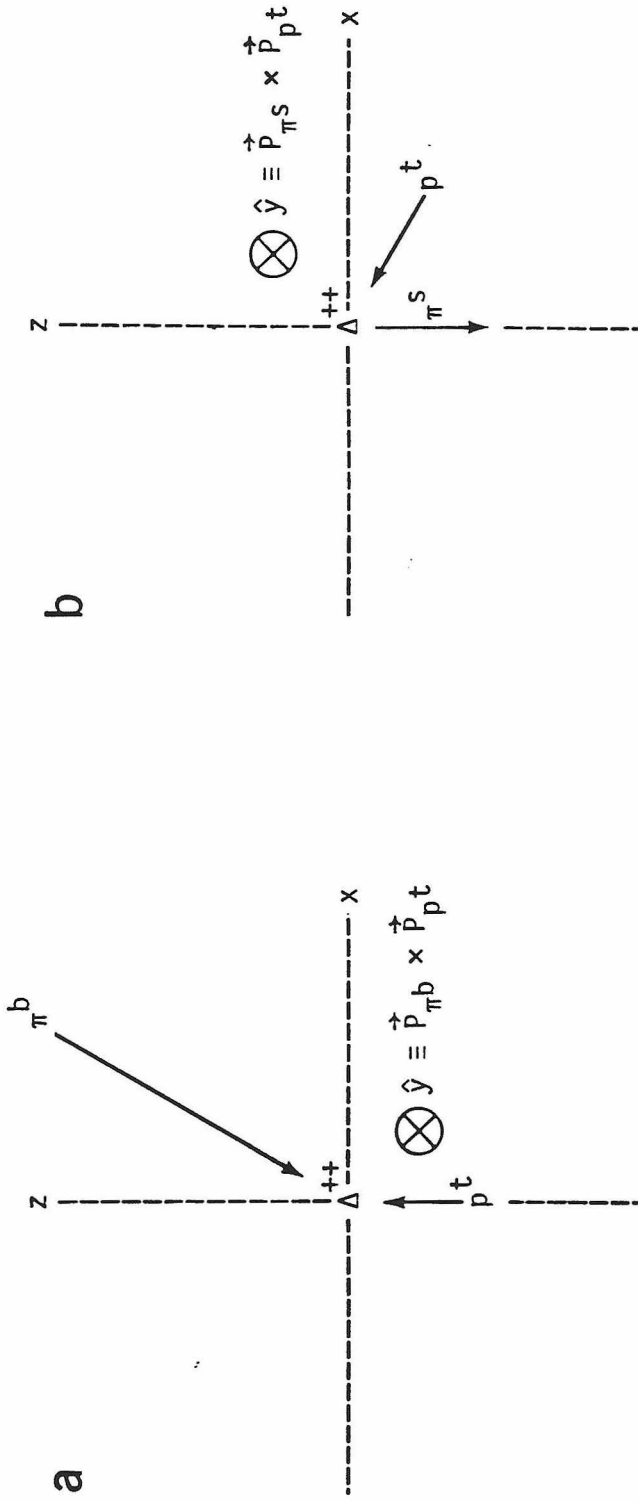


FIG. 23. The Deck mechanism for the process  $\pi p \rightarrow \pi \pi \Delta$ .

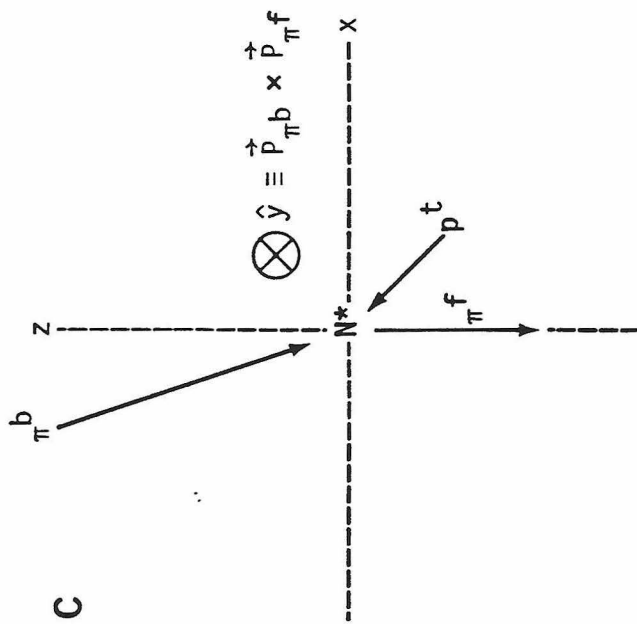
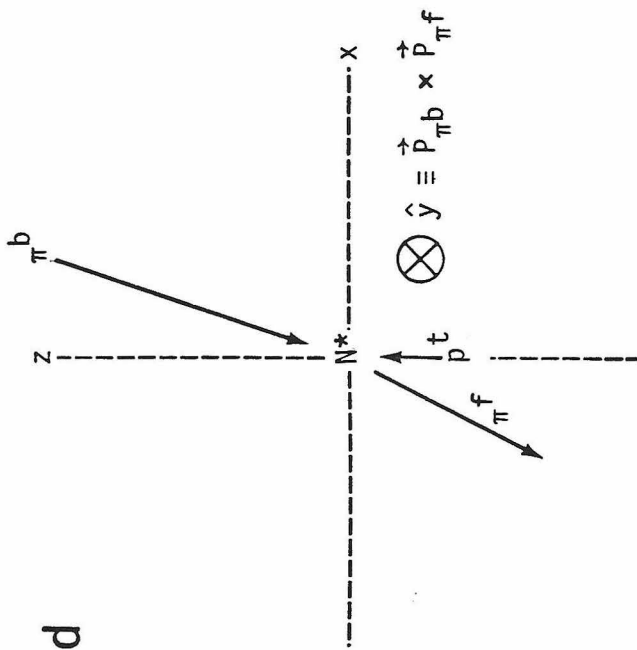
In the rest of this section we present evidence that the cross section for the  $\Delta$  subset comes dominantly from an amplitude corresponding to the diagram of Figure 23. The line connecting the  $\pi^S$  with the  $\Delta^{++}$  represents  $\pi$  exchange, and the bubble connecting the  $\pi^f$  with the  $\pi^S$  represents off-mass-shell  $\pi^-\pi^-$  elastic scattering. Deck [1964] and Drell and Hida [1961] first pointed out that diagrams of this type are an alternative to resonance formation as an explanation of threshold enhancements. The angular momentum properties of the  $\pi\Delta$  vertex of Figure 23 have an easily recognizable signature in the  $\Delta^{++}$  t-channel frame which we define in Figure 24a. If we assume that the exchanged pion is spinless (no Reggeization), the z projection of the  $\Delta^{++}$  spin must



$\Delta^{++}$  t-channel frame. The  $\Delta^{++}$  is at rest. Not shown are the  $\pi^f$ ,  $\pi^s$ , and the daughters of the  $\Delta^{++}$ .

$\Delta^{++}$  secondary decay frame. The  $\Delta^{++}$  is at rest. Not shown are the  $\pi^b$ ,  $\pi^f$ , and the daughters of the  $\Delta^{++}$ .

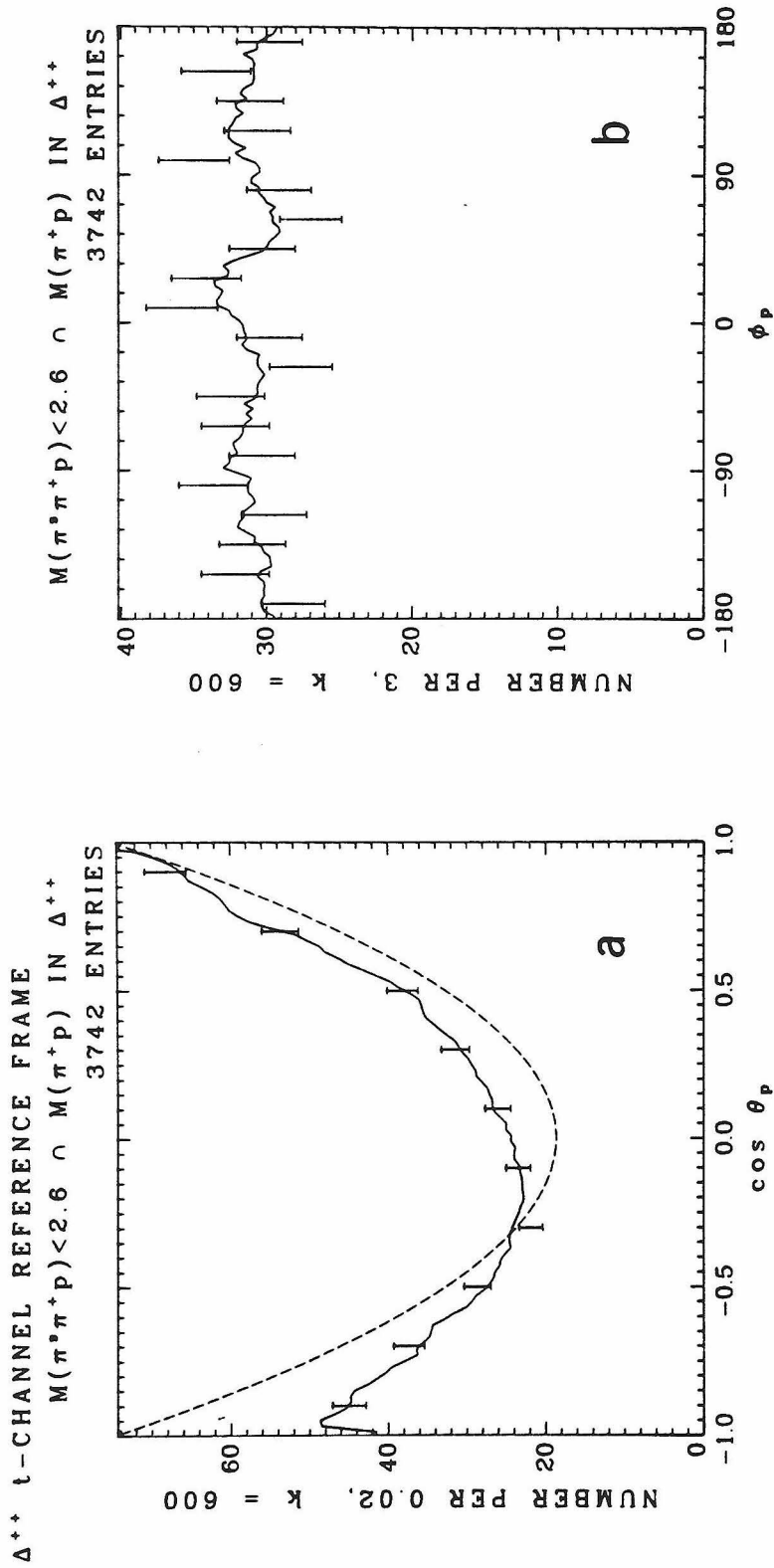
FIG. 24. Definitions of four reference frames in which we present angular distributions. A vector  $\hat{V}$  in any of these frames has spherical coordinates  $\theta, \phi$  with  $\cos \theta = (\hat{z} \cdot \hat{V}) / |\hat{V}|$  and  $\phi$  measured from  $\hat{x}$ .



$N^*$  t-channel frame. The  $N^*$  is at rest.  
 Not shown are the daughters of the  $N^*$   
 ( $\pi^S$ ,  $\pi^+$ , and p).

$N^*$  s-channel frame. The  $N^*$  is at rest.  
 Not shown are the daughters of the  $N^*$   
 ( $\pi^S$ ,  $\pi^+$ , and p).

FIG. 24 (continued).



XBL 774-8355

FIG. 25. a) Polar and b) azimuthal distributions for the  $\Delta^{++}$  decay in the  $\Delta^{++}$  t-channel reference frame (Fig. 8a). Included are all events with  $1.15 < M(\pi^+p) < 1.32$  GeV. The dashed curve in a) is the function  $1+3 \cos^2 \theta_p$  normalized to the number of events. The data would take this shape if the  $\pi^+p$  system were pure  $J^P=3/2^+$  and if  $J_z$  were a mixture of  $+1/2$  and  $-1/2$ . Under these same conditions the  $\phi_p$  distribution would be uniform.

be the same as the helicity of the incoming target proton. In the decay of the  $\Delta^{++}$  the  $J_z = \pm 1/2$  states therefore add incoherently, and the decay angular distribution produced from an unpolarized target must be

$$\begin{aligned}
 W(\cos \theta_p, \phi_p) &= \frac{1}{2} \{ |D_{\frac{1}{2} \frac{1}{2}}^{3/2}(\phi_p, \theta_p, 0)|^2 + |D_{\frac{1}{2} -\frac{1}{2}}^{3/2}|^2 + |D_{-\frac{1}{2} \frac{1}{2}}^{3/2}|^2 + |D_{-\frac{1}{2} -\frac{1}{2}}^{3/2}|^2 \} \\
 &= \frac{1}{8\pi} (1 + 3 \cos^2 \theta_p) \\
 &= \frac{1}{2\pi} \left[ \frac{1}{2} + \frac{1}{2} D_{00}^2(\Omega_p) \right] \tag{7.2}
 \end{aligned}$$

The D functions are the matrix elements of finite rotations [Edmonds 1957]. If we suppose that the orbital angular momentum of the  $\pi^+ p$  system is less than two, the available spin-parities are  $1/2^+$ ,  $1/2^-$ , and  $3/2^+$ . When only  $1/2^+$  and  $1/2^-$  states contribute, the maximum power of  $\cos \theta$  which can appear in the distribution function is one. Therefore nonzero values of the moment  $\langle D_{00}^2(\Omega_p) \rangle$  are attributable exclusively to the  $\Delta^{++}$  and to its interference with the background. That  $W(\cos \theta_p, \phi_p)$  is independent of the Treiman-Yang angle,  $\phi_p$  [Treiman and Yang 1962], is a more general attribute of  $\pi$  exchange which we will also compare with the data.

In Figure 25a we display the distribution of  $\cos \theta_p$  and in Figure 25b the distribution of  $\phi_p$ . The average values of the low order D functions are

$$\langle D_{00}^1 \rangle = 0.108 \pm 0.011$$

$$\langle D_{00}^2 \rangle = 0.148 \pm 0.008$$

$$\left. \begin{array}{l} \langle D_{10}^1 \rangle \\ \langle D_{10}^2 \rangle \\ \langle D_{20}^2 \rangle \end{array} \right\} \approx (0 \pm 0.005) + (0 \pm 0.005)i \quad (7.3)$$

To determine whether the moments  $\langle D_{00}^1 \rangle$  and  $\langle D_{00}^2 \rangle$  alone fully describe the  $\cos \theta_p$  distribution we computed the Kuiper statistic (see Appendix B) of the data relative to the probability density

$$f(\cos \theta_p) \equiv \frac{1}{2} + \frac{3}{2} \langle D_{00}^1 \rangle D_{00}^1(\Omega_p) + \frac{5}{2} \langle D_{00}^2 \rangle D_{00}^2(\Omega_p) . \quad (7.4)$$

The result was  $V = 0.914$  for 3742 events. The corresponding confidence level for a simple hypothesis is 91%, but, since  $f(\cos \theta_p)$  is a composite hypothesis, this figure is an overestimate. We similarly tested the  $\phi_p$  distribution for uniformity. We computed the Kuiper statistic both for the full sample and for three subintervals of  $\cos \theta_p$ , and we list the results in Table IV.C. Our conclusion is that  $\langle D_{00}^1 \rangle$  and  $\langle D_{00}^2 \rangle$  are indeed a complete description of the joint angular distribution  $W(\Omega_p)$ . We postpone physical interpretation of this result until the end of this section.

Next we discuss the dependence of the distribution  $W(\Omega_p)$  on

the variables  $t_1 \equiv t(\pi^b \rightarrow \pi^f)$ ,  $M(\pi^S \pi^+ p)$ ,  $t_2 \equiv t(p \rightarrow \Delta^{++})$ , and  $M(\pi^+ p)$ . We divided the domain of each variable into several subintervals with comparable numbers of events, and we carried out on the data of each subinterval the same computations as we just described for the full subset. In all intervals the  $\cos \theta_p$  distribution was consistent with the form (7.4), and in all subintervals the  $\phi_p$  distribution was consistent with uniformity at the 0.5% confidence level.

$t_1$ : All moments of the  $D$  functions were consistent with their full-sample values; we found no indication that the distribution  $W(\Omega_p)$  depends on  $t_1$ . Because of this independence and because  $W(\Omega_p)$  is also substantially independent of  $M(\pi^S \pi^+ p)$ , we have not and we need not weight the events or otherwise account for the geometrical efficiency of the apparatus.

TABLE IV.C.--Kuiper statistics for uniformity of the  $\phi_p$  distribution in the  $\Delta^{++}$   $t$ -channel reference frame.

	Sample size	Kuiper statistic, $V$	Confidence level
$0.3 < \cos \theta_p < 0.9$	1410	1.06	0.73
$-0.3 < \cos \theta_p < 0.3$	766	1.13	0.62
$-0.9 < \cos \theta_p < -0.3$	967	1.35	0.31
all $\cos \theta_p$	3742	1.39	0.27

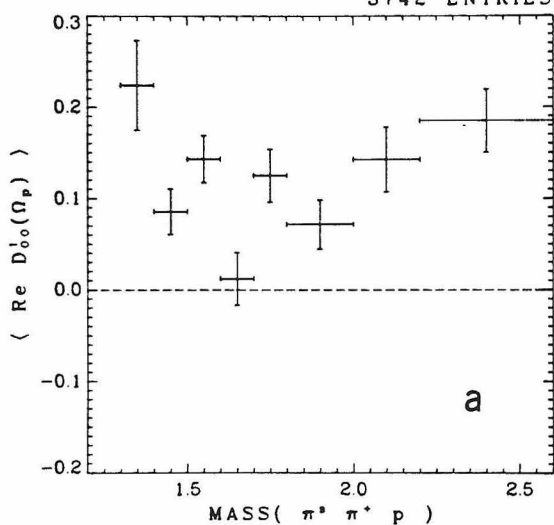
$M(\pi^S \pi^+ p)$ : In Figures 26a-c we display the moments  $\langle D_{00}^1 \rangle$ ,  $\langle D_{00}^2 \rangle$ , and  $\langle \text{Re } D_{10}^1 \rangle$  as functions of  $M(\pi^S \pi^+ p)$ .  $\langle D_{00}^2 \rangle$  (Figure 26b) appears consistent with the full-sample value in every interval.  $\langle D_{00}^1 \rangle$  (Figure 26a) shows variations of greater statistical significance. In particular we call attention to the dip at 1.65 GeV although we cannot offer any physical interpretation for it. The departure from zero of the moment  $\langle \text{Re } D_{10}^1 \rangle$  (Figure 26c) when  $M(\pi^S \pi^+ p) > 1.7$  GeV is marginally significant. Small negative values may reflect the vestigial  $f^0$  signal in the  $\pi^f \pi^+$  system rather than properties intrinsic to the  $N^*$ . All other moments were consistent with zero.

$M(\pi^+ p)$ : We present the  $\langle D_{00}^1 \rangle$  and  $\langle D_{00}^2 \rangle$  moments as a function of  $M(\pi^+ p)$  in Figures 26d,e. In this variable we can compare our data with on-shell  $\pi^+ p$  elastic scattering. From the phase shifts of the Saclay [1974] elastic phase shift analysis we calculated the points which we label with squares in the figure. The  $\langle D_{00}^2 \rangle$  (Figure 26e) moment of the present experiment is similar to but not quite as large as the on-shell moment. Our  $\langle D_{00}^1 \rangle$  (Figure 26d), on the other hand, has a distinctly different dependence on  $M(\pi^+ p)$  than its on-shell counterpart. The other moments were consistent with zero in all intervals of  $M(\pi^+ p)$ . Colton and Schlein [1969] compare off-shell with on-shell moments for the reactions

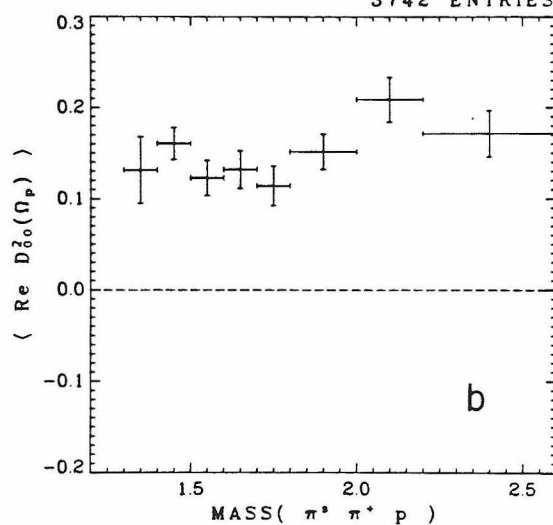
$$Xp \rightarrow X\pi^- (\pi^+ p) \quad (7.5)$$

$\Delta^{++}$  t-CHANNEL REFERENCE FRAME $M(\pi^+p)$  IN  $\Delta^{++}$  (1.15, 1.32)

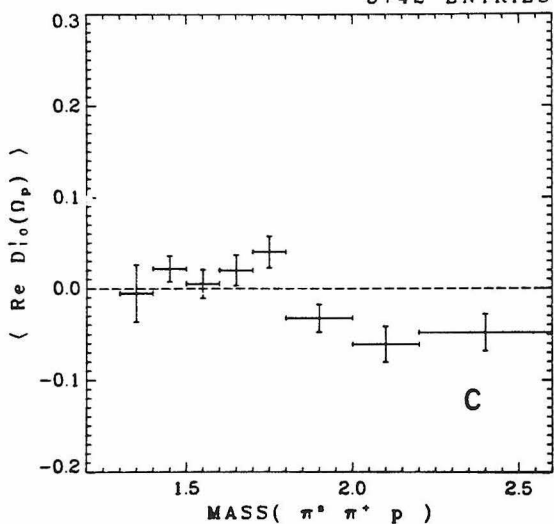
3742 ENTRIES

 $M(\pi^+p)$  IN  $\Delta^{++}$  (1.15, 1.32)

3742 ENTRIES

 $M(\pi^+p)$  IN  $\Delta^{++}$  (1.15, 1.32)

3742 ENTRIES



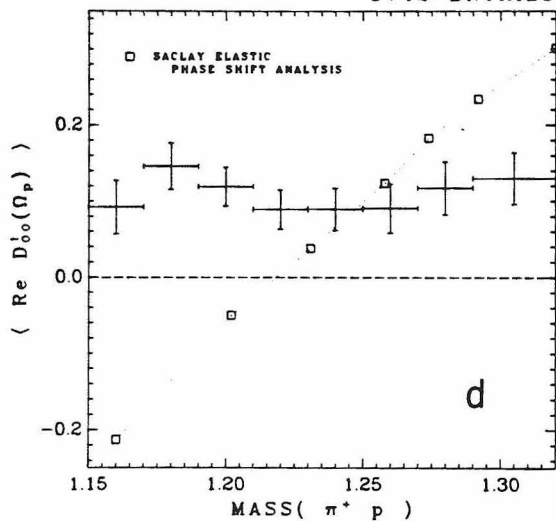
XBL 774-8363

FIG. 26. Moments of the  $\Delta^{++}$  decay distribution in the  $\Delta^{++}$  t-channel frame (defined in Fig. 8a). The abscissa is  $M(N^*)$  in a), b), and c),  $M(\pi^+p)$  in d) and e), and  $-t(p \rightarrow \Delta^{++})$  in f) and g).

$\Delta^{++}$  t-CHANNEL REFERENCE FRAME

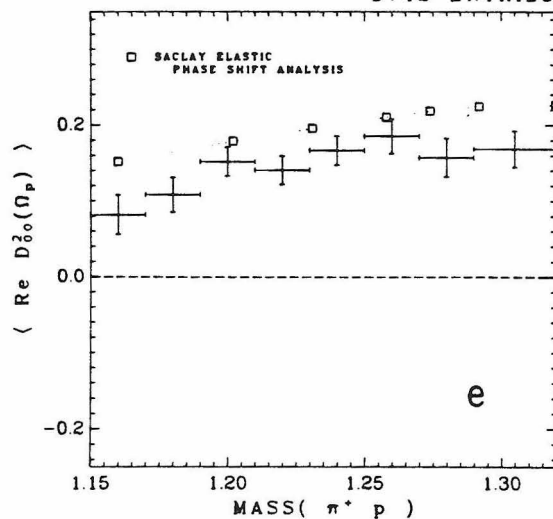
MASS(  $\pi^0 \pi^+ p$  ) < 2.6

3742 ENTRIES



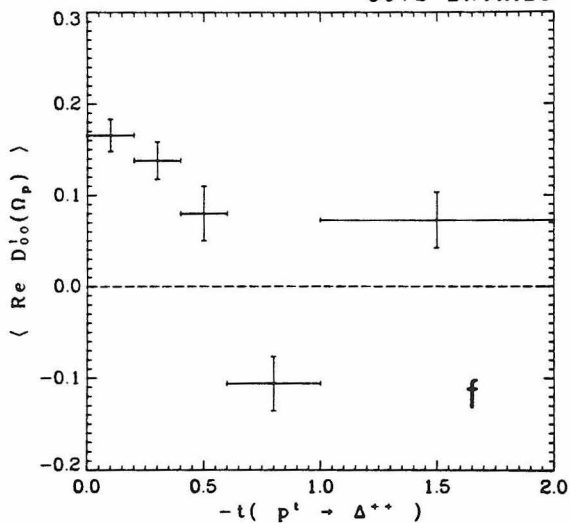
MASS(  $\pi^0 \pi^+ p$  ) < 2.6

3742 ENTRIES



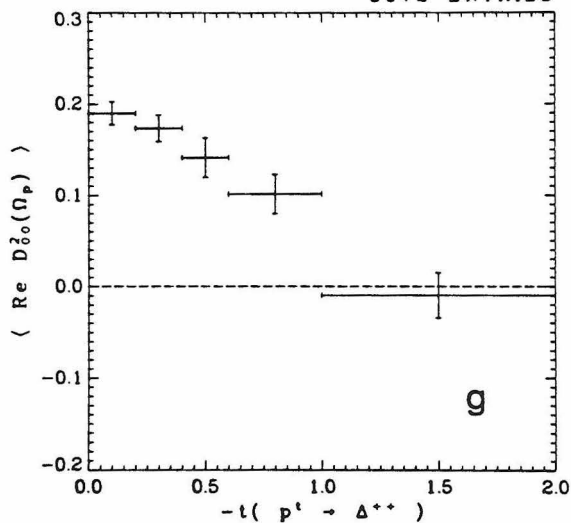
$M(\pi^0 \pi^+ p) < 2.6 \cap M(\pi^+ p)$  IN  $\Delta^{++}$

3672 ENTRIES



$M(\pi^0 \pi^+ p) < 2.6 \cap M(\pi^+ p)$  IN  $\Delta^{++}$

3672 ENTRIES



XBL 774-8365

FIG. 26 (continued).

with  $X$  a  $\pi^+$ ,  $K^+$ , or  $p$ . Their moments and ours all exhibit roughly the same departures from the on-shell dependence.

$t_2$ : As we see in Figures 26f,g the moments  $\langle D_{00}^1 \rangle$  and  $\langle D_{00}^2 \rangle$  depend heavily on this variable which measures the displacement of the exchanged pion from its mass shell.  $\langle D_{00}^1 \rangle$  (Fig. 26f) exhibits a pronounced dip at  $-t_2 = 0.8 \text{ GeV}^2$ , and  $\langle D_{00}^2 \rangle$  (Fig. 26g) falls from 0.2 to zero as  $-t_2$  grows from minimum ( $\approx 0.08$ ) to  $1.5 \text{ GeV}^2$ . The other moments were consistent with zero throughout the domain of  $t_2$ .

Although we cannot reconstruct amplitudes from our data, we can point out one broad hypothesis which explains the most prominent features of the  $\pi^+p$  decay angular distribution. We propose that production of  $\Delta^{++}(1230)$  by  $\pi$  exchange, Figure 23, dominates at the lowest values of  $|t_2|$ . Though it drops to zero as  $-t_2$  approaches  $1.5 \text{ GeV}^2$ , it generates most of the cross section and accounts for  $\langle D_{00}^2 \rangle \approx 0.2$ . Both  $\pi$  exchange and such other mechanisms as the decay of  $N^*$  resonances create small  $J^P = 1/2^+$  and  $1/2^-$  waves which interfere with the  $\Delta^{++}$  to produce the  $\langle D_{00}^1 \rangle$  moment. Variations of the small amplitudes with  $t_2$  and  $M(\pi^S \pi^+ p)$  contribute most to the dependence of  $\langle D_{00}^1 \rangle$  on these parameters.

#### 8. Further Discussion of $N^*$ Resonance Production.

Production of the  $P_{11} N^*(1470)$  resonance [Particle Data Group 1976] could conceivably account for most of the cross section in the  $1.49 \text{ GeV}$  enhancement. In view of the presentation of the preceding section we should regard this possibility as unlikely, but temporarily we put

aside that evidence and seek support for the resonance alternative. The decay distribution of the  $\Delta^{++}$  would provide a distinct signature of the production of  $N^*(1470)$  if the branching fraction  $\Gamma(N^*(1470) \rightarrow \pi\Delta) / \Gamma(N^*(1470) \rightarrow \text{all } \pi\pi N)$  were close to one. We are about to show that this signature does not appear in our data. Estimates of the branching fraction by Longacre et al. [1975] are the best available. Using three different methods they obtained three disparate values, 36%, 55%, and 74%. Since Longacre et al. clearly do not assure us that the branching fraction is actually high, our result is inconclusive concerning production of  $N^*(1470)$ .

We consider the distribution of  $\cos \theta_p$  in the  $\Delta^{++}$  secondary decay frame which we define in Figure 24b. In this frame the  $J_z$  of the  $\Delta$  is the same as its helicity in the rest frame of the  $N^*$ . Hence if the  $N^*$  has spin 1/2,  $J_z = \pm 1/2$ . Jackson [1965], pp. 354-357, gives a full discussion of sequential decays of this type. In particular he shows that the distribution of  $\cos \theta_p$  is

$$\begin{aligned} w(\cos \theta_p) &= \frac{1}{2} + \frac{1}{2} D_{00}^2(\theta_p) \\ &= \frac{1}{4} (1 + 3 \cos^2 \theta_p) . \end{aligned} \quad (8.1)$$

The moment

$$\begin{aligned} \langle D_{00}^2 \rangle &= \int w(\cos \theta_p) D_{00}^2(\theta_p) d(\cos \theta_p) \\ &= 0.2 . \end{aligned} \quad (8.2)$$

In Figure 27 we histogram  $\cos \theta_p$  for the 1.4-1.5 GeV interval of  $M(\pi^S \pi^+ p)$ . The distribution of the data is much flatter than the form (8.1). The measured  $\langle D_{00}^2 \rangle$  is  $0.047 \pm 0.017$  which is so different from 0.2 as to be inconsistent with dominance of the cross section by production and  $\pi\Delta(1230)$  decay of the  $N^*(1470)$  resonance.

Discussions of the composition of the 1.49 GeV enhancement in the  $\pi\pi p$  system have appeared previously in Rhode et al. [1969] (22 GeV proton), Morse et al. [1971] (7 and 25 GeV  $\pi^-$ ), Rushbrooke et al. [1971a] (16 GeV proton), Johnstad et al. [1972] (19 GeV proton), Colley et al. [1973] (10 GeV  $K^+$ ), Blobel et al. [1975] (12 and 24 GeV proton), and Antipov et al. [1975] (25 and 40 GeV  $\bar{p}$ ). Most of these analyses reached a conclusion similar to ours. None obtained a contradictory result.

We next mention a stimulating feature of the decay angular distribution of the events in the 1.72 GeV enhancement. Restricting attention to  $\Delta$  subset events (see inequalities (7.1)) with  $1.6 < M(N^*) < 1.8$  GeV, we show in Figure 28 the distribution of  $\cos \theta_\Delta$  in the  $N^*$  t-channel frame (the Gottfried-Jackson frame, see Figure 24d). This distribution has nearly the  $1+2\cos^2 \theta_\Delta$  shape which would result from production of a  $5/2^+$  resonance conserving t-channel helicity followed by P-wave (lowest L) decay to  $\pi\Delta$ . Most previous analyses have taken agreement of this sort as indicative of the nature of the resonance. (The previous work includes all references cited in discussion of the 1.49 GeV peak as well as Willmann et al. [1970] using 13.1 GeV  $\pi^+$  data and Lamsa et al. [1972] using  $\pi^+$  and  $\pi^-$  at 8 to 18 GeV.) In all cases, however, the conclusion rests on several unsupportable assumptions.

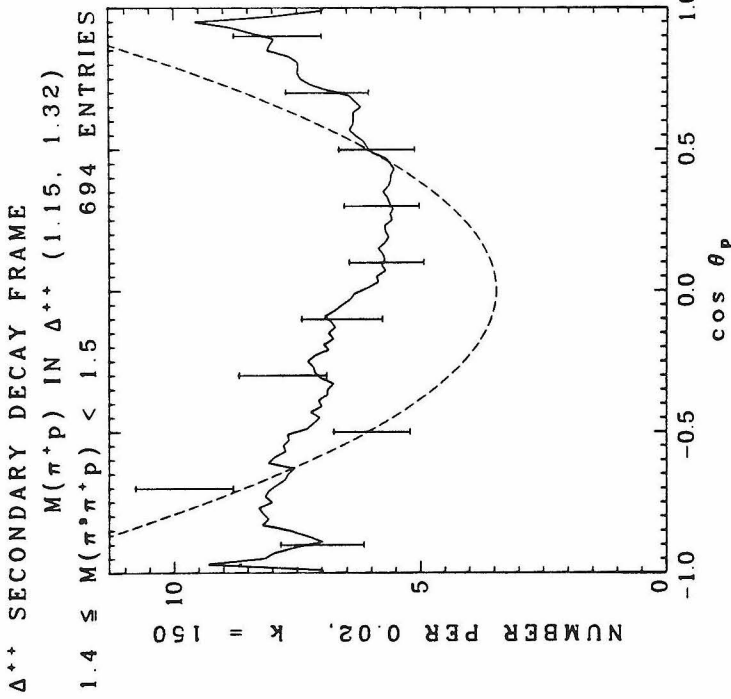


FIG. 27. The polar distribution of the  $\Delta^{++}$  decay in the  $\Delta^{++}$  secondary decay frame (Fig. 8b) for events near 1.47 GeV. The dashed curve is the function  $1+3 \cos^2 \theta_p$  normalized to the number of events. This shape would result from the second decay of the sequence  $N^*(1470) \rightarrow \pi^- \Delta^{++} \rightarrow \pi^- \pi^+ p$ .

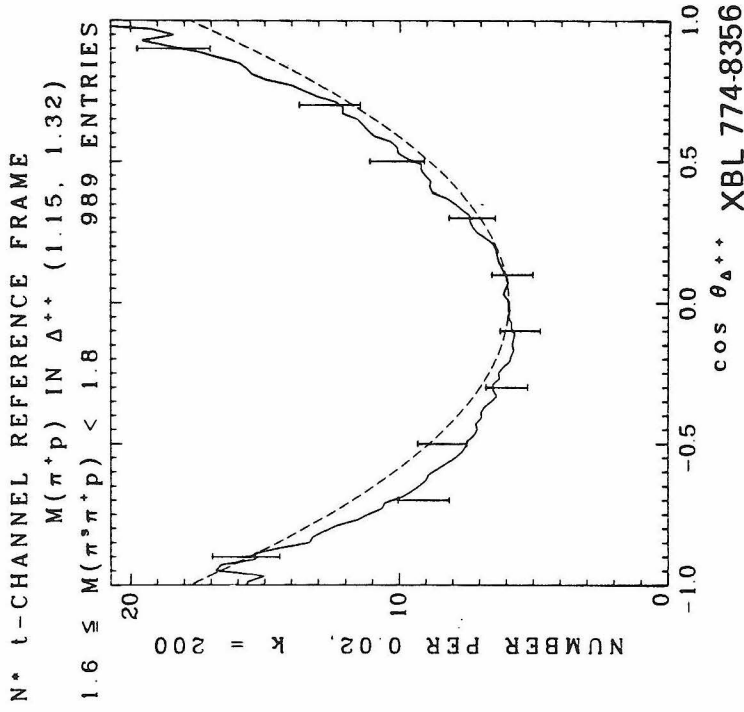


FIG. 28. The polar distribution of the decay  $N^* \rightarrow \pi^+ \Delta^{++}$  in the t-channel frame for events in the 1.72 GeV enhancement. The dashed curve is the function  $1+2 \cos^2 \theta_{\Delta^{++}}$  normalized to the number of events. A  $J^P = 5/2^+$   $N^*$  would generate this shape under some circumstances (see text). We argue that the good agreement here is quite likely fortuitous.

For example we would judge from Figure 22d that at 1.72 GeV the resonance contributes less than 50% of the cross section, though typical analyses assume 100%. Helicity conservation, be it s- or t-channel is closer to conjecture than to proven fact (see the next section). Furthermore the task is not merely to choose between two alternatives; candidate spin-parities are truly numerous. The partial wave analysis of  $\pi N \rightarrow \pi\pi N$  by Herndon et al. [1975] finds resonant behavior in the  $J^P$  states  $1/2^+$ ,  $1/2^-$ ,  $3/2^-$ ,  $5/2^+$ , and  $5/2^-$  all within the mass band 1.67 to 1.73 GeV and all having a  $\pi\Delta$  decay mode. To narrow the field by invoking the Gribov-Morrison rule (see Section IV.10) begs the question. Even to assume that a single spin-parity generates the enhancement seems unduly optimistic.

The partial wave analyses by Colley et al. and Blobel et al. waive a few of the dubious assumptions. At 1.72 GeV Blobel et al. find  $\approx 25\%$   $1/2^+$ ,  $\approx 50\%$   $3/2^-$ , and  $\approx 25\%$   $5/2^+$ , but they do not observe clear resonant behavior in any of these waves. Colley et al. were also unable to report resonant behavior.

We call attention to one other shortcoming of most previous work. An adequate description of the enhancement must be able to account for angular distributions even in a reference frame which is not germane to partial wave decomposition of the  $\pi^S \pi^+ p$  system. An example is the  $\Delta^{++}$  t-channel frame in which the distribution of  $\cos \theta_p$  has the distinctive shape which we discussed in the previous section. Of the cited analyses only Colley et al. specifically indicate agreement of their solution with this distribution.

In summary, we have not found in the literature a convincing spin-parity determination for the 1.72 GeV enhancement. Regretably the present experiment does not have the power to improve significantly on its antecedents. In the belief that only a major advance would be of any service, we stand mute on this issue.

## 9. Helicity Conservation

In this section we examine our data for consistency with the hypothesis of s-channel helicity conservation (sCHC) and t-channel helicity conservation (tCHC). The sCHC hypothesis asserts that in the overall center-of-mass frame the outgoing  $\pi^S \pi^+ p$  ( $N^*$ ) system has the same helicity as the incoming target proton. To test sCHC we prefer to work with angular distributions in the  $N^*$  s-channel frame which we define in Figure 24c. The two frames are related by a Lorentz boost along the s-channel z axis, so the  $J_z$  of the  $N^*$  in the s-channel frame is the same as its helicity in the CM frame. The tCHC hypothesis asserts that in the  $N^*$  t-channel frame defined in Figure 24d the  $J_z$  of the  $N^*$  is the same as the helicity of the target proton.

The initial spur to most of the work on helicity conservation was a paper by Gilman et al. [1970]. Because experimental evidence was favorable to sCHC in the reactions  $\gamma p \rightarrow \rho^0 p$  [Ballam et al. 1970] and  $\pi N \rightarrow \pi N$  [Hohler and Strauss 1970], they speculated that sCHC was characteristic of all diffractive resonance production. They were non-committal on the question of sCHC for diffractive nonresonant "background." Satz and Schilling [1971] argued from the principle of duality

that validity of sCHC for resonance production implied validity for background as well. Analyses of diffractively produced  $3\pi$  and  $K\pi\pi$  systems [e.g., Beaupré et al. 1971a] showed for resonance and background in combination that sCHC was invalid. For resonance production alone they were indecisive because the  $A_1$  and  $Q$  enhancements appear to be nonresonant [Antipov et al. 1973]. Concerning tCHC some investigations found consistency with observation [e.g., Beaupré et al. 1971a], others mild violation [e.g., Beaupré et al. 1972b], while still others found strong violation [Evans et al. 1973]. Distinguishing these investigations were both their techniques and the reactions studied.

Discussions of helicity conservation for diffractively produced  $\pi^+\pi^-p$  systems have appeared in Rushbrooke et al. [1971b] (16 GeV proton), Lamsa et al. [1972] ( $\pi^+$  and  $\pi^-$  at 8 to 18 GeV), Johnstad et al. [1972] (19 GeV proton), Beaupré et al. [1972a] (16 GeV  $\pi^+$  and  $\pi^-$  and 10 GeV  $K^-$ ), Beaupré et al. [1972b] (16 GeV  $\pi^-$  and 8 and 16 GeV  $\pi^+$ ), Chapman et al. [1973] (25 GeV deuterium), and Beketov et al. [1974] (4.5 GeV  $\pi^-$ ). All authors find large departures of their data from sCHC. Most find consistency with tCHC, but Rushbrooke et al., Johnstad et al., and Chapman et al. find some degree of violation. Our own analysis improves on previous work in four respects. 1) Our effective sample size is greater. 2) Our statistical techniques are more powerful. 3) We take explicit measures to suppress unwanted channels. 4) We consider separately the forward and backward  $\Delta^{++}$  production for  $M(N^*) > 1.7$  GeV.

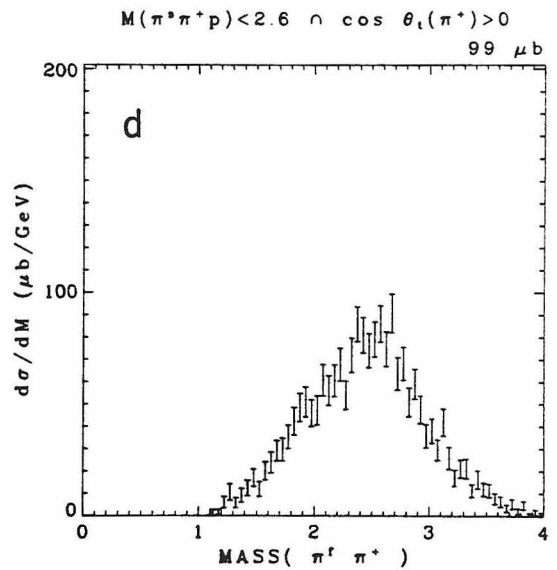
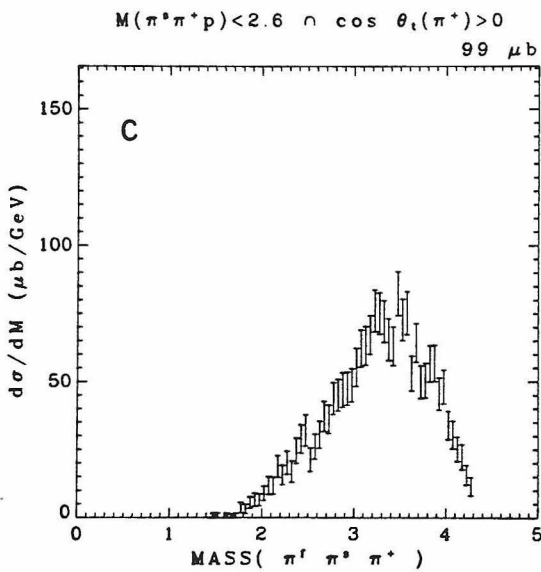
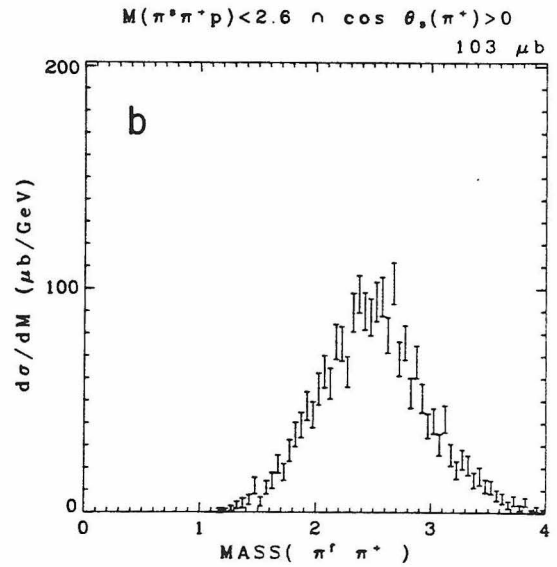
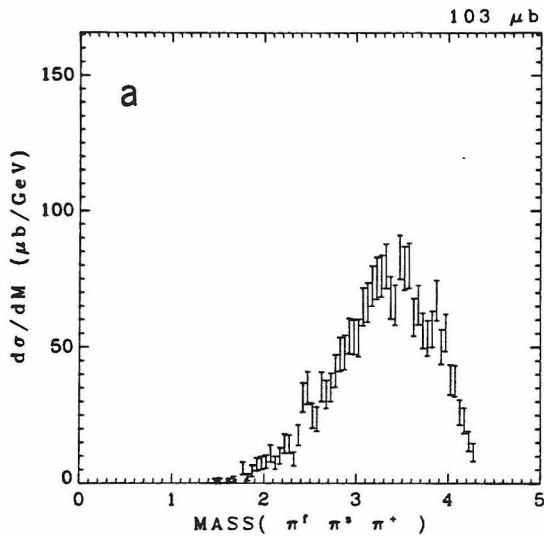
Our check of the helicity conservation hypotheses is for the resonance and background amplitudes in combination. We follow the

suggestions of Cohen-Tannoudji et al. [1970] and of Białas et al. [1971] who demonstrate that helicity conservation implies azimuthal symmetry in the corresponding reference frame for any analyzer of the  $\pi^S \pi^+ p$  system.

Our first concern is that samples on which we carry out the analysis should be free of enhancements in the  $\pi^f \pi^S \pi^+$  and  $\pi^f \pi^+$  combinations. We consider two methods for suppressing this background. One is selection of the  $\Delta$  subset which we discussed in Section IV.7. An alternative invokes cuts on the angles  $\cos \theta_S(\pi^+)$  and  $\cos \theta_t(\pi^+)$ , the polar angles of the  $\pi^+$  in the s-channel and t-channel reference frames (Figures 24c and 24d). The requirement  $\cos \theta_S(\pi^+) > 0$ , by forcing a large angle between the  $\pi^f$  and the  $\pi^+$ , suppresses events with low  $\pi^f \pi^+$  mass. Since the angle of rotation from the s-channel to the t-channel frame is typically small, the cut  $\cos \theta_t(\pi^+) > 0$  has a similar effect. In Figures 29 a-d we show the  $\pi^f \pi^S \pi^+$  and  $\pi^f \pi^+$  mass distributions after these selections and in Figures 30a and b the  $\pi^S \pi^+ p$  mass distributions.

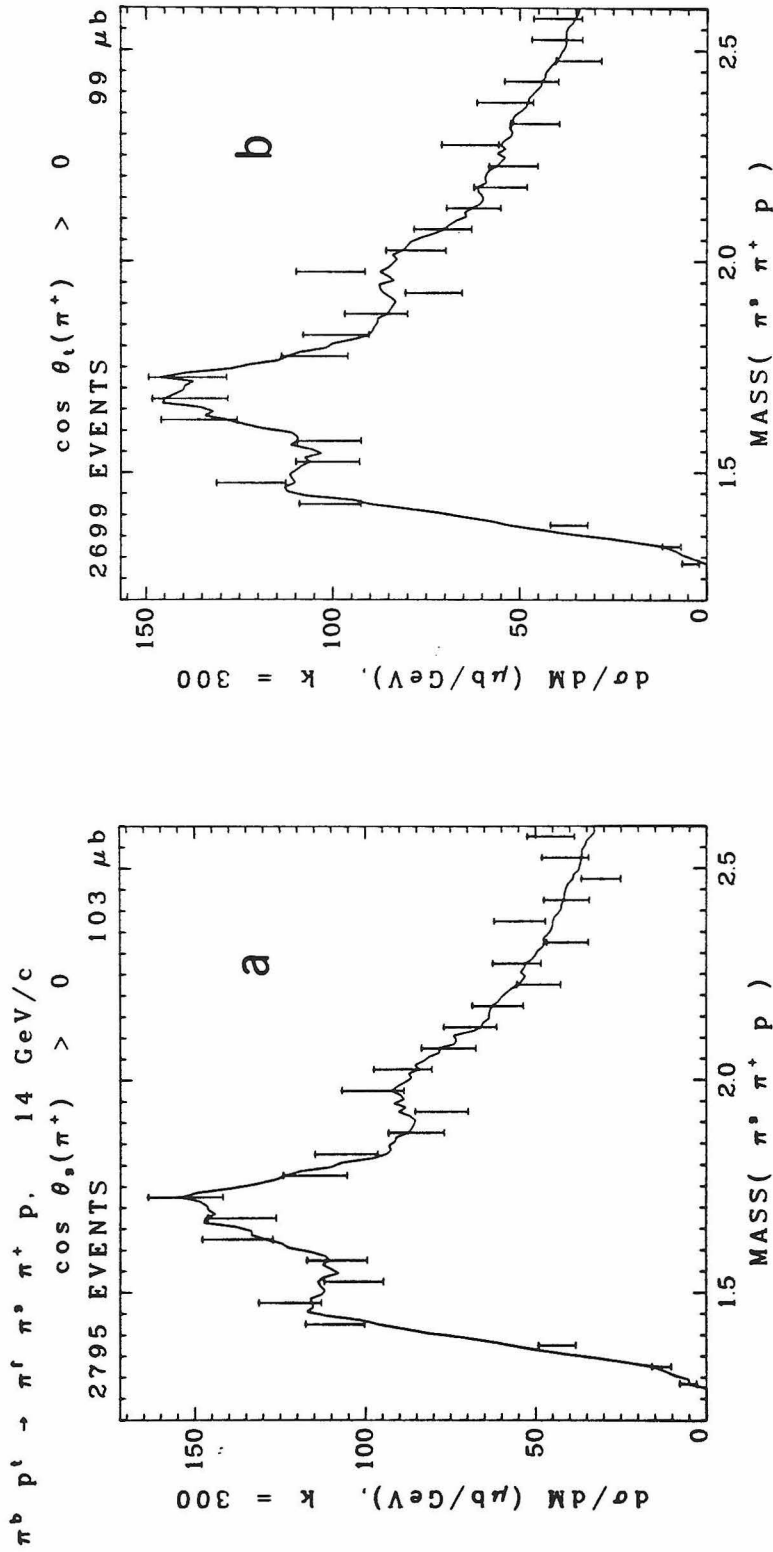
The analyzers which we have employed are the directions of the  $\Delta^{++}$  (equivalent to  $-\vec{P}_S$ ), the proton, the  $\pi^+$ , and the decay plane normal (DPN),  $\vec{P}_p \times \vec{P}_{\pi^+}$ . For the first three of these analyzers parity invariance implies that the distribution function is symmetric under reflection in the production plane or equivalently that the  $\phi$  distribution is an even function on the domain  $(-\pi, \pi)$ . Therefore a test for uniformity of the distribution of  $|\phi|$  in lieu of  $\phi$  is satisfactory and has the advantage of greater statistical power. For

$\pi^b p^t \rightarrow \pi^f \pi^s \pi^+ p$ , 14 GeV/c  
 $M(\pi^s \pi^+ p) < 2.6 \cap \cos \theta_s(\pi^+) > 0$



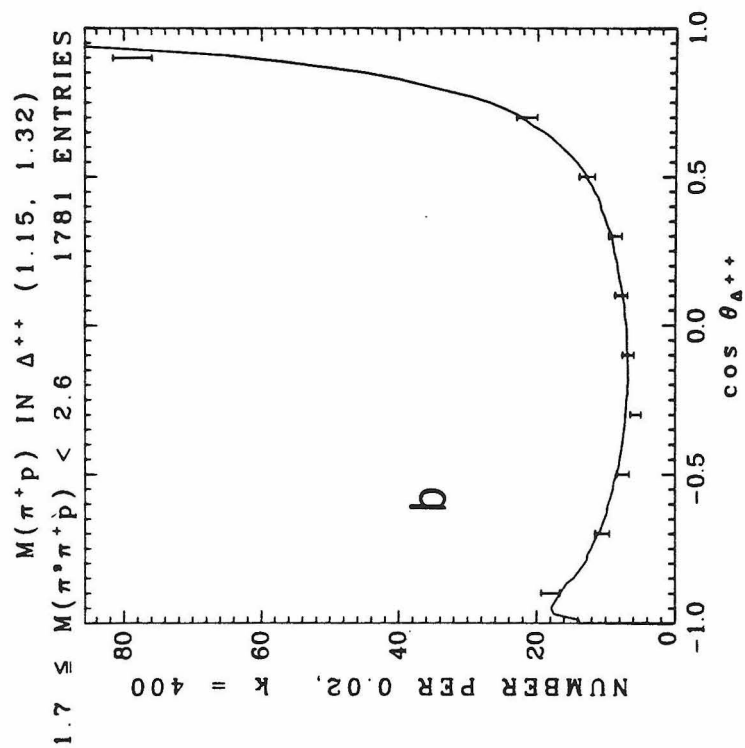
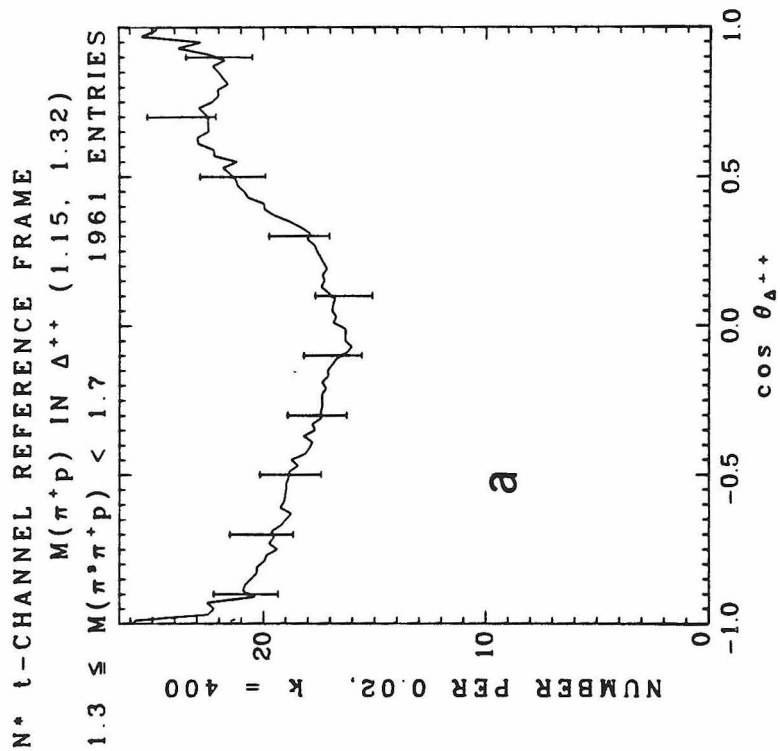
XBL 772-7590

FIG. 29. The cuts on  $\cos \theta_s(\pi^+)$ , a) and b), and on  $\cos \theta_t(\pi^+)$ , c) and d), eliminate A,  $\rho^0$ , and f signals in meson systems which include the  $\pi^f$ . These cuts are suitable for use with tests of helicity conservation. Comparison with Figs. 17 and 18 may be helpful.



XBL 774-8358

FIG. 30. Distributions of the  $N^*$  mass after cuts on a)  $\cos \theta_s(\pi^+)$  and b)  $\cos \theta_t(\pi^+)$ . These samples are free of  $A, \rho^0$ , and  $f$  background and are suitable for tests of helicity conservation. Comparison with Fig. 22 may be helpful.



XBL 774-8357

FIG. 31. Distribution of  $\cos \theta_{\Delta^{++}}$  for a) lower and b) upper intervals of the  $N^*$  mass. Definition of the reference frame appears in Fig. 8d.

the DPN which is an axial vector we test the angle  $|\phi - \pi/2|$  because the symmetry plane is perpendicular to the production plane. Our measure of uniformity for a sample of the data is the Kuiper statistic which we describe in Appendix B.

We have examined  $\phi$  distributions for 0.1 GeV intervals of the  $N^*$  mass, but we can best document our results using just two intervals, 1.3-1.7 GeV and 1.7-2.6 GeV. The prime distinction between these intervals is the  $t$ -channel distribution of  $\cos \theta_{\Delta^{++}}$  which we display in Figures 31 a and b. We ascribe the prominent forward peak which appears in the upper mass interval to the Deck mechanism.<sup>†</sup> Events in the backward hemisphere may be ascribable to processes distinct from the Deck mechanism such as resonance production. By subdividing the upper mass interval into three bins of  $\cos \theta_{\Delta^{++}}$  we will try to assess the validity of sCHC and tCHC separately for the forward and backward processes.

<sup>†</sup>One might naively write for the square of the invariant amplitude corresponding to Figure

$$|M|^2 \propto \frac{G(t_2)}{t_2 - m_\pi^2} \sigma_{\pi\pi}(s_1, t_1) \quad (9.1)$$

where  $\sigma_{\pi\pi}$  is the  $\pi\pi$  elastic scattering cross section and  $G(t_2)$  is a "phenomenological" pion form factor. Resnick [1966] and others have argued, supposing asymptotic beam momentum and  $G(t_2) \approx 1$ , that the amplitude  $M$  generates a uniform distribution in the variable  $\cos \theta_{\Delta^{++}}$ . In reality our beam energy, 14 GeV, is low enough that the  $\pi\pi$  sub-energy,  $s_1$ , may be below the asymptotic regime of  $\sigma_{\pi\pi}$ . The assumption that  $G(t_2) \approx 1$  may also be inappropriate because the description of two body  $\pi$  exchange reactions requires some modification of the Born term to suppress low partial waves. Alternatives are absorption (see Kane and Seidl [1976]) or a form factor which falls rapidly with  $t_2$ . The Deck mechanism is thus a viable explanation of the forward peak in  $\cos \theta_{\Delta^{++}}$ , Resnick's result notwithstanding. Supporting the Deck interpretation is our analysis in Section IV.7 of the decay angular distribution of the  $\Delta$  and particularly its dependence on  $t_2$ .

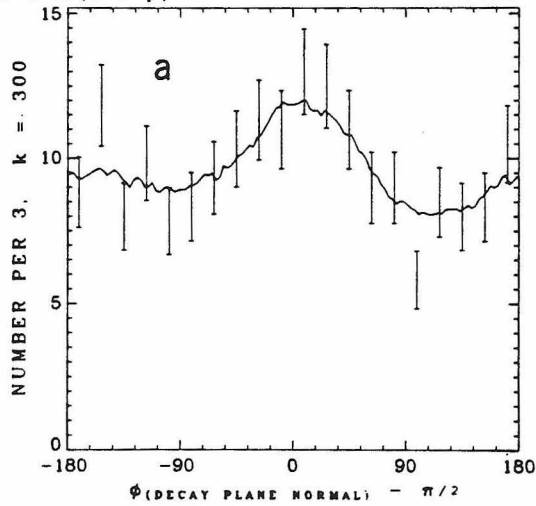
TABLE IV.D.--Acceptability of sCHC and tCHC.

Sample	sCHC	tCHC
<u>Selection by <math>\cos(\pi^+)</math></u>		
$1.3 < M(N^*) < 1.7$	Rejected (Fig. 32a) SS = 1154, ANL = DPN $V = 2.46, CL = 2 \times 10^{-4}$	Accepted (Fig. 32b) SS = 1113, ANL = all ( $\Delta^{++}$ shown) $1.15 \leq V \leq 1.25$ $0.45 \leq CL \leq 0.65$
$1.7 < M(N^*) < 2.6$	Rejected (Fig. 32c) <sub>++</sub> SS = 1636, ANL = $\Delta^{++}$ $V = 7.18, CL \approx 10^{-42}$	Rejected (Fig. 32d) <sub>++</sub> SS = 1582, ANL = $\Delta^{++}$ $V = 2.71, CL = 2 \times 10^{-5}$
<u>Selection by <math>M(\pi^+p)</math> (<math>\Delta</math> subset)</u>		
$1.3 < M(N^*) < 1.7$	Rejected (Fig. 32e) SS = 1961, ANL = p $V = 3.58, CL \approx 10^{-9}$	Marginal SS = 1961, ANL = $\Delta^{++}$ $V = 2.11, CL = 0.004$
$1.3 < M(N^*) < 1.7$ $0.4 < \cos \theta_{\Delta} < 1.0$		Rejected (Fig. 32f) <sub>++</sub> SS = 671, ANL = $\Delta^{++}$ $V = 2.59, CL = 7 \times 10^{-5}$
$1.7 < M(N^*) < 2.6$ $0.4 < \cos \theta_{\Delta} < 1.0$	Rejected (Fig. 32g) <sub>++</sub> SS = 1081, ANL = $\Delta^{++}$ $V = 11.4, CL \approx 10^{-109}$	Rejected (Fig. 32h) <sub>++</sub> SS = 1131, ANL = $\Delta^{++}$ $V = 3.63, CL \approx 10^{-9}$
$1.7 < M(N^*) < 2.6$ $-0.4 < \cos \theta_{\Delta} < 0.4$	Rejected (Fig. 32i) <sub>++</sub> SS = 371, ANL = $\Delta^{++}$ $V = 2.75, CL = 1 \times 10^{-5}$	Accepted (Fig. 32j) <sub>++</sub> SS = 290, ANL = $\Delta^{++}$ $V = 0.98, CL = 0.82$
$1.7 < M(N^*) < 2.6$ $-1.0 < \cos \theta_{\Delta} < -0.4$	Rejected (Fig. 32k) <sub>++</sub> SS = 329, ANL = $\Delta^{++}$ $V = 3.39, CL \approx 10^{-8}$	Marginal (Fig. 32l) <sub>++</sub> SS = 360, ANL = $\Delta^{++}$ $V = 2.00, CL = 0.009$

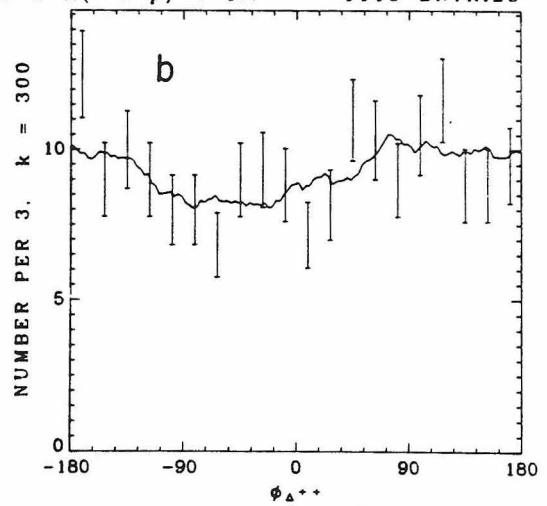
TABLE IV.D. (Continued)

Legend: Units of  $M(N^*)$  are GeV. The symbols  $\theta(\pi^+)$  and  $\theta_\Delta$  refer to s-channel polar angles for the sCHC columns and to t-channel polar angles for the tCHC column.  $SS \equiv$  sample size,  $ANL \equiv$  analyzer,  $V \equiv$  Kuiper statistic,  $CL \equiv$  confidence level for Kuiper statistic. The appellations "accepted", "marginal", and "rejected" correspond to ranges of  $CL$ ,  $0.01 < CL$ ,  $0.001 < CL < 0.01$ , and  $CL < 0.001$  respectively.

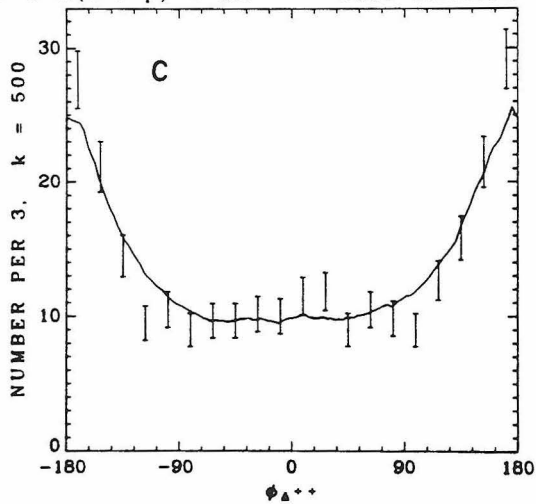
N° s-CHANNEL REFERENCE FRAME  
 $\cos \theta_{\pi^+} > 0$   
 $1.3 \leq M(\pi^+\pi^+p) < 1.7$  1154 ENTRIES



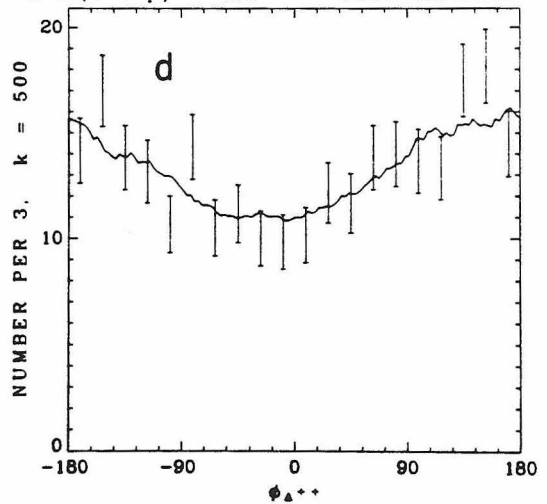
N° t-CHANNEL REFERENCE FRAME  
 $\cos \theta_{\pi^+} > 0$   
 $1.3 \leq M(\pi^+\pi^+p) < 1.7$  1113 ENTRIES



N° s-CHANNEL REFERENCE FRAME  
 $\cos \theta_{\pi^+} > 0$   
 $1.7 \leq M(\pi^+\pi^+p) < 2.6$  1636 ENTRIES



N° t-CHANNEL REFERENCE FRAME  
 $\cos \theta_{\pi^+} > 0$   
 $1.7 \leq M(\pi^+\pi^+p) < 2.6$  1582 ENTRIES



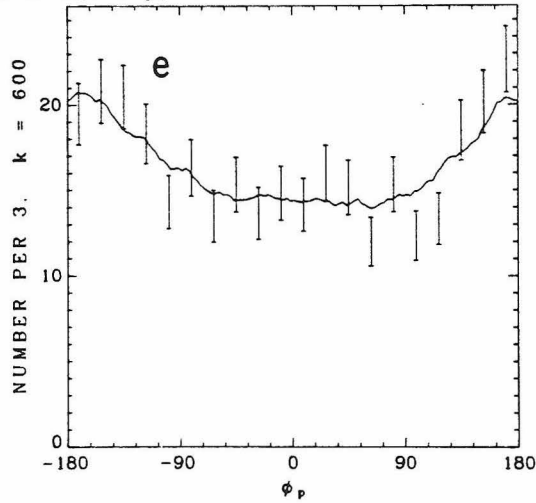
XBL 774-8373

FIG. 32. Azimuthal distributions which demonstrate violation of sCHC (left column) and tCHC (right column). Associated statistics appear in Table IV.D.

N° s-CHANNEL REFERENCE FRAME

$M(\pi^+p)$  IN  $\Delta^{++}$  (1.15, 1.32)

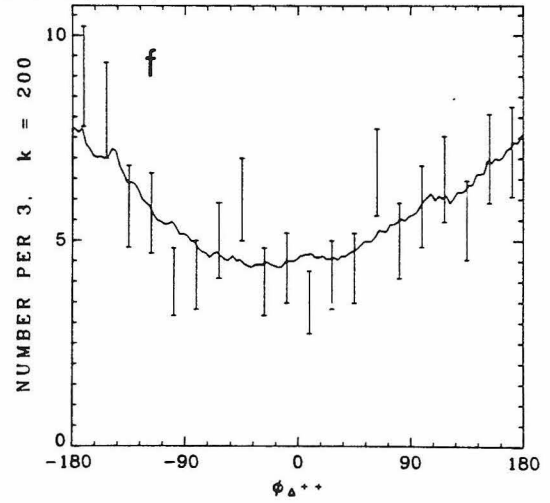
$1.3 \leq M(\pi^+\pi^+p) < 1.7$  1961 ENTRIES



N° t-CHANNEL REFERENCE FRAME

$\Delta^{++}$  REQUIRED,  $0.4 < \cos \theta_{\Delta} < 1.0$

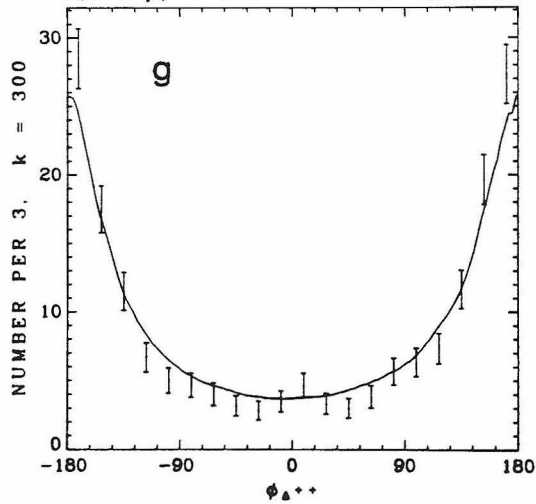
$1.3 \leq M(\pi^+\pi^+p) < 1.7$  671 ENTRIES



N° s-CHANNEL REFERENCE FRAME

$\Delta^{++}$  REQUIRED,  $0.4 < \cos \theta_{\Delta} < 1.0$

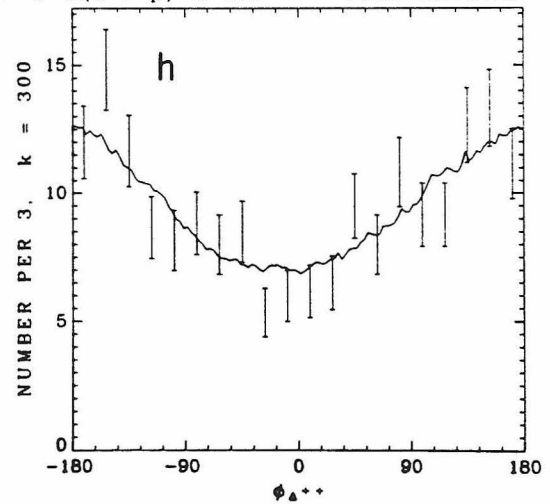
$1.7 \leq M(\pi^+\pi^+p) < 2.6$  1081 ENTRIES



N° t-CHANNEL REFERENCE FRAME

$\Delta^{++}$  REQUIRED,  $0.4 < \cos \theta_{\Delta} < 1.0$

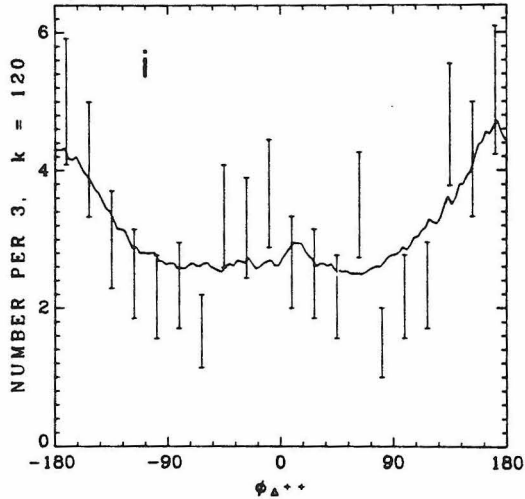
$1.7 \leq M(\pi^+\pi^+p) < 2.6$  1131 ENTRIES



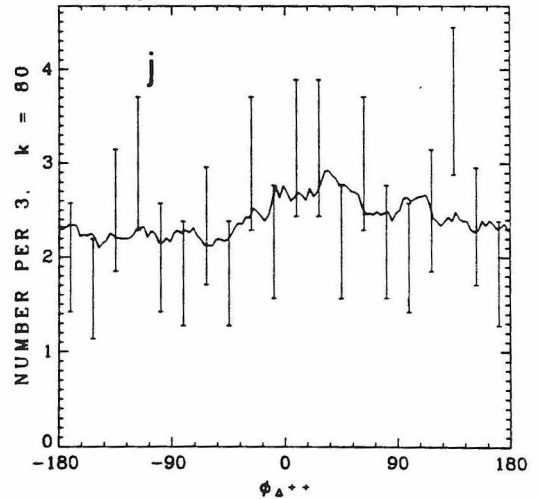
XBL 774-8374

FIG. 32 (continued).

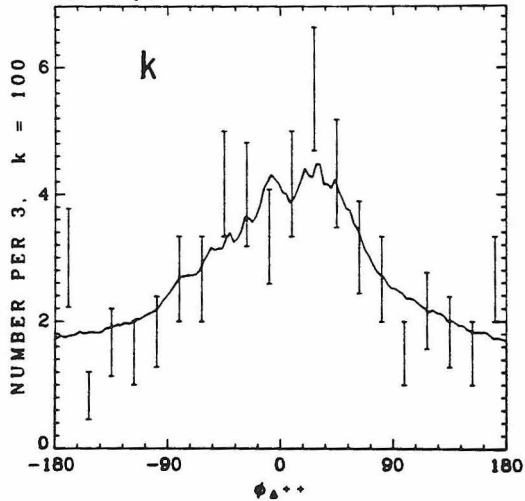
N° s-CHANNEL REFERENCE FRAME  
 $\Delta^{++}$  REQUIRED,  $-0.4 < \cos \theta_{\Delta} < 0.4$   
 $1.7 \leq M(\pi^+\pi^+p) < 2.6$  371 ENTRIES



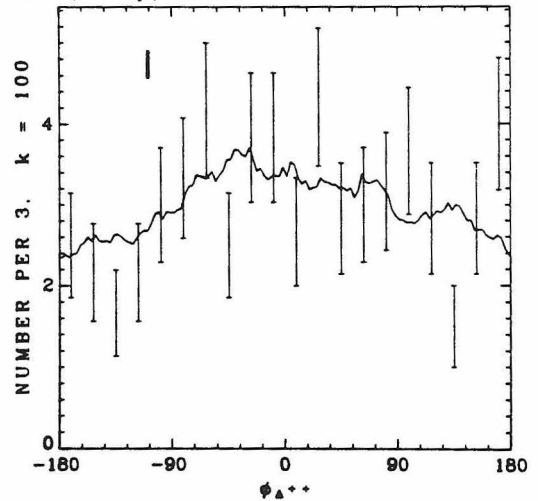
N° t-CHANNEL REFERENCE FRAME  
 $\Delta^{++}$  REQUIRED,  $-0.4 < \cos \theta_{\Delta} < 0.4$   
 $1.7 \leq M(\pi^+\pi^+p) < 2.6$  290 ENTRIES



N° s-CHANNEL REFERENCE FRAME  
 $\Delta^{++}$  REQUIRED,  $-1.0 < \cos \theta_{\Delta} < -0.4$   
 $1.7 \leq M(\pi^+\pi^+p) < 2.6$  329 ENTRIES



N° t-CHANNEL REFERENCE FRAME  
 $\Delta^{++}$  REQUIRED,  $-1.0 < \cos \theta_{\Delta} < -0.4$   
 $1.7 \leq M(\pi^+\pi^+p) < 2.6$  360 ENTRIES



XBL 774-8375

FIG. 32 (continued).

We present our findings in Table IV.D. The analyzer selected for each entry is the one which exhibits the greatest nonuniformity. We observe that the most potent analyzer in this sense is usually but not universally the  $\Delta^{++}$ . sCHC is solidly inconsistent with the data in both mass intervals and throughout the domain of  $\cos \theta_{\Delta}$ . tCHC is also generally inconsistent although it fares much better than sCHC. We attach minimal significance to its acceptability for the lower mass interval of the  $\cos \theta(\pi^+)$  selected sample because we find unambiguous rejection for this mass interval of the  $\Delta$  subset.

The events in the forward peak of Figure 31 b certainly imply violation of tCHC. This finding is consistent with a Deck interpretation of the forward peak since rigorous tCHC is not a property of a typical Deck model. (tCHC may be a good approximation as discussed in Donohue [1971].) Events in the backward direction of Figure 31b ( $\cos \theta_{\Delta} < -0.4$ ) suggest violation of tCHC in this regime also, but the confidence level is not low enough to permit a definitive statement.

#### 10. Test of the Białas-Dabkowski-Van Hove Hypothesis

Gribov [1967] and Morrison [1968] proposed that diffractively produced states satisfy the relation

$$\eta_f/\eta_i = (-1)^{J_f - J_i} \quad (10.1)$$

$\eta_i$  and  $\eta_f$  are the parities of one projectile and the system into which it dissociates, and  $J_i$  and  $J_f$  are the corresponding spins. For the reactions

$$\left\{ \begin{array}{c} \pi \\ K \end{array} \right\} N \rightarrow A^* N \quad (10.2)$$

the "G-M rule" states that the  $J^P$  of the  $A^*$  is a member of the unnatural parity series  $0^-, 1^+, 2^- \dots$ . Theoretical arguments supporting the rule are weak, and the experimental situation is, so far, unfavorable. The most significant evidence against the rule is the persistence out to 40 GeV of the  $A_2(J^P = 2^+)$  production cross section [Antipov et al. 1973]. Applied to nucleon diffraction,

$$\pi N \rightarrow \pi N^* \quad (10.3)$$

the rule states that the  $J^P$  of the  $N^*$  is a member of the series  $1/2^+, 3/2^-, 5/2^+ \dots$ . As with helicity conservation, the rule could be valid for resonant parts of the amplitude but invalid for the background.

In pursuit of tests of relation (10.1) we deal with the sequential process

$$\begin{array}{c} \pi^- p \rightarrow \pi^- N^* \\ \quad \quad \quad \downarrow \\ \quad \quad \quad \pi^- \Delta^{++}(1230) \\ \quad \quad \quad \quad \quad \quad \downarrow \\ \quad \quad \quad \quad \quad \quad \pi^+ p \end{array} \quad (10.4)$$

We characterize each event by the direction of the  $\Delta^{++}$ ,  $\Omega_\Delta \equiv (\theta_\Delta, \phi_\Delta)$ , in the  $N^*$  t-channel frame, Figure 24d, and the direction of the proton,  $\Omega_p \equiv (\theta_p, \phi_p)$ , in the  $\Delta^{++}$  secondary decay frame, Figure 24b. In

terms of these angles and the Wigner D functions [Edmonds 1957] we define the following averages over the data.

$$G_{3/2\ 3/2}^{LM} = \langle D_{MO}^L(\phi_\Delta, \theta_\Delta, 0) \left[ \frac{1}{4} - \frac{5}{4} D_{00}^2(\phi_p, \theta_p, 0) \right] \rangle \quad (10.5)$$

$$G_{1/2\ 1/2}^{LM} = \langle D_{MO}^L(\Omega_\Delta) \left[ \frac{1}{4} + \frac{5}{4} D_{00}^2(\Omega_p) \right] \rangle \quad (10.6)$$

$$G_{3/2\ 1/2}^{LM} = \langle \frac{5\sqrt{2}}{4} D_{M1}^L(\Omega_\Delta) D_{10}^2(\Omega_p) \rangle \quad (10.7)$$

$$G_{3/2-1/2}^{LM} = \langle -\frac{5\sqrt{2}}{4} D_{M2}^L(\Omega_\Delta) D_{20}^2(\Omega_p) \rangle \quad (10.8)$$

Parity conservation at every step of the process (10.4) implies that the imaginary parts of the G's are zero except for sampling fluctuation.

Biačyas, Dabkowski, and Van Hove [1971] derived some relations among these G's by assuming validity of both the G-M rule and helicity conservation. We will refer to their ansatz as the BDVH hypothesis. Two of the five relations are

$$G_{\lambda\lambda}^{LM} = 0 \quad \text{if } M \neq 0 \quad (10.9)$$

$$G_{\lambda\lambda}^{L0} = 0 \quad \text{if } L \geq 2J \quad (10.10)$$

We use  $J$  to represent the maximum spin contribution to the  $N^*$  system. Equation (10.9) follows from helicity conservation whether or not the G-M rule holds. The other three relations we state separately for each of three assumptions about  $J$ .

$$J = 3/2: \quad G_{3/2 \ 3/2}^{00} + 5 G_{3/2 \ 3/2}^{20} = 0 \quad (10.11)$$

$$G_{3/2 \ 3/2}^{10} = 0 \quad (10.12)$$

$$G_{3/2 \ 1/2}^{20} + G_{3/2-1/2}^{20} = 0 \quad (10.13)$$

$$J = 5/2: \quad G_{3/2 \ 3/2}^{00} + 5 G_{3/2 \ 3/2}^{20} + 9 G_{3/2 \ 3/2}^{40} = 0 \quad (10.14)$$

$$3 G_{3/2 \ 3/2}^{10} + 7 G_{3/2 \ 3/2}^{30} = 0 \quad (10.15)$$

$$G_{3/2 \ 1/2}^{40} + \sqrt{2} G_{3/2-1/2}^{40} = 0 \quad (10.16)$$

$$J = 7/2: \quad G_{3/2 \ 3/2}^{00} + 5 G_{3/2 \ 3/2}^{20} + 9 G_{3/2 \ 3/2}^{40} + 13 G_{3/2 \ 3/2}^{60} = 0 \quad (10.17)$$

$$3 G_{3/2 \ 3/2}^{10} + 7 G_{3/2 \ 3/2}^{30} + 11 G_{3/2 \ 3/2}^{50} = 0 \quad (10.18)$$

$$2 G_{3/2 \ 1/2}^{60} + \sqrt{10} G_{3/2-1/2}^{60} = 0 \quad (10.19)$$

In Appendix E we give an independent derivation of these relations.

Białas et al. give us the opportunity to test the G-M rule with either sCHC or tCHC. In the previous section we demonstrate violation of sCHC so gross that further use of the hypothesis would be unreasonable. The violation of tCHC, while statistically strong, is by comparison a small effect. Although we have shown that tCHC is imperfect, still it may be a legitimate approximation.

The event sample on which we test the BDVH hypothesis is the  $\Delta$  subset which we defined at the outset of Section IV.7. A  $\pi^+ p$  mass

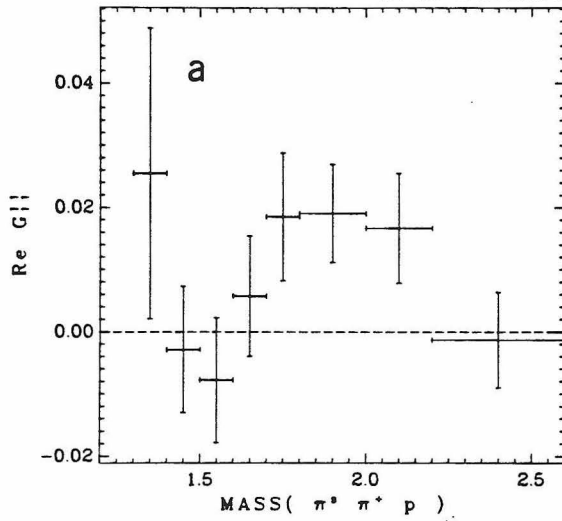
cut is of course insufficient to guarantee that the spin of the  $\pi^+p$  system is  $3/2$ . We did give evidence in Section IV.7 favorable to dominance of spin  $3/2$  even for low  $N^*$  mass. We do not know, however, what impact on the  $G$  moments we should expect from small  $1/2^+$  and  $1/2^-$  waves. This "contamination" could create apparent violation if BDVH were exact, or it could mask violation if BDVH were just approximate. Consequently our test is sensitive only to gross failure of the hypothesis. We have calculated  $G$ 's for eight intervals of  $M(N^*)$ , but in order to maintain adequate sample sizes we have not subdivided in the variable  $t(\pi^b \rightarrow \pi^f)$ . If BDVH is valid for the entire range of  $|t|$  ( $0.01$  to  $0.5 \text{ GeV}^2$ ) the appropriate moments will be zero whether or not we weight the events. We have elected not to weight and so to obtain slightly smaller errors.

In Figure 33a-d we display the moments  $\text{Re } G_{1/2}^{L1}$  for  $1 \leq L \leq 4$ . These moments test only tCHC. The violation of tCHC which we demonstrated in the previous section shows up in the intervals covering  $1.7$  to  $2.2 \text{ GeV}$ . The departures from zero are of three to four standard deviations. If the  $M = 0$  moments are no more inconsistent with zero than these  $M = 1$  moments, they will contribute no additional information on the BDVH hypothesis.

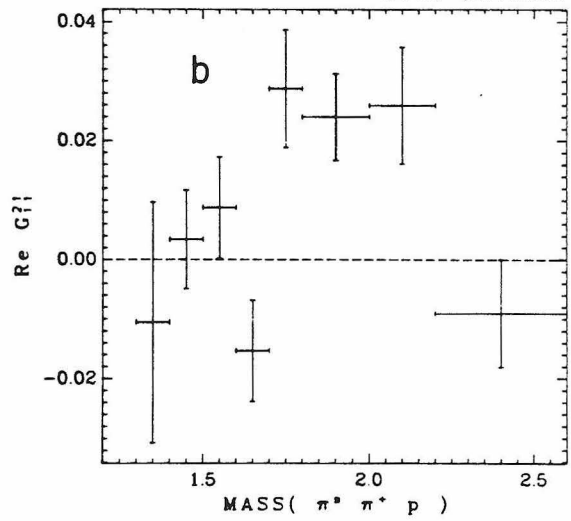
In Figure 34 we show the  $M = 0$  moments of lowest  $L$  which must be zero if BDVH is valid and  $J = 7/2$ . From Figures 34c and 34d we conclude that BDVH fails above  $2.0 \text{ GeV}$  unless  $N^*$  spins of  $9/2$  or greater contribute. In any case spin  $7/2$  must contribute above  $2.0 \text{ GeV}$  to generate nonzero  $L = 7$  moments. Figures 34e-g show that

N<sup>+</sup> t-CHANNEL MOMENTSM( $\pi^+p$ ) IN  $\Delta^{++}$  (1.15, 1.32)

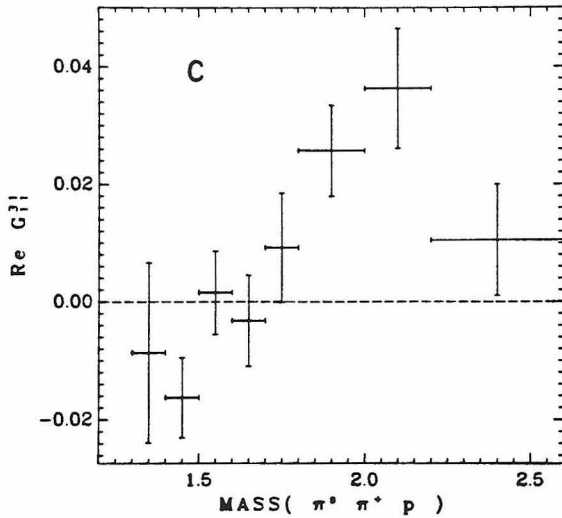
3742 ENTRIES

M( $\pi^+p$ ) IN  $\Delta^{++}$  (1.15, 1.32)

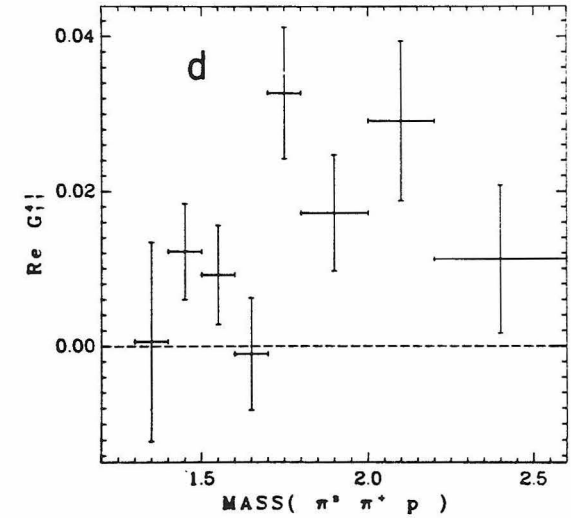
3742 ENTRIES

M( $\pi^+p$ ) IN  $\Delta^{++}$  (1.15, 1.32)

3742 ENTRIES

M( $\pi^+p$ ) IN  $\Delta^{++}$  (1.15, 1.32)

3742 ENTRIES



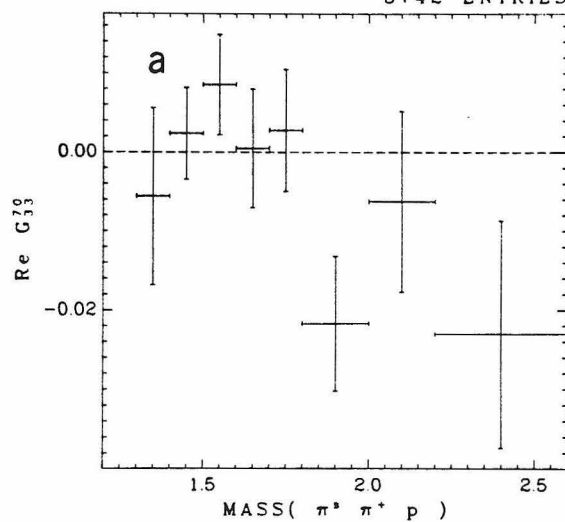
XBL 774-8364

FIG. 33. The moments  $G_{1/2}^{L1}$  for values of  $L$  from 1 to 4.

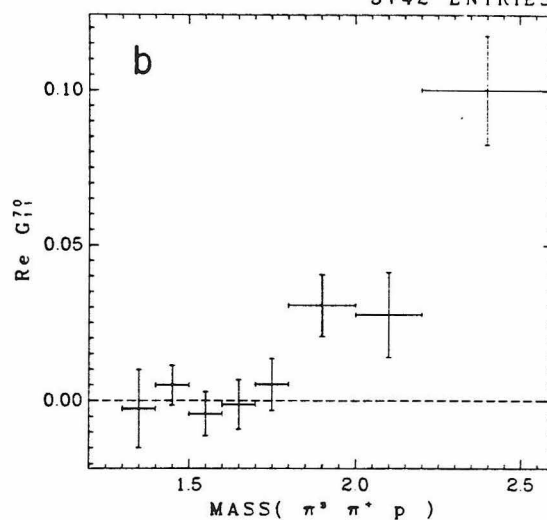
N\* t-CHANNEL MOMENTS

M( $\pi^+p$ ) IN  $\Delta^{++}$  (1.15, 1.32)

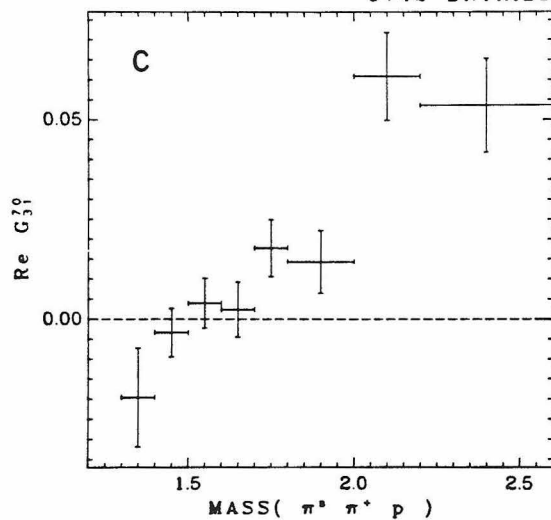
3742 ENTRIES

M( $\pi^+p$ ) IN  $\Delta^{++}$  (1.15, 1.32)

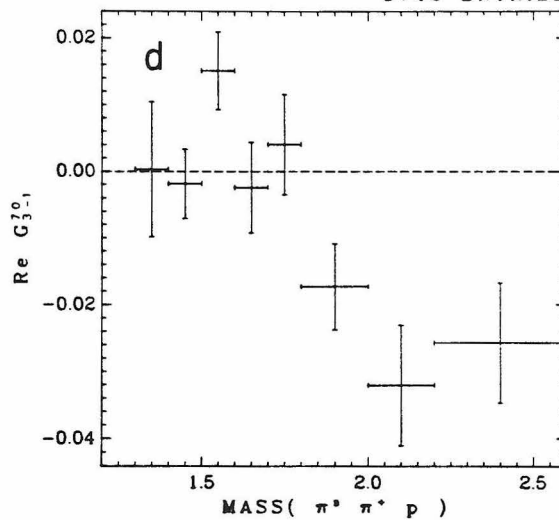
3742 ENTRIES

M( $\pi^+p$ ) IN  $\Delta^{++}$  (1.15, 1.32)

3742 ENTRIES

M( $\pi^+p$ ) IN  $\Delta^{++}$  (1.15, 1.32)

3742 ENTRIES



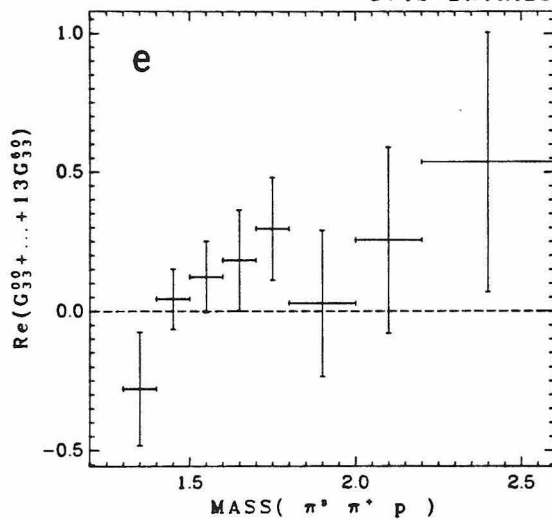
XBL 774-8366

FIG. 34. G moments which the BDVH hypothesis requires to be zero if the spin of the  $N^* \leq 7/2$ . Subscripts 3, 1, and -1 in the y axis label should be understood as 3/2, 1/2, and -1/2.

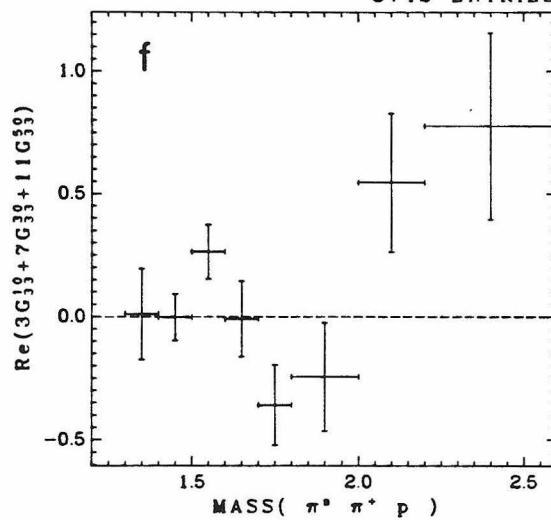
N° t-CHANNEL MOMENTS

M( $\pi^+p$ ) IN  $\Delta^{++}$  (1.15, 1.32)

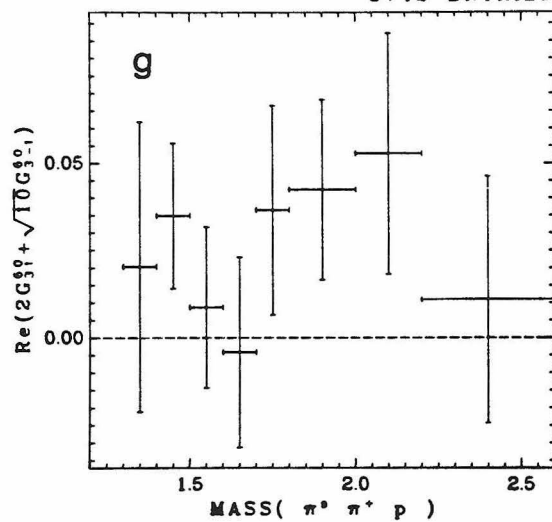
3742 ENTRIES

M( $\pi^+p$ ) IN  $\Delta^{++}$  (1.15, 1.32)

3742 ENTRIES

M( $\pi^+p$ ) IN  $\Delta^{++}$  (1.15, 1.32)

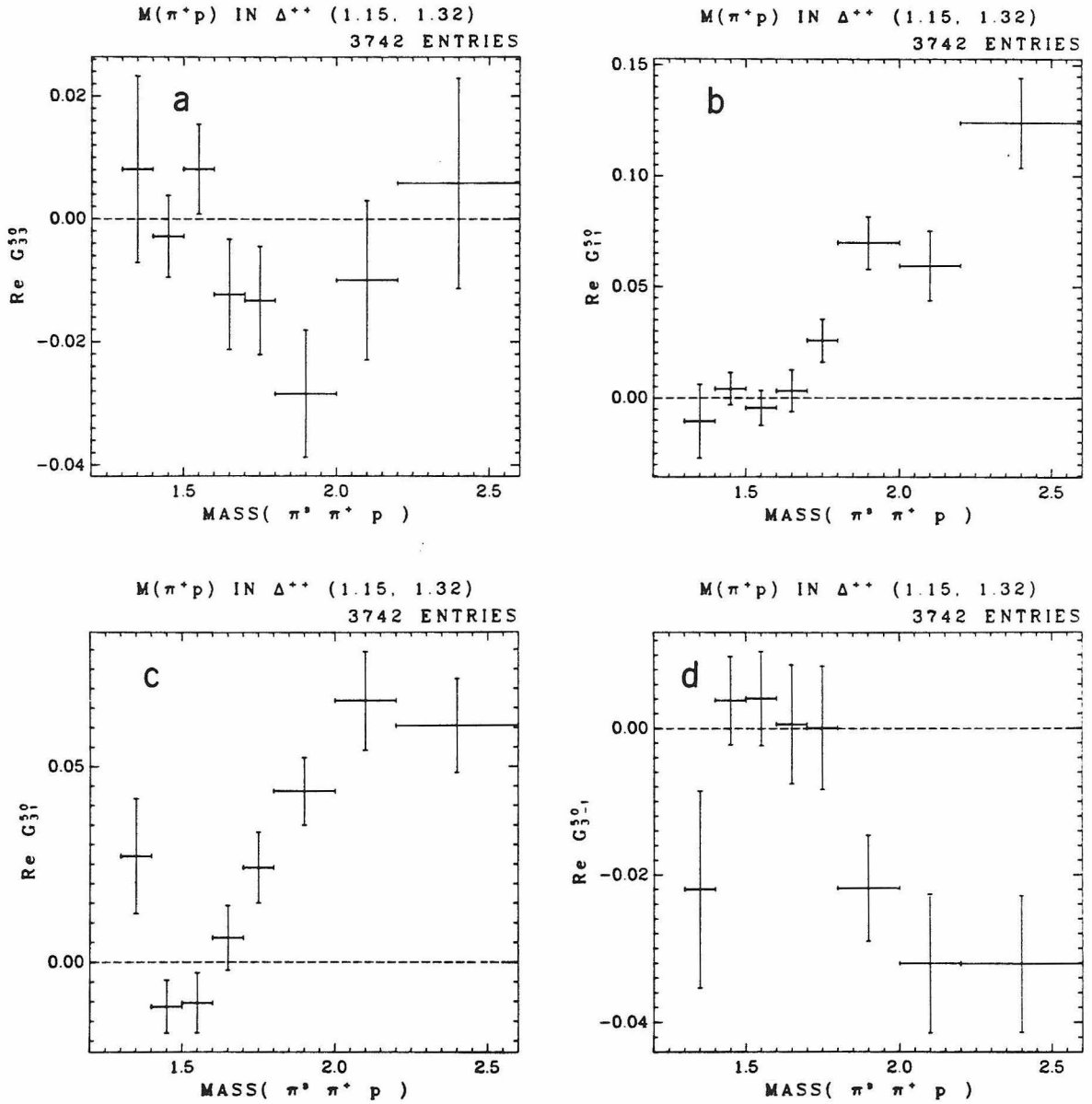
3742 ENTRIES



XBL 774-8367

FIG. 34 (continued).

$N^*$  t-CHANNEL MOMENTS



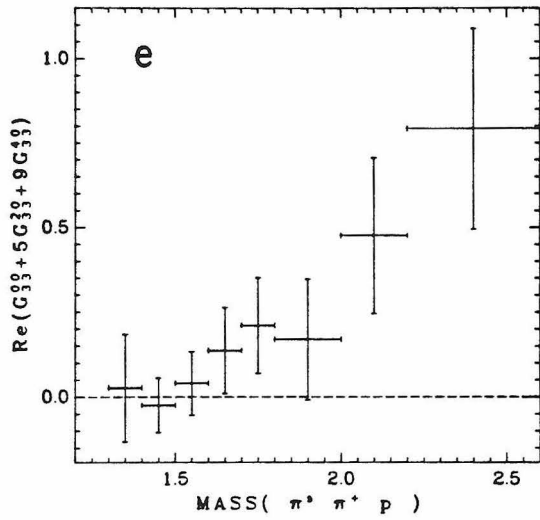
XBL 774-8368

FIG. 35. G moments which the BDVH hypothesis requires to be zero zero if the spin of the  $N^* \leq 5/2$ . Subscripts 3, 1, and -1 in the the y axis label should be understood as 3/2, 1/2, and -1/2.

N° t-CHANNEL MOMENTS

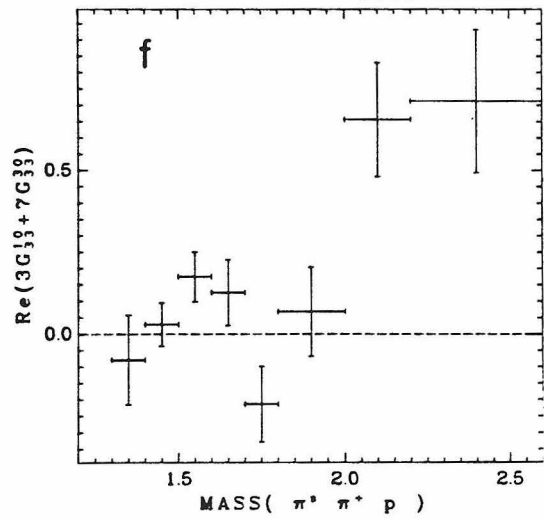
M( $\pi^+p$ ) IN  $\Delta^{++}$  (1.15, 1.32)

3742 ENTRIES



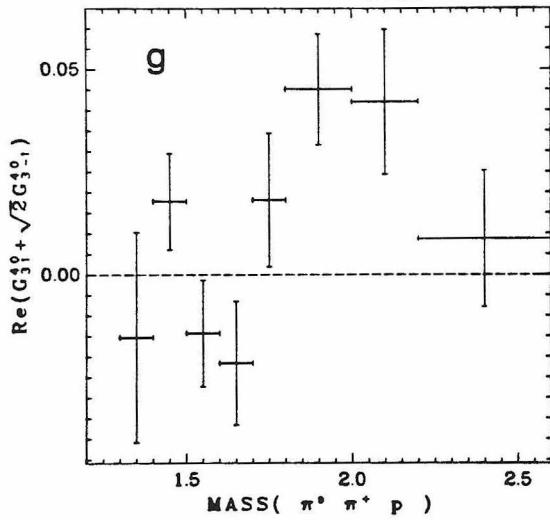
M( $\pi^+p$ ) IN  $\Delta^{++}$  (1.15, 1.32)

3742 ENTRIES



M( $\pi^+p$ ) IN  $\Delta^{++}$  (1.15, 1.32)

3742 ENTRIES



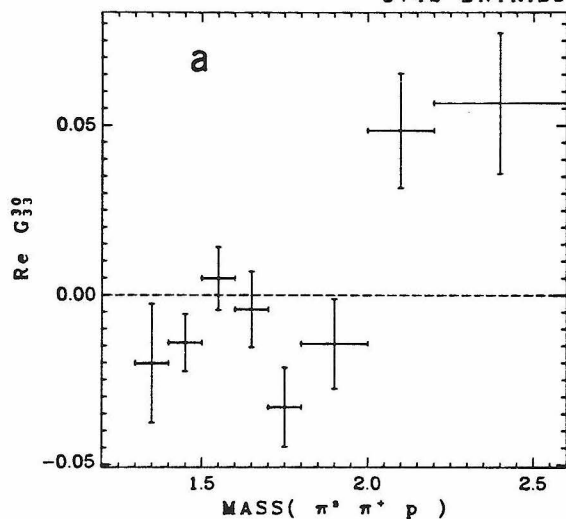
XBL 774-8369

FIG. 35 (continued).

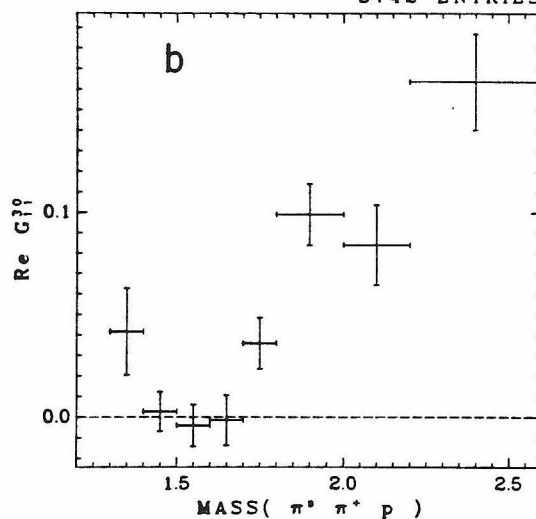
N\* t-CHANNEL MOMENTS

M( $\pi^+p$ ) IN  $\Delta^{++}$  (1.15, 1.32)

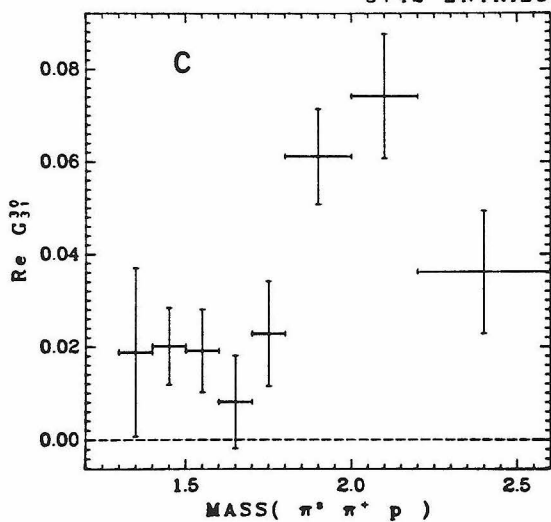
3742 ENTRIES

M( $\pi^+p$ ) IN  $\Delta^{++}$  (1.15, 1.32)

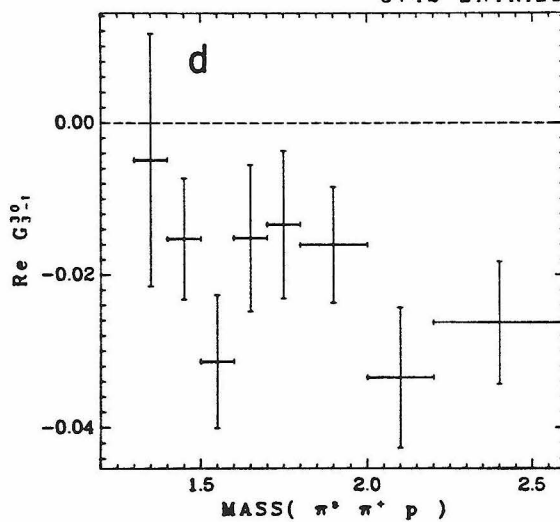
3742 ENTRIES

M( $\pi^+p$ ) IN  $\Delta^{++}$  (1.15, 1.32)

3742 ENTRIES

M( $\pi^+p$ ) IN  $\Delta^{++}$  (1.15, 1.32)

3742 ENTRIES



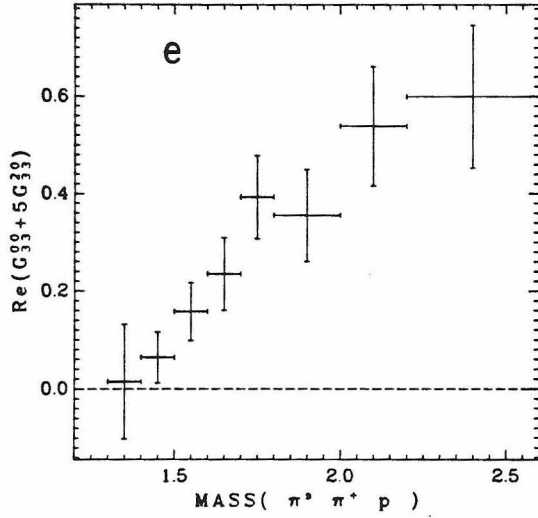
XBL 774-8371

FIG. 36. G moments which the BDVH hypothesis requires to be zero if the spin of the  $N^* \leq 3/2$ . Subscripts 3, 1, and -1 in the y axis label should be understood as  $3/2$ ,  $1/2$ , and  $-1/2$ .

N\* t-CHANNEL MOMENTS

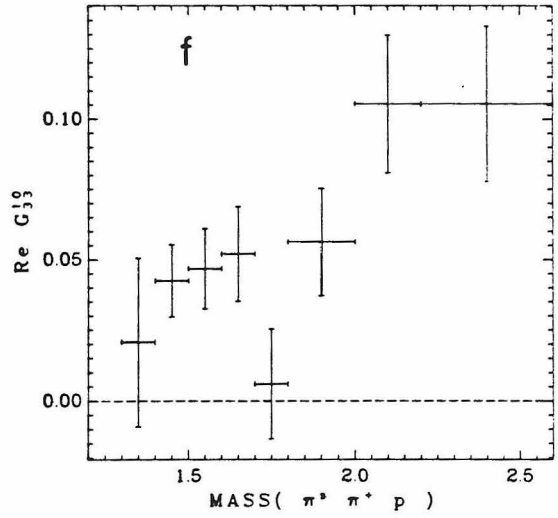
M( $\pi^+p$ ) IN  $\Delta^{++}$  (1.15, 1.32)

3742 ENTRIES



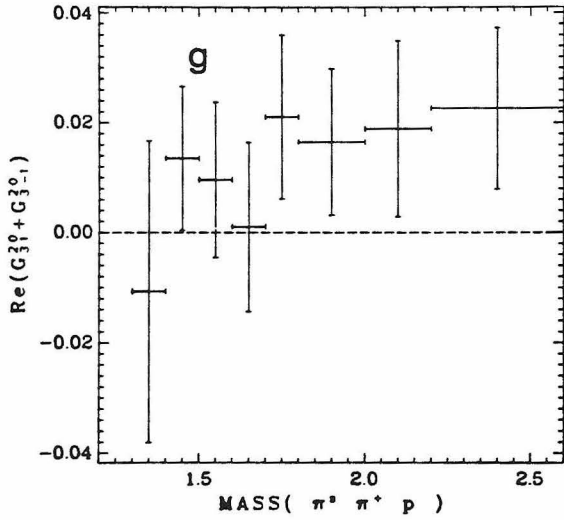
M( $\pi^+p$ ) IN  $\Delta^{++}$  (1.15, 1.32)

3742 ENTRIES



M( $\pi^+p$ ) IN  $\Delta^{++}$  (1.15, 1.32)

3742 ENTRIES



XBL 774-8372

FIG. 36 (continued).

below 2.0 GeV the data are consistent with the relations (10.17)-(10.19). Figures 35 and 36 show the moments of lowest  $L$  which BDVH requires to be zero for  $J = 5/2$  and  $J = 3/2$ . Figures 35 a-g indicate that BDVH is compatible with  $J = 5/2$  up to 1.8 GeV. Above 1.8 GeV the moments  $G_{1/2}^{50}$  and  $G_{3/2}^{50}$  (Figures 35 b and c) are dramatically different from zero. With  $J = 3/2$  the data suggest violation of BDVH. Figures 36 e and f are not in good agreement with the relations (10.11) and (10.12) except in the lowest mass interval. Between 1.4 and 1.7 GeV these moments are about  $3\sigma$  from zero.

We displayed in Figure 31b the forward peak which dominates the distribution of  $\cos \theta_{\Delta}$  above  $M(N^*)$  of 1.7 GeV. This peak, probably ascribable to the Deck mechanism, is the source of the large values acquired by the large  $L$  moments. The development of the forward peak is detrimental to our test of the BDVH hypothesis because it obliges us to consider high values of the  $N^*$  spin especially at high mass. Those moments which are far from zero we can attribute to an insufficiently high  $J$  rather than to violation of BDVH. On balance, therefore, our data appear consistent with BDVH.

A previous test of the BDVH hypothesis using the reaction  $pp \rightarrow p\pi^- \Delta^{++}(1230)$  appears in Rushbrooke et al. [1971b]. Their moments disagreed to some extent from expected values, so they could not claim support for BDVH. On the other hand the discrepancies were small enough that they did not rule out BDVH. So far as we can tell, their result and ours are consistent.

## 11. Summary

We have investigated the reaction  $\pi^- p \rightarrow \pi^- N^* \rightarrow \pi^- \pi^- \pi^+ p$  at an incident  $\pi^-$  momentum of 14 GeV/c. After elimination of competing channels our sample size for  $M(N^*) < 2.6$  GeV is about 4400. In the two body mass spectra the only outstanding feature is the  $\Delta^{++}(1230)$  resonance in the  $\pi^+ p$  system. In the  $\pi^+ \pi^- p$  mass spectrum we observe enhancements at 1.49 GeV, 1.72 GeV, and some indication of a peak near 2.0 GeV. For the prominent 1.72 GeV feature we give estimates of the width and cross section, and we give evidence favoring a substantial branching fraction to  $\pi\Delta(1230)$ . We looked for evidence of  $N^*(1470)$  production followed by  $\pi\Delta(1230)$  decay with negative result. An examination of the  $\Delta^{++}(1230)$  decay distribution suggests that the Deck mechanism is the major contributor to the  $\pi\Delta$  subchannel.

We tested the consistency of helicity conservation, both s-channel (sCHC) and t-channel (tCHC). We found that sCHC conflicted strongly with our data. We also observed violation of tCHC which is statistically convincing but is much weaker than the violation of sCHC. These findings are applicable to the amplitude as a whole. The question of whether resonant pieces of the amplitude obey sCHC or tCHC remains open. Finally, we tested for simultaneous validity of tCHC and the Gribov-Morrison rule for spin-parities of diffractively produced systems. We could find no significant contradiction with this dual hypothesis.

## Appendix A

## Details of the Trigger Program

At the conclusion of a beam pulse a computer code executing in the Sigma 2 performed the following sequence of operations.

1. Transfer z axis spark coordinates and some scintillation counter information from external electronics to the computer memory. The time required was about 0.6 msec.
2. By the counts from a scintillation detector just upstream of the bubble chamber, verify that the beam intensity was neither too low (zero counts) nor too high (more than 11 counts). Pulses with unacceptable intensity were ignored.
3. Determine if a spark chamber trigger had occurred. On pulses with no SC trigger the only action taken was to tally counts from various scintillation detectors.
4. On the occasion of a SC trigger, reorganize the digitizations from each wand into four ordered lists associated with each of the four stations. Remove adjacent chamber redundancies from these lists.

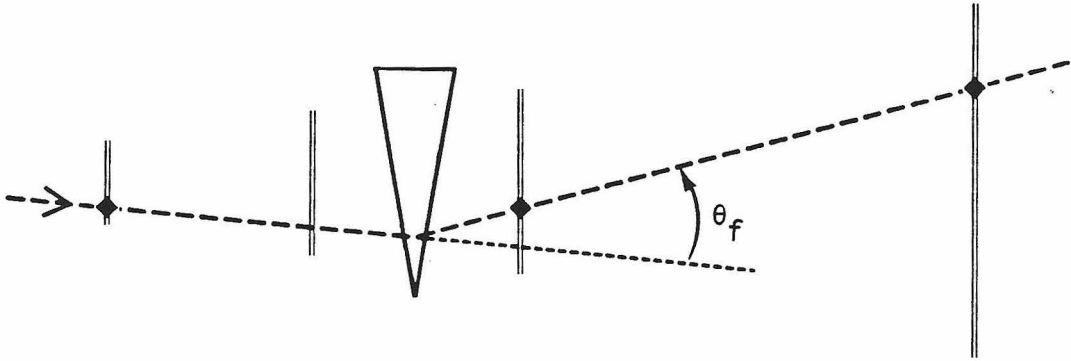


FIG. 37. A triplet of sparks at stations 1, 3, and 4 determines a trajectory through the spectrometer.

5. Search for a triplet of sparks at stations 1, 3, and 4 as in Figure 37 which satisfy the inequality

$$M_L^2 < M_p^2 + 2 M_p P_0 \theta_0 \left( \frac{1}{\theta_b} - \frac{1}{\theta_f} \right) < M_U^2. \quad (\text{A.1})$$

This inequality incorporates only the first term of Equation (II.5.10).  $M_L$  and  $M_U$  are the lower and upper limits selected for  $M_x$ . For the majority of the data  $M_L = 1.1$  GeV and  $M_U = 3.8$  GeV.

6. Locate a station 2 spark on the trajectory determined by the spark triplet selected in step 5.
7. Require that the trajectory intersect the portion of the bubble

chamber illuminated by the beam,

8. Require that the spark triplet from step 5 satisfy

$$M_L^2 < M_p^2 + 2 M_p P_0 \theta_0 \left( \frac{1}{\theta_b} - \frac{1}{\theta_f} \right) - P_f C_z \phi_z^2 < M_U^2 . \quad (\text{A.2})$$

This inequality includes the second term of equation (II.5.10).

9. In case of success in steps 5-8 permit the bubble chamber camera to expose the film 3 msec after the beam pulse.

When steps 6, 7, or 8 failed, the program returned to step 5.

When step 5 failed, the program advanced to step 10.

10. Transfer y axis spark coordinates from external electronics to the computer memory, and record all of the data on magnetic tape.

## The Kuiper Statistic

The Kuiper statistic [Kuiper 1960] is useful for testing the goodness-of-fit of a simple hypothesis (no free parameters) to a sample from a univariate density. It is a close relative to the Kolmogorov statistic. In this appendix we give its definition and basic properties, and we say qualitatively when this statistic may be preferable to various alternatives.

Given a continuous probability density  $f(x)$  and a sample from the population  $g(x)$ , we seek to test the (null) hypothesis  $g(x) \equiv f(x)$ . We define the cumulative distribution function (c.d.f.)  $F(x)$  by

$$F(x) = \int_{-\infty}^x f(t)dt \quad (\text{B.1})$$

We order the sample from  $g$  so that

$$x_i < x_{i+1}, \quad i = 1, 2, \dots, n-1 \quad (\text{B.2})$$

and define the sample c.d.f. by the relation

$$G(x) = \begin{cases} 0 & x < x_1 \\ i/n & x_i < x < x_{i+1} \\ 1 & x > x_n \end{cases} \quad (\text{B.3})$$

The Kuiper statistic is

$$V = \sqrt{n} [\text{Max} (F(x) - G(x)) + \text{Max} (G(x) - F(x))] \quad (\text{B.4})$$

The use of this statistic is the same as for most other test statistics; if  $V$  exceeds some threshold,  $\tau$  (nominally determined in advance of calculation of  $V$ ), we reject the hypothesis. If on the other hand,  $V < \tau$ , it may still be that  $g(x) \neq f(x)$ , but then we require more data to distinguish them. The Kuiper statistic has the property that if  $g(x) \neq f(x)$ , the probability that  $V < \tau$  drops to zero as  $n \rightarrow \infty$ . We say that  $V$  is consistent against every alternative. It also has the property that the distribution of  $V$  when  $g(x) \equiv f(x)$  is independent of  $f(x)$ , and on this account we say that  $V$  is "distribution-free". Its distribution for large  $n$ , the asymptotic distribution, although difficult to derive, is easy to state and easy to use for computations. The formulae are

$$\tau'^2 = \tau^2 + \frac{2}{3\sqrt{n}} \tau \quad (\text{B.5})$$

$$1 - P(V > \tau) = \sum_{k=-\infty}^{\infty} (1 - 4k^2 \tau'^2) \exp(-2k^2 \tau'^2) \quad (\text{B.6})$$

$$= \frac{\pi^2 \sqrt{2\pi}}{\tau'^3} \sum_{k=1}^{\infty} k^2 \exp \left[ -\frac{\pi^2 k^2}{2\tau'^2} \right] \quad (\text{B.7})^\dagger$$

<sup>†</sup>For one method of establishing the equivalence of the forms (B.6) and (B.7) see Whittaker and Watson, A Course of Modern Analysis, Chap. 6, exercises 17 and 18.

If relation (B.6) is used when  $\tau^2 > 1.5$  and relation (B.7) when  $\tau^2 < 1.5$ , the error incurred by truncating terms with  $|k| > 1$  is less than 0.05% of the smaller of  $P$  and  $1-P$ . These formulae give  $P$  correct to about 0.03 even for  $n$  as low as 10.

Procedures for assessing goodness-of-fit fall into three general categories. These are tests based on moments, the  $\chi^2$  test, and tests in the Kolmogorov family. The most powerful procedures are by and large in the first category. When the null hypothesis is false, they reject it with the greatest efficiency. These tests are never consistent against every alternative, but such strong consistency is usually a lesser virtue. The principal disadvantage of moments tests is that they are not robust; they are hypersensitive to a small number of outliers in the sample. They are "too powerful" in that they detect departures from the null hypothesis which are of little interest to the experimenter.

Though less powerful, the tests of the Kolmogorov family are highly robust as is  $\chi^2$ , provided that the bins have approximately equal probability content. Of the robust tests, the best choice will depend on what kind of alternatives are a priori most probable. We distinguish two classes, "high frequency" deviations, such as oscillations or spikes, and "low frequency" deviations such as arise from shift in location or change of scale. In the former case a  $\chi^2$  test with an appropriate number of bins is more powerful than the Kuiper test. In the latter case  $\chi^2$  is less powerful regardless of the number of bins used. A heuristic explanation for  $\chi^2$ 's inferiority against low

frequency alternatives is that it sacrifices the information contained in the relative positions of the bins. The better known Kolmogorov test is slightly more powerful than Kuiper against shift in location, but against change of scale it is much worse even than  $\chi^2$ . The Cramer-von Mises statistics and variations are mostly less powerful than Kuiper. Any that are better offer only marginal improvement, and the substantial increase in computational complexity makes them unattractive.

The limitation to simple hypotheses and univariate densities which applies to the Kuiper test does not apply to  $\chi^2$ . The Kuiper test is therefore applicable to a much narrower class of problems. For many of the problems to which it is applicable, however, it has the greater power and is the better choice.

## Appendix C

The  $\chi^2$  Dependence of Contamination  
from Lower Constraint Classes

Our purpose in this appendix is to justify the use of relation (IV.3.7). We recall that each event is a point in a 15 dimensional measurement space, that 1C events lie in a 14 dimensional hypersurface, and that 4C events lie in an 11 dimensional hypersurface (see Section III.7). The 4C  $\chi^2$  is the square of the distance of an event from the 4C hypersurface using the appropriate metric. We will assume that the 4C surface is entirely embedded in the 1C surface. From the standpoint of 1C contamination in the 4C sample this situation is the worst possible. In fact the surfaces do not even intersect, but exchanging identities of the positive tracks creates a reflection of the 1C surface which does intersect. Furthermore about 20% of the 4C events have a low  $\chi^2$  for the "inverted" 1C fit which is an indication that the 4C surface and the reflected 1C surface are nearly parallel. We represent this situation schematically in Figure 38. Consequently our embedding assumption is as conservative as it can be but not more conservative than it needs to be.

Our next assumption is that the constant and gradient terms alone of a Taylor expansion suffice to describe the density of 1C events at points near the 4C surface. By thus ruling out the possibility that the 1C density peaks at the 4C surface we have built in our

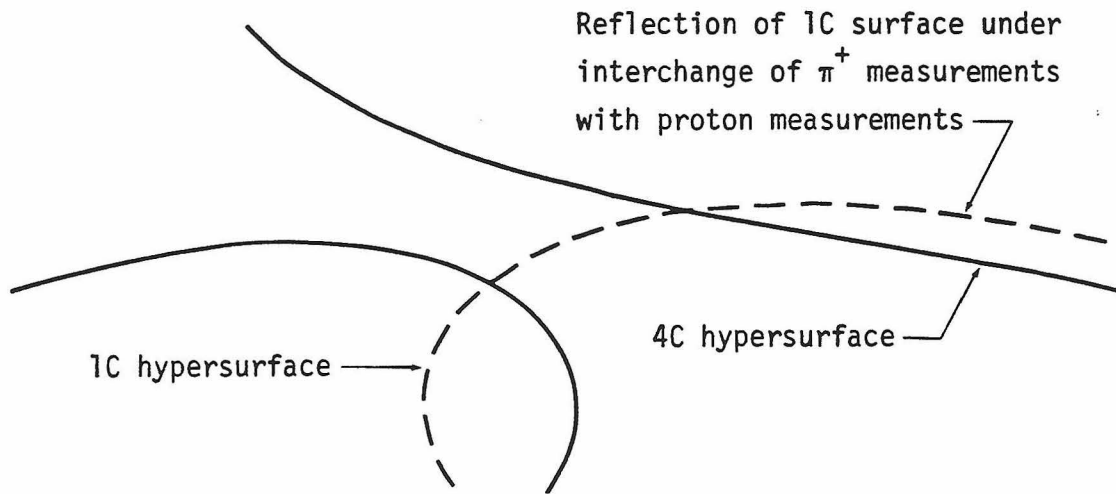


FIG. 38. Schematic of 4C and 1C hypersurfaces.

"anti-conspiracy" bias. Next we define a sheath at distance  $r$  to be the 14 dimensional locus of points at a distance  $r$  from the 4C surface. Points within the sheath have a  $\chi^2 < r^2$ . What we want to determine is the  $r$  dependence of the number of 1C points within the sheath. To obtain this we integrate in the 1C surface as far as the sheath using the Taylor expansion approximation. The result is the product of the 1C density at the 4C surface (technically averaged over the 4C surface) and the "area" of enclosed 1C surface. This area is proportional to  $r^3$  which follows purely from dimensional counting. These same arguments applied to 0C events imply contamination within the sheath proportional to  $r^4$ . The  $r^3$  dependence is the more conservative and is the one we use in relation (IV.3.7).

## Appendix D

## Estimation of the Probability of Track Inversion

We consider the set of events which are truly examples of the reaction  $\pi^- p \rightarrow \pi^- \pi^- \pi^+ p$ . To each such event we fit two hypotheses,  $H_T$ , the correct one, and  $H_F$ , the one with inverted assignment of masses to the positive tracks. From our fits we obtain the  $\chi^2$  statistics and the frequency statistics

$$Q_T \equiv P(\chi^2 > \chi_T^2), \quad Q_F \equiv P(\chi^2 > \chi_F^2). \quad (D.1)$$

In this appendix we address the following question. If to each event we assign the hypothesis corresponding to the larger of  $Q_T$  and  $Q_F$ , how often do we assign  $H_F$ ?

We let the probability densities of  $Q_T$  and  $Q_F$  be respectively  $t(x)$  and  $f(x)$ . We note that these densities are not observable. We also define the statistics

$$Q_G = \max(Q_T, Q_F)$$

and

$$Q_L = \min(Q_T, Q_F) \quad (D.2)$$

with observable density functions  $g(x)$  and  $\ell(x)$ . If we have used quantitatively correct procedures for the computation of  $\chi^2$ , then  $t(x)$  is uniform on the domain  $(0,1)$ . We will assume this property for our analysis. Since  $t(x)$  is not observable we do not have a direct check

of this assumption. In the usual case, however, that assignments of  $H_F$  are quite infrequent, the observable counterpart,  $g(x)$ , is similar to  $t(x)$  and we can use it to decide whether  $t(x)$  is sufficiently flat.

Whereas errors of measurement completely determine the shape of  $t(x)$ , they play a comparatively minor role in creating the shape of  $f(x)$ . In the space of measured parameters (see Section III.7) each event has a reflection under the interchange  $\pi^+ \leftrightarrow p$ . Kinematics determines the separation of an event from its reflection. The distribution of  $Q_F$  thus depends primarily on the density of perfectly measured events in the 4C hypersurface, a density determined by the scattering amplitude.

We next consider the joint probability density of  $Q_T$  and  $Q_F$ ,  $H(x,y)$ .

$$\begin{aligned} t(x) &= \int_0^1 H(x,y) dy \\ f(y) &= \int_0^1 H(x,y) dx \end{aligned} \quad (D.3)$$

For our analysis we wish to assume that

$$H(x,y) = t(x)f(y) . \quad (D.4)$$

This assumption is not quite valid because the multiple scattering and digitization errors which are common to the two  $Q$  statistics compromise their independence. As a practical matter, however, we expect that the simplification embodied in equation (D.4) is so benign that our result will still

be a useful approximation.

We evaluate the proportion of assignments of  $H_F$  in terms of  $H(x,y)$  by integration over the triangle,  $y > x$ , which we show horizontally hatched in Figure 39.

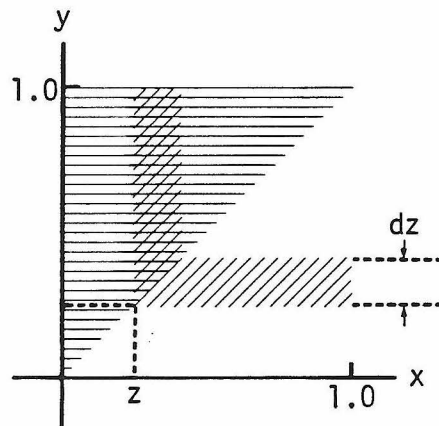


FIG. 39. Integration regions in the domain of  $H(x,y)$  for  $P(H_F)$  and  $\ell(z)$ .

$$\begin{aligned}
 P(H_F) &= \int_0^1 dy \int_0^y dx H(x,y) \\
 &= \int_0^1 dy f(y) \int_0^y t(x) dx \\
 &= \int_0^1 yf(y) dy \tag{D.5}
 \end{aligned}$$

The observable counterpart of  $f(x)$  is  $\ell(x)$  which we evaluate in terms of  $H(x,y)$  by integrating over the slant hatched portion of Figure 39.

$$\begin{aligned} \ell(z) &= \int_z^1 H(x,z) dx + \int_z^1 H(z,y) dy \\ &= (1-z)f(z) + \int_z^1 f(y) dy \end{aligned} \quad (D.6)$$

Differentiating, we obtain a first order differential equation for  $f(z)$ .

$$(1-z)f'(z) - 2f(z) = \ell'(z) \quad (D.7)$$

This equation has the general solution

$$f(z) = \frac{-1}{(1-z)^2} \int_z^1 (1-u)\ell'(u) du + \frac{\kappa}{(1-z)^2} \quad (D.8)$$

Applying l'Hospital's rule to the first term of equation (D.8) we learn that

$$f(1) = -\frac{1}{2} \ell'(1) + \lim_{z \rightarrow 1} \frac{\kappa}{(1-z)^2} \quad (D.9)$$

In any practical situation  $f(1)$  is finite and  $\ell'(1)$  is finite which implies that  $\kappa = 0$ . Next we integrate by parts in equation (D.8) obtaining

$$\begin{aligned} f(z) &= \frac{1}{(1-z)^2} \left[ (1-u)(u) \Big|_z^1 - \int_{1-z}^0 \ell(u) d(1-u) \right] \\ &= \frac{\ell(z)}{(1-z)} - \frac{1}{(1-z)^2} \int_z^1 \ell(u) du \end{aligned} \quad (D.10)$$

Using this expression for  $f(z)$  we evaluate the integral in equation (D.5).

$$P(H_F) = \int_0^1 \frac{z}{1-y} \ell(y) dy - \int_0^1 \left( \int_y^1 \ell(z) dz \right) \frac{y dy}{(1-y)^2} \quad (D.11)$$

We make the substitutions

$$\begin{aligned} u &= \int_y^1 \ell(z) dz & du &= -\ell(y) dy \\ v &= \ln(1-y) + \frac{1}{1-y} & dv &= \frac{y dy}{(1-y)^2} \end{aligned} \quad (D.12)$$

and again integrate by parts.

$$\begin{aligned} P(H_F) &= \int_0^1 \frac{y}{1-y} \ell(y) dy - uv \Big|_0^1 + \int_0^1 v du \\ &= \int_0^1 \frac{1}{1-y} \ell(y) dy - \lim_{y \rightarrow 1} (uv) + 1 + \int_0^1 [\ln(1-y) + \frac{1}{1-y}] [-\ell(y)] dy \\ &= \int_0^1 [-\ln(1-y)] \ell(y) dy - \lim_{y \rightarrow 1} (uv) \end{aligned}$$

$$\lim_{y \rightarrow 1} u = \lim_{y \rightarrow 1} \lambda'(1)(1-y)^2$$

$$\begin{aligned} \lim_{y \rightarrow 1} (uv) &= \lambda'(1) \left[ \lim_{y \rightarrow 1} (1-y)^2 \lambda n(1-y) + \lim_{y \rightarrow 1} (1-y) \right] \\ &= 0 \end{aligned}$$

$$P(H_F) = \int_0^1 [-\lambda n(1-y)] \lambda(y) dy \quad (D.13)$$

The integral is just the average value of the bracketed expression with respect to the distribution of  $Q_L$ . Thus to estimate  $P(H_F)$  from a sample of  $N$  events we compute

$$P(H_F) \approx \frac{1}{N} \sum_{\text{events}} [-\lambda n(1-Q_L)] \quad (D.14)$$

This statistic is the one we quote in Section IV.3 for the rate of misassignments ascribable to reaction (IV.3.6).



which  $N_T$  has helicity  $\tau$ . This amplitude depends on  $s$ , the square of the CM energy, on  $t$ , the square momentum transfer from  $A_i$  to  $A_f$ , and on  $M$ , the mass of the  $N^*$ . We will carry out the derivation supposing these three parameters fixed, and our results will be testable with any binning of the data in  $t$  and  $M$ . Henceforth we will allow these dependencies to be implicit when we write  $T$ . Whichever axis figures in the helicity conservation rule is the axis along which we quantize  $\Lambda$ . So long as this axis is in the production plane, as it is for conservation of s- or t-channel helicity, we can write form invariant equations. We may interpret our results according to either conservation hypothesis by measuring  $\Omega_\Delta$  in the appropriate coordinate frame.

The middle factor in equation (E.2) describes the decay of the  $N^*$  to  $\Delta\pi_1$ .  $\Omega_\Delta \equiv (\theta_\Delta, \phi_\Delta)$  is the direction and  $\lambda$  the helicity of the  $\Delta$ . We measure both in the reference frame with  $N^*$  at rest,  $\hat{z}$  along the  $\Lambda$  quantization axis, and  $\hat{y}$  in the direction  $\vec{p}_{A_i} \times \vec{p}_{A_f}$  which is the production plane normal. In Figure 24 d is an illustration of this frame for  $\Lambda$  taken along  $N_T$ . The quantum numbers  $J$ ,  $\Lambda$ , and  $\lambda$  completely determine the dependence of this amplitude on  $\Omega_\Delta$ . Specifically (see Chung, equation (7.3)).

$$(\Omega_\Delta \lambda | M_J | J \Lambda) = N_J F_\lambda^J D_{\Lambda\lambda}^J (\phi_\Delta, \theta_\Delta, 0). \quad (\text{E.3})$$

$N_J$  is a real normalization constant which we have no need to discuss. The Wigner  $D$  functions embody all the rotational symmetry of the state

$J, \Lambda$ , and the helicity amplitudes,  $F_{\lambda}^J$ , embody all of the dynamics of the operator  $M_J$ . The  $F$ 's depend on  $J, \lambda$ , and  $M_{\Delta}$  and may depend also on  $s, t$ , and  $M$ . Our remarks concerning the  $s, t$ , and  $M$  dependence of  $T$  are pertinent also to  $F_{\lambda}^J$ . Likewise we consider  $M_{\Delta}$  fixed for this derivation and bin the data as appropriate when testing the results. The critical assumption concerning  $F$  is that  $\lambda$  is the helicity index of a spin 3/2 system.

The left factor in equation (E.2) describes the decay of the  $\Delta$  to  $N_{\pi_2}$ . For this decay the reference frame has the  $\Delta$  at rest,  $\hat{z}'$  antiparallel to  $\vec{P}_{\pi_1}$ , and  $\hat{y}'$  parallel to  $\hat{z} \times \hat{z}'$ . Figure 24b illustrates the frame which is complementary to Figure 24d. In this frame the  $z'$  component of the  $\Delta$  spin is  $\lambda$  and the  $N$  travels along  $\Omega_N \equiv (\theta_N, \phi_N)$  with helicity  $\nu$ . In precise analogy with equation (E.3)

$$(\Omega_N \nu | M_{\Delta} | \lambda) = N_{\Delta} F_{\nu}^{\Delta} D_{\lambda\nu}^{3/2}(\phi_N, \theta_N, 0). \quad (E.4)$$

Again  $N_{\Delta}$  is a real constant of no concern to us.  $F_{\nu}^{\Delta}$  may depend on  $M_{\Delta}$ , but since we are suppressing this variable, it is for present purposes a complex constant.

The intensity observed from an unpolarized target is

$$I(\Omega_{\Delta}, \Omega_N) = \frac{1}{2} \sum_{\nu\tau} I(\Omega_{\Delta}, \Omega_N; \nu\tau). \quad (E.5)$$

$$\begin{aligned} I(\Omega_{\Delta}, \Omega_N; \nu\tau) &= |M_{\nu\tau}|^2 \\ &= \sum_{\lambda\lambda'} (\Omega_N \nu | M_{\Delta} | \lambda) (\Omega_N \nu | M_{\Delta} | \lambda')^* \rho_{\lambda\lambda'}^{\tau}(\Omega_{\Delta}) \end{aligned} \quad (E.6)$$

$$\rho_{\lambda\lambda'}^{\tau}(\Omega_{\Delta}) = \sum_{\substack{J\Lambda \\ J'\Lambda'}} (\Omega_{\Delta}\lambda|M_J|J\Lambda)(\Omega_{\Delta}\lambda'|M_{J'}|J'\Lambda')^*(J\Lambda|T|\tau)(J'\Lambda'|T|\tau)^* \quad (E.7)$$

Our helicity conservation hypothesis stated in this notation is

$$(J\Lambda|T|\tau) = T_{\tau}^J \delta_{\Lambda,\tau} \quad (E.8)$$

If  $T$  is the sum of a resonance part and a background part, equation (E.8) implies that both parts preserve the target helicity. We could not carry through this derivation with the weaker assumption of helicity conservation only in the resonance part of  $T$ . Equation (E.7) reduces to

$$\rho_{\lambda\lambda'}^{\tau}(\Omega_{\Delta}) = \sum_{J,J'} T_{\tau}^J T_{\tau}^{J'*} (\Omega_{\Delta}\lambda|M_J|J\tau)(\Omega_{\Delta}\lambda'|M_{J'}|J'\tau)^* \quad (E.9)$$

Next we state the implications of parity invariance of the operators  $T$ ,  $M_J$ , and  $M_{\Delta}$ . In what follows  $\eta_Z$  is the intrinsic parity of  $Z$ . The Gribov-Morrison rule permits just one  $N^*$  parity for each  $J$ , so anticipating this restriction we write  $\eta_J$  for the parity of the  $N^*$  of spin  $J$ . For the production amplitude we have

$$\begin{aligned} T_{-\Lambda}^J &= \eta_{A_i} \eta_{N_T} \eta_{A_f} \eta_J (-1)^{J-1/2} (-1)^{\Lambda-\tau} T_{\Lambda}^J \\ &= \eta_J (-1)^{J-1/2} T_{\Lambda}^J \end{aligned} \quad (E.10)$$

which follows directly from equation (11) of Gottfried and Jackson [1964]. We set  $\Lambda\text{-}\tau$  to zero because of the helicity conservation condition, equation (E.8). For the  $N^*$  decay

$$\begin{aligned} F_{-\lambda}^J &= \eta_J \eta_\Delta \eta_\pi (-1)^{J-3/2} F_\lambda^J \\ &= \eta_J (-1)^{J-1/2} F_\lambda^J \end{aligned} \quad (\text{E.11})$$

and for the  $\Delta$  decay

$$\begin{aligned} F_{-\nu}^\Delta &= \eta_\Delta \eta_N \eta_\pi (-1)^{3/2-1/2} F_\nu^\Delta \\ &= F_\nu^\Delta . \end{aligned} \quad (\text{E.12})$$

According to the Gribov-Morrison rule

$$\eta_J / \eta_{N_T} = (-1)^{J-1/2} \quad (\text{E.13})$$

from which

$$\eta_J (-1)^{J-1/2} = 1 . \quad (\text{E.14})$$

Equations (E.10) and (E.11) become

$$T_{-\Lambda}^J = T_\Lambda^J \quad (\text{E.15})$$

and

$$F_{-\lambda}^J = F_\lambda^J . \quad (\text{E.16})$$

Our goal is some relations among certain moments of  $I(\Omega_\Delta, \Omega_N)$ , so we begin to calculate moments. First we define

$$H^{\ell m L M} = \sum_{\nu} H_{\nu}^{\ell m L M} \quad (E.17)$$

$$H_{\nu}^{\ell m L M} = \frac{1}{2} \sum_{\tau} \int \int I(\Omega_\Delta, \Omega_N; \nu \tau) D_{Mm}^L(\phi_\Delta, \theta_\Delta, 0) D_{m0}^{\ell}(\phi_N, \theta_N, 0) d\Omega_N d\Omega_\Delta. \quad (E.18)$$

$H^{\ell m L M}$  is calculable directly from data.

Using equations (E.3), (E.4), (E.6), and (E.9) we break up the r.h.s. of (E.18) as follows.

$$H_{\nu}^{\ell m L M} = \sum_{\lambda \lambda'} Q_{\nu \lambda \lambda'}^{\ell m} R_{\lambda \lambda'}^{m L M} \quad (E.19)$$

$$Q_{\nu \lambda \lambda'}^{\ell m} = N_{\Delta}^2 |F_{\nu}^{\Delta}|^2 \int D_{\lambda \nu}^{3/2*}(\Omega_N) D_{\lambda' \nu}^{3/2}(\Omega_N) D_{m0}^{\ell}(\Omega_N) d\Omega_N \quad (E.20)$$

$$R_{\lambda \lambda'}^{m L M} = \frac{1}{2} \sum_{J J' \tau} N_J N_{J'} F_{\lambda}^{J J'} F_{\lambda'}^{J' J} T_{\tau}^{J J'} T_{\tau}^{J' J} \int D_{\tau \lambda}^{J*}(\Omega_\Delta) D_{\tau \lambda'}^{J'}(\Omega_\Delta) D_{Mm}^L(\Omega_\Delta) d\Omega_\Delta \quad (E.21)$$

The integral of a triple product of D functions (see Edmonds [1957], equation (4.6.2)) over all three Euler angles is

$$\begin{aligned} \Phi(J_1 \mu_1 \nu_1 J_2 \mu_2 \nu_2 J_3 \mu_3 \nu_3) &\equiv \int_0^{2\pi} \int_0^{\pi} \int_0^{2\pi} D_{\mu_1 \nu_1}^{J_1*} D_{\mu_2 \nu_2}^{J_2} D_{\mu_3 \nu_3}^{J_3} d\alpha d(\cos \beta) d\gamma \\ &= (-1)^{\mu_2 - \nu_2} \frac{8\pi^2}{2J_3 + 1} \{J_1 \mu_1 J_2 - \mu_2 | J_3 \mu_3\} \{J_1 \nu_1 J_2 - \nu_2 | J_3 \nu_3\}. \end{aligned} \quad (E.22)$$

The symbol  $\{J_1\mu_1 J_2\mu_2 | J_3\mu_3\}$  is a Clebsch-Gordan coefficient for coupling of  $J_1$  and  $J_2$  to the resultant  $J_3$ . The integral over  $\gamma$  in equation (E.22) contributes only a factor  $2\pi \delta_{\nu_1-\nu_2, \nu_3}$ . When  $\nu_1-\nu_2 = \nu_3$ , the integral of the triple product over only  $\alpha$  and  $\cos \beta$  has the value  $\Phi/2\pi$  at  $\gamma = 0$ . We readily apply this result to equation (E.20).

$$Q_{\nu\lambda\lambda'}^{\ell m} = N_{\Delta}^2 |F_{\nu}^{\Delta}|^2 (-1)^{\lambda'-\nu} \frac{4\pi}{(2\ell+1)} \left\{ \frac{3}{2} \lambda \frac{3}{2} -\lambda' | \ell m \right\} \left\{ \frac{3}{2} \nu \frac{3}{2} -\nu | \ell 0 \right\} \quad (\text{E.23})$$

We can use the same technique to evaluate the integral on the r.h.s. of equation (E.21) when  $m = \lambda - \lambda'$ . We do not care what the value of  $R$  is when  $m \neq \lambda - \lambda'$  because for all such terms in the sum in equation (E.19)  $Q$  is zero.

$$R_{\lambda\lambda'}^{mLM} = (-1)^{-\lambda' - 1/2} \frac{4\pi}{(2L+1)} k_{\lambda\lambda'}^{mLM}, \quad m = \lambda - \lambda' \quad (\text{E.24})$$

$$k_{\lambda\lambda'}^{mLM} = \frac{1}{2} \sum_{JJ'\tau} w_{\lambda\lambda'\tau}^{LJJ'} \quad (\text{E.25})$$

$$w_{\lambda\lambda'\tau}^{LJJ'} = (-1)^{\frac{1}{2} + \tau} N_J N_{J'} F_{\lambda\lambda}^{JJ'} F_{\lambda\lambda}^{J'J'^*} T_{\tau\tau}^{JJ'} T_{\tau\tau}^{J'J'^*} \{J\tau J' - \tau | LM\} \{J\lambda J' - \lambda' | Lm\} \quad (\text{E.26})$$

Our first result follows from inspection of the first C-G coefficient in equation (E.26).

$$H^{\ell m LM} = 0 \quad \text{if } M \neq 0 \quad (\text{E.27})$$

This relation is a corollary of the azimuthal symmetry attendant on helicity conservation. Using equations (E.23) and (E.24) we rewrite equation (E.19) as follows.

$$H_{\nu}^{\ell m L M} = N_{\Delta}^2 |F_{\nu}^{\Delta}|^2 \left( \frac{4\pi}{2\ell+1} \right) (-1)^{1/2+\nu} \left\{ \frac{3}{2} \nu \frac{3}{2} -\nu \mid \ell 0 \right\} \left( \frac{4\pi}{2L+1} \right) h^{\ell m L M} \quad (\text{E.28})$$

$$h^{\ell m L M} = \sum_{\lambda \lambda'} \left\{ \frac{3}{2} \lambda \frac{3}{2} -\lambda' \mid \ell \right\} k_{\lambda \lambda'}^{m L M} \quad (\text{E.29})$$

Then summing equation (E.28) over the helicities of the final nucleon,  $\nu$ , we obtain

$$H^{\ell m L M} = N_{\Delta}^2 \left( \frac{4\pi}{2\ell+1} \right) \left( \frac{4\pi}{2L+1} \right) f_{\ell}^{\Delta} h^{\ell m L M} \quad (\text{E.30})$$

$$f_{\ell}^{\Delta} = \sum_{\nu} |F_{\nu}^{\Delta}|^2 (-1)^{1/2+\nu} \left\{ \frac{3}{2} \nu \frac{3}{2} -\nu \mid \ell 0 \right\} . \quad (\text{E.31})$$

Using parity conservation in the  $\Delta$  decay, equation (E.12), permits us to do the sum in equation (E.31).

$$f_{\ell}^{\Delta} = \begin{cases} (-1)^{\ell/2} |F_{1/2}^{\Delta}|^2 & \ell = 0, 2 \\ 0 & \ell = 1, 3 \end{cases} \quad (\text{E.32})$$

We can now outline the rest of this derivation. We invert equations (E.29) and (E.30) which enables us to write each  $k$  as a sum

of H's. Then we can readily express in terms of H's a number of relations of the k's which follow directly from properties of the constituent amplitudes and C-G coefficients.

To invert equations (E.29) we use the following expression of orthonormality of the C-G coefficients [Edmonds 1957, equation (3.5.5)].

$$\sum_{j_3} \{j_1 m_1 j_2 m_2 - m_1 | j_3 m_3\} \{j_1 m_1' j_2 m_2 - m_1' | j_3 m_3\} = \delta_{m_1, m_1'} \quad (\text{E.33})$$

We obtain

$$k_{\lambda\lambda'}^{mLM} = \sum_{\ell} \left\{ \frac{3}{2} \lambda \frac{3}{2} - \lambda' | \ell m \right\} h^{\ell m LM}, \quad m = \lambda - \lambda' \quad (\text{E.34})$$

Because  $f_{\ell}^{\Delta} = 0$  when  $\ell$  is odd, we can better use a modification of equation (E.34) in which the sum extends only over even  $\ell$ .

$$\begin{aligned} k_{-\lambda' - \lambda}^{mLM} &= \sum_{\ell} \left\{ \frac{3}{2} - \lambda' \frac{3}{2} \lambda | \ell m \right\} h^{\ell m LM} \\ &= - \sum_{\ell} (-1)^{\ell} \left\{ \frac{3}{2} \lambda \frac{3}{2} - \lambda' | \ell m \right\} h^{\ell m LM} \end{aligned} \quad (\text{E.35})$$

An easy demonstration using equations (E.15), (E.16), (E.25), (E.26), and symmetries of the C-G coefficients shows that

$$k_{-\lambda' - \lambda}^{mLM} = - k_{\lambda\lambda'}^{mLM} \quad (\text{E.36})$$

We note that the demonstration of equation (E.36) is our first use of the Gribov-Morrison rule. Combining equations (E.34), (E.35), and (E.36) we write

$$\operatorname{Re} \left( k_{\lambda\lambda'}^{mLM} \right) = \sum_{\text{even } \ell} \left\{ \frac{3}{2} \lambda \frac{3}{2} - \lambda' \mid \ell m \right\} h^{\ell m LM}. \quad (\text{E.37})$$

For convenience we define

$$\begin{aligned} G_{\lambda\lambda'}^{LM} &= \frac{(-1)^{3/2-\lambda'}}{4\pi N_{\Delta}^2} \sum_{\text{even } \ell} (f_{\ell}^{\Delta})^{-1} (2\ell+1) \left\{ \frac{3}{2} \lambda - \lambda' \mid \ell m \right\} H^{\ell m LM} \\ &= \frac{(-1)^{3/2-\lambda'}}{4\pi N_{\Delta}^2 |F_{1/2}^{\Delta}|^2} \sum_{\text{even } \ell} (-1)^{\ell/2} (2\ell+1) \left\{ \frac{3}{2} \lambda \frac{3}{2} - \lambda' \mid \ell m \right\} H^{\ell m LM} \end{aligned} \quad (\text{E.38})$$

which, like  $H$ , is calculable from data. (Our  $G_{\lambda\lambda'}^{LM}$  is identical to Chung's  $G_{\lambda\lambda'}^{(+)}(LM)$ , equation (7.30).) From equations (E.30), (E.37), and (E.38)

$$\frac{2L+1}{4\pi} G_{\lambda\lambda'}^{LM} = (-1)^{3/2-\lambda'} \operatorname{Re} \left( k_{\lambda\lambda'}^{mLM} \right). \quad (\text{E.39})$$

The reality of the moments  $H$  and  $G$  actually follows just from parity invariance in the process (E.1). Under reflection in the production plane  $\phi_{\Delta} \rightarrow -\phi_{\Delta}$ ,  $\phi_p \rightarrow -\phi_p$ , and consequently

$H^{\ell m L M} \rightarrow (H^{\ell m L M})^*$ . With an unpolarized beam the intensity is invariant under the reflection so that integration over the azimuth angles results in real quantities.

We now develop four more properties of the  $k$ 's which appear below as equations (E.49)-(E.52). We begin with a few definitions.

$J \equiv$  the highest spin produced.

$$T^J = 0 \quad \text{if } J > J \quad (\text{E.40})$$

$$\theta_+(n) \equiv \begin{cases} 1 & \text{if } n \text{ even} \\ 0 & \text{if } n \text{ odd} \end{cases} \quad (\text{E.41a})$$

$$\theta_-(n) \equiv \begin{cases} 1 & \text{if } n \text{ odd} \\ 0 & \text{if } n \text{ even} \end{cases} \quad (\text{E.41b})$$

$$W_{ijk} \equiv \frac{1}{2} \sum_{L=0}^{2J} \sum_{J,J'}^J \sum_{\tau} \theta_i(L) \theta_j(J+J') \theta_k(1/2-\tau) w_{3/2}^{LJJ'} \quad (\text{E.42})$$

The subscripts of  $W$  take the symbolic values  $+$  and  $-$ . These  $W$ 's are a useful way to break up certain sums of  $k$ 's. Specifically,

$$\sum_{L=0}^{2J} \theta_+(L) k_{3/2}^{OLO} = W_{+++} + W_{++-} + W_{+-+} + W_{+--} \quad (\text{E.43})$$

$$\sum_{L=0}^{2J} \theta_-(L) k_{3/2}^{OLO} = W_{-++} + W_{-+-} + W_{--+} + W_{---} . \quad (E.44)$$

Orthogonality of the C-G coefficients, equation (E.32), applied to  $w$  yields

$$\sum_{L=0}^{2J} w_{3/2}^{LJJ'} = 0 \quad (E.45)$$

from which immediately follows

$$W_{+ij} + W_{-ij} = 0 . \quad (E.46)$$

We sum  $w$  over  $\tau$  using equation (E.15) to obtain

$$\sum_{\tau} w_{\lambda\lambda'}^{LJJ'} = -2\theta_-(J+J'-L) N_J N_{J'} F_{\lambda}^J F_{\lambda'}^{J'*} T_{1/2}^J T_{1/2}^{J'*} \left\{ \begin{matrix} J & J' & -1 \\ 2 & 2 & 2 \end{matrix} \middle| L0 \right\} \{ J\lambda J' - \lambda' | Lm \} \quad (E.47)$$

which quickly leads to

$$W_{ij+} + W_{ij-} = 0 \text{ if } i = j . \quad (E.48)$$

If to the r.h.s. of equation (E.43) we add  $\frac{1}{2}(W_{-++} + W_{-+-} + W_{--+} - W_{+--})$  which is zero by equation (E.48) and subtract  $\frac{1}{2}(W_{+++} + W_{-++} + W_{++-} + W_{-+-})$  which is zero by equation (E.46), we find

$$\sum_{L=0}^{2J} \theta_+(L) k_{3/2}^{OLO} = 0 . \quad (E.49)$$

Analogously

$$\sum_{L=0}^{2J} \theta_{-}(L) k_{3/2 \ 3/2}^{0L0} = 0 . \quad (\text{E.50})$$

That  $k$  is zero when  $L > 2J$  is apparent from inspection of the C-G coefficients in equation (E.26). Equation (E.47) shows that the sum on  $\tau$  makes  $k$  zero also when  $L = 2J$  so that

$$k_{\lambda\lambda'}^{mLM} = 0 \quad \text{if } L \geq 2J . \quad (\text{E.51})$$

On this account the sum in equation (E.50) need extend only to  $2J-2$ . Equation (E.47) also implies that the only  $J, J'$  pair which contributes to  $k$  for  $L = 2J-1$  is  $J = J' = J$ . This simplification permits us to derive one more relation.

$$\begin{aligned} k_{3/2-1/2}^{2L0} &= - N_{J \ 3/2}^{2FJ} F_{-1/2}^{J*} |T_{1/2}^J|^2 \{J \ 1/2 \ J-1/2 | L0\} \{J \ 3/2 \ J \ 1/2 | L2\} \\ &= \frac{\{J \ 3/2 \ J \ 1/2 | L2\}}{\{J \ 3/2 \ J-1/2 | L1\}} N_{J \ 3/2}^{2FJ} F_{1/2}^{J*} |T_{1/2}^J|^2 \{J \ 1/2 \ J-1/2 | L0\} \{J \ 3/2 \ J-1/2 | L1\} \\ &= \frac{1}{2} \left[ \frac{2J+1}{2J-2} \right]^{1/2} k_{3/2 \ 1/2}^{1L0}, \quad L = 2J - 1 \end{aligned} \quad (\text{E.52})$$

Once again we used equation (E.16). The ratio of C-G coefficients is one of several which Chung gives in his Appendix A.

We recapitulate using this time the experimentally accessible moments  $G$  instead of  $k$ .

$$G_{\lambda\lambda'}^{LM} = 0 \quad \text{if } M \neq 0 \quad (\text{E.53})$$

$$G_{\lambda\lambda'}^{LM} = 0 \quad \text{if } L \geq 2J \quad (\text{E.54})$$

$$\sum_{L=0}^{2J-1} \theta_+(L) (2L+1) G_{3/2 \ 3/2}^{L0} = 0 \quad (\text{E.55})$$

$$\sum_{L=1}^{2J-2} \theta_-(L) (2L+1) G_{3/2 \ 3/2}^{L0} = 0 \quad (\text{E.56})$$

$$G_{3/2 \ 1/2}^{L0} + 2 \left[ \frac{2J-2}{2J+1} \right]^{1/2} G_{3/2-1/2}^{L0} = 0 \quad \text{if } L = 2J-1 \quad (\text{E.57})$$

## List of References

- Abarbanel, H. D. I. 1976. *Rev. Mod. Phys.* 48, 435.
- Albrecht, H. C., et al. 1968. The COBWEB data reduction system. Lawrence Berkeley Laboratory report UCRL-18528 Rev.
- Anderson, E. W., et al. 1966. *Phys. Rev. Lett.* 16, 855.
- Antipov, Yu. M., et al. 1973. *Nucl. Phys. B* 63, 153.
- Antipov, Yu. M., et al. 1975. *Nucl. Phys. B* 99, 189.
- Apokin, V. D., et al. 1976. Elastic  $\pi^-$  meson and proton scattering on nuclei in the diffraction cone region within momentum range 30-50 GeV/c. Inst. of High Energy Physics, Serpukhov, preprint 76-122.
- Ballam, J., et al. 1970. *Phys. Rev. Lett.* 24, 960.
- Beaupré, J. V., et al. 1971a. *Phys. Lett. B* 34, 160.
- Beaupré, J., et al. 1971b. *Nucl. Phys. B* 35, 61.
- Beaupré, J. V., et al. 1972a. *Nucl. Phys. B* 47, 51.
- Beaupré, J. V., et al. 1972b. *Nucl. Phys. B* 49, 441.
- Beaupré, J. V., et al. 1973. *Nucl. Phys. B* 66, 93.
- Beketov, G. V., et al. 1974. *Yad. Fiz.* 19, 830 [*Sov. J. Nucl. Phys.* 19, 424].
- Belletini, G., et al. 1965. *Phys. Lett.* 18, 167.
- Berger, E. L. 1968. *Phys. Rev. Lett.* 21, 701.
- Biazas, A., J. Dabkowski, and L. Van Hove 1971. *Nucl. Phys. B* 27, 338.
- Biel, J., et al. 1976. *Phys. Rev. Lett.* 36, 504.
- Blieden, H. R., et al. 1975. *Phys. Rev. D* 11, 14.
- Blobel, V., et al. 1975. *Nucl. Phys. B* 97, 201.
- Boesebeck, K., et al. 1971. *Nucl. Phys. B* 33, 445.
- Boesebeck, K., et al. 1972. *Nucl. Phys. B* 40, 39.
- Boyarski, A. M., et al. 1968. "Yields of secondary particles from 18 GeV electrons," in *SLAC Users Handbook*, sec. C2.

- Brody, A. D., et al. 1971. Phys. Rev. Lett. 26, 1050.
- Carlitz, R., S. Frautschi, and G. Zweig 1969. Phys. Rev. Lett. 23, 1134.
- Chapman, J. W., et al. 1973. Phys. Rev. Lett. 30, 64.
- Cheng, H., and T. T. Wu 1971. Phys. Lett. B 36, 357.
- Chou, T. T., and C. N. Yang 1968. Phys. Rev. 175, 1832.
- Chung, S. U. 1971. Spin formalisms. CERN report 71-8.
- Cohen-Tannoudji, G., et al. 1970. Phys. Lett. B 33, 183.
- Colley, D. C., et al. 1973. Nucl. Phys. B 55, 1.
- Colton, E., and P. Schlein 1969. "Experimental validity of one-pion exchange and prospects for studying  $\pi\pi$  and  $K\pi$  scattering," in Proceedings of the Conference on  $\pi\pi$  and  $K\pi$  Interactions (Argonne National Laboratory), p. 1. Edited by F. Loeffler and E. Malamud.
- Colton, E., et al. 1971. Phys. Rev. D 3, 1063.
- Dahl, O. I., et al. 1968. SQUAW kinematic fitting program. Group A, Lawrence Berkeley Laboratory, Programming Note P-126.
- Deck, R. T. 1964. Phys. Rev. Lett. 13, 169.
- Derrick, M. 1975. "Diffractive processes," in Particles and Fields -- 1975 (APS/DPF Seattle), p. 33. Edited by H. J. Lubatti and P. M. Mockett.
- Donohue, J. T. 1971. Nucl. Phys. B 35, 213.
- Drell, S. D., and K. Hiida 1961. Phys. Rev. Lett. 7, 199.
- Edelstein, R. M., et al. 1977. Phys. Rev. Lett. 38, 185.
- Edmonds, A. R. 1957. Angular Momentum in Quantum Mechanics. Princeton: Princeton University Press.
- Evans, D., et al. 1973. Nuovo Cimento A 14, 651.
- Foley, K. J., et al. 1967. Phys. Rev. Lett. 19, 397.
- Foley, K. J., et al. 1969. Phys. Rev. 181, 1775.
- Fox, G. C. and C. Quigg 1973. Annu. Rev. Nucl. Sci. 23, 219.

- Friedman, J. H. 1974. Data analysis techniques for high energy particle physics. SLAC Report No. 176.
- Gilman, F. J., et al. 1970. Phys. Lett. B 31, 387.
- Good, M. L. and W. D. Walker 1960. Phys. Rev. 120, 1857.
- Gottfried, K., and J. D. Jackson 1964. Nuovo Cimento 33, 309.
- Gramenitskii, I. M., and Z. Novak 1974. Fiz. El. Chastits At. Yad. 5, 63 [Sov. J. Part. Nucl. 5, 25].
- Gribov, V. N. 1967. Yad. Fiz. 5, 197 [Sov. J. Nucl. Phys. 5, 138].
- Herndon, D. J., et al. 1975. Phys. Rev. D 11, 3183.
- Hohler, G., and R. Strauss 1970. Z. Phys. 232, 205.
- Jackson, J. D. 1965. "Particle and polarization angular distributions for two and three body decays," in High Energy Physics (Les Houches Lectures), p. 325. Edited by C. DeWitt and M. Jacob. New York: Gordon and Breach.
- Johnstad, H., et al. 1972. Nucl. Phys. B 42, 558.
- Kane, G. L., and A. Seidl 1976. Rev. Mod. Phys. 48, 309.
- Kuiper, N. H. 1960. Nederl. Akad. Wetensch. Proc. Ser. A 63, 38.
- Lamsa, J. W., et al. 1972. Nucl. Phys. B 37, 364.
- Leith, D. W. G. S. 1974. "Diffractive processes," in Proceedings of Summer Institute on Particle Physics, SLAC Report No. 179, vol. 1, p. 1. Edited by M. C. Zipf.
- Longacre, R. S., et al. 1975. Phys. Lett. B 55, 415.
- Miettinen, H. I. 1975. "Diffractive processes and the triple-Pomeron," in High Energy Physics: Proceedings of the EPS International Conference (Palermo) vol. 2, p. 731. Edited by A. Zichichi. Bologna: Editrice T. Compositori.
- Morrison, D. R. O. 1968. Phys. Rev. 165, 1699.
- Morse, R., et al. 1971. Phys. Rev. D 4, 133.
- O'Brien, D. D., et al. 1974. Nucl. Phys. B 77, 1.
- Oh, B. Y., and W. D. Walker 1969. Phys. Lett. B 8, 564.

- Particle Data Group 1976. Review of Particle Properties. Rev. Mod. Phys. 48, No. 2, Part II.
- Resnick, L. 1966. Phys. Rev. 150, 1292.
- Rhode, J. I., et al. 1969. Phys. Rev. 187, 1844.
- Rushbrooke, J. G., et al. 1971a. Phys. Rev. D 4, 3273.
- Rushbrooke, J. G., et al. 1971b. Nucl. Phys. B 35, 1.
- Saclay 1974. The Particle Data Group, Lawrence Berkeley Laboratory, furnished us with the unpublished results of the Saclay elastic phase shift analysis.
- Satz, H., and K. Schilling 1971. Nuovo Cimento Lett. 1, 351.
- Solmitz, F. T., A. D. Johnson, and T. B. Day 1966. Three view geometry program. Alvarez Group, Lawrence Berkeley Laboratory, Programming Note P-117.
- Treiman, S. B., and C. N. Yang 1962. Phys. Rev. Lett. 8, 140.
- Webb, R., et al. 1975. Phys. Lett. B 55, 331.
- White, H. S., et al. 1968. DAPR: Digital pattern recognition approaches production. Lawrence Berkeley Laboratory preprint UCRL-18543.
- Willmann, R. B., et al. 1970. Phys. Rev. Lett. 24, 1260.